TUM School of Computation, Information and Technology
Technische Universität München

Ion-beam irradiation presented as a universal fabrication method for spin-wave devices in YIG

Martina Kiechle, M.Sc.

Vollständiger Abdruck der von der TUM School of Computation, Information and Technology der Technischen Universität München zur Erlangung des akademischen Grades einer

Doktorin der Ingenieurwissenschaften (Dr.-Ing.)

genehmigten Dissertation.

Vorsitz
Prof. Dr.-Ing. Amelie Hagelauer

Prüfer der Dissertation:
1. Priv.-Doz. Dr.-Ing. habil. Markus Becherer
2. Prof. Dr. Will Branford

Die Dissertation wurde am 28.06.2023 bei der Technischen Universität München eingereicht und durch die TUM School of Computation, Information and Technology am 04.08.2023 angenommen.

To my own diligence and laziness, the greatest partners in crime.

You can learn anything if you really want to.
Once you found your inner drive, the sky is the limit.
The sky is not the limit, and neither is the universe.

And if you do not want to do anything, that is also fine.

Abstract

Using spin waves as information carriers in computing tasks is a promising alternative to perform efficient signal processing. Apart from propagating at low power levels at wavelengths that are orders of magnitude smaller than that of electromagnetic waves at microwave frequencies, spin waves are particularly useful in the emerging field of neuromorphic computing because they offer easily accessible non-linear interactions. Device scaling becomes not only possible but also inevitable due to the limited propagation range. Hereby, the fabrication of nanostructures with excellent quality is one of the main challenges with spin-wave devices, and this should ideally be compatible with standard industrial processes to accelerate device integration. For that purpose, a fabrication workflow for spin-wave computing elements in the most commonly used magnonic material as a thin film - Yttrium Iron Garnet - has been developed. The magnetic properties of YIG can be altered with nanoscale precision using direct focused-ion-beam irradiation, a technique that has been widely used in metallic magnetic systems to locally change their magnetic properties. In YIG, this has previously been reported as an undesired side effect of ion milling due to the creation of defects. Ion milling or wet chemical etching have been most used to fabricate devices in YIG, but they imply the physical structuring of YIG. Here, focused ion irradiation is explicitly used to change the magnetic properties, precisely the effective magnetization, through ion implantation instead of removing material, and it is shown how the initial drawback of unwanted modification can be turned into an advantage for device manufacturing. This allows one to engineer the magnonic index of refraction adapted to desired applications. This technique allows rapid fabrication of high-quality architectures of modified magnetization in magnonic media with minimal defects, whereby magnetic damping is not severely increased. Magnetic landscapes are ion-beam-written into YIG with dwell times in the low nanosecond range using 50 keV accelerated Ga^+ ions. Furthermore, an efficient method to fabricate magnetization gradients is demonstrated, enabling smooth transitions of the magnetic properties that are required in many sophisticated devices. This work presents remarkable progress on spin-wave device fabrication, demonstrated by spin-wave computing elements of high complexity inspired by optical computing, more specifically Fourier optics, but also points out the universality of this technique by fabricating and characterizing machine-learned magnetization patterns of unintuitive shape.

Preface

This thesis is an original work by myself, Martina Kiechle. In Chapter 2, the experimental platform for spin-wave devices developed during my doctoral program is thoroughly explained to equip the reader with the foundations of the presented results. Some content has been published as supplementary material in **M. Kiechle, A. Papp, S. Mendisch, *et al.*, "Spin-wave optics in yig realized by ion-beam irradiation", *Small*, p. 2 207 293, 2023. DOI: 10.1002/smll.202207293**.

Chapter 3 was originally published as **M. Kiechle, A. Papp, S. Mendisch, *et al.*, "Spin-wave optics in yig realized by ion-beam irradiation", *Small*, p. 2 207 293, 2023. DOI: 10.1002/smll.202207293**. I performed most of the experiments, including the creation/coding of the designs, performed almost all measurements and data analysis, and wrote the major part of the manuscript. Ádám Papp provided many design ideas, reviewed and improved my code, performed simulations and built the trMOKE microscope I used for the measurements. Simon Mendisch tremendously helped in developing the optimal sputter deposition process for YIG, and together with Valentin Ahrens contributed to the development of an efficient workflow for the FIB irradiation process. Matthias Golibrzuch optimized the delicate metallization process, sputtered some of the YIG samples and advised in fabrication aspects. Gary H. Bernstein and Wolfgang Porod organized and planned the TEM measurements and helped to analyze the results. György Csaba gave guidance in research direction and interpretation, and wrote/revised a significant part of the manuscript. Markus Becherer provided experimental direction and advised in every single process step.

Chapter 4 was originally published as **Á. Papp, M. Kiechle, S. Mendisch, *et al.*, "Experimental demonstration of a concave grating for spin waves in the rowland arrangement", *Scientific Reports*, vol. 11, no. 1, pp. 1–8, 2021. DOI: 10.1038/s41598-021-93700-z**. This manuscript has a shared first-authorship (equal contribution) between Ádám Papp and myself.
Ádám Papp created the experimental design and built the trMOKE used for the optical measurement, I fabricated the samples, performed the FIB experiment and the measurement, and optimized the trMOKE construction. We worked together on data post-processing and interpretation, prepared the figures, and wrote the main part of the manuscript. Simon Mendisch and Valentin Ahrens helped with the YIG sample fabrication and the metallization process and assisted in the FIB irradiation procedure. Levent Sahin and Lukas Seitner helped with the YIG characterization (ferromagnetic resonance, transmission measurements), György Csaba wrote a significant part of the manuscript, did background research on the discovered effect and helped together with Wolfgang Porod to interpret and analyze the discovered effect. Markus Becherer gave experimental guidance and helped to set up the experiments.

Chapter 5 was originally published as **M. Kiechle, L. Maucha, V. Ahrens, *et al.*, "Experimental demonstration of a spin-wave lens designed with machine learning", *IEEE Magnetics Letters*, vol. 13, pp. 1–5, 2022. DOI: 10.1109/LMAG.2022.3209647**. I did the pre-characterization of the sample needed for the training parameters, planned the experiment, led all experimental steps, performed the optical measurements and data processing, and wrote the major part of the manuscript. Levente Maucha performed the training of magnetization parameters in SpinTorch, Simon Mendisch and Valentin Ahrens helped with the FIB irradiation, Matthias Golibrzuch fabricated metallic leads and helped with the measurements, Carsten Dubs provided the LPE fabricated YIG thin film, Wolfgang Porod gave guidance in developing SpinTorch and planning the experiment, György Csaba gave inspirations for the experiments and helped writing and to improve the manuscript. Markus Becherer

gave guidance for all experimental steps and helped to improve the measurements, Ádám Papp had the original idea, developed SpinTorch and provided directions for the measurements.

Contents

1 Introduction

In this chapter, the motivation and the objective of the work at hand are presented. Also, an overview of related work is given. Following this, the introductory section on spin waves (SWs) and their application in alternative computing devices provides the necessary theoretical background and contextualizes the focus of this work. In Chapter 2, the experimental methodologies for fabricating and characterizing spin-wave devices are explained. Chapters 3, 4, and 5 show the centerpieces of this thesis, the main achievements in form of published results. The discussion of the results and the outlook on future work in Chap. 6 concludes this work.

1.1 Motivation

The properties of spin waves and the working mechanisms in spin-wave-based computing devices are actively researched primarily within the physics community [4]–[7], as they provide an attractive alternative to existing computing architectures, primarily scoring points with low-power transmission and extensive device scalability due to orders of magnitude shorter wavelengths at microwave frequencies.

Sadly, very little attention is given to the engineering aspects such as clean and efficient device manufacturing and integration problems with electronic circuitry. A few impressive spin-wave device concepts have been experimentally demonstrated in the direction of digital as well as non-Boolean computing, e. g. a magnonic transistor [8] and a majority gate [9], but also a spin-wave-based interference device [10]. However, hardly any literature shows up their cards when it comes to reproducibility and performance robustness.

The applied manufacturing techniques are nowhere close to producing high-performance architectures reliably with realistic time effort, a prerequisite for mass production. Reactive ion-milling of Yttrium Iron Garnet (YIG) is highly time-consuming and involves unavoidable ion scattering during the bombardment that could inadvertently alter the magnetic properties in the structures' peripheral zones [11], [12]. Similarly, chemical etching using phosphoric acid can be tricky due to YIG's crystallinity and needs to be done at high temperatures, and added to this it is limited to larger structural sizes and acts highly isotropic, causing surface and edge inhomogeneities [13], [14]. The production of high-quality (periodic) nanostructures with perfect edges and interfaces needed in nano-conduits that are compatible with lithographic process standards to enable mass fabrication remains one of the main problems in device fabrication [4].

On top of many unsolved problems within the functional medium, there is no working solution for the integration into existing CMOS environments, not to mention a surrounding platform for standalone spin-wave devices. On this road, fundamental questions need quantitative clarification, e. g. how a spin-wave conduit compares in energy efficiency, speed, and size to a microwave or photonic waveguide, what can be gained if the electronic waveguides and transistors of a high-frequency chip are replaced by spin-wave conduits, can spin waves be excited and measured with relatively inexpensive electronic antennas with small insertion loss, what are the manufacturing and sensitivity problems with alternative detection schemes, for instance, elements using the inverse spin Hall effect or magnetic-tunnel-junction-based spin-torque oscillators. For now, most experiments are carried out using expensive electronic and optical equipment such as HF signal generators, network analyzers, and time- and / or frequency-resolved optical probing, such as time-resolved Kerr microscopy (trMOKE) or Brillouin light scattering (BLS).

To get this straight from the beginning, the work shown in this thesis does not solve any of the above-mentioned problems regarding integration. It is rather starting from the point of developing a practical technology platform to manufacture spin-wave device architectures of demanded complexity and minimal defects, offering a rapid prototyping platform to the community for ground-breaking device ideas to come. The center technology is direct focused-ion-beam (FIB) irradiation of YIG thin films, which was found to change the magnetic properties with nanoscale precision. YIG is the most commonly used material to carry spin waves because of its record low magnetic damping, allowing waves to propagate over distances many tenfold of their wavelength (mainly determined by their group velocity) without additional amplification. FIB has been used extensively to alter the magnetic properties of magnetic metals [15], and we are only aware of one previous attempt to apply FIB in a nonablative fashion to YIG [16], however, with a not meaningful amount of data points and no investigation on the impact on spin waves. Thus, we are the first group to explore the occurring effects on spin waves to the extent demonstrated, holding out the prospect of adaptability in device design and manufacturing. To showcase the performance outcome, a number of spin-wave computing elements are experimentally demonstrated, primarily inspired by optics, but also unconventional architectures of arbitrary shape, highlighting the versatility of the technique.

1.2 Related work

The 'Nanomagnetic devices' group of Markus Becherer has an extensive background in the field of perpendicular Nanomagnetic logic (pNML) – a concept that uses the dipole field coupling of neighboring nanomagnets with perpendicular magnetic anisotropy (PMA) to switch their magnetization to either 'spin-up' or 'spin-down' by a driving field in a controlled and nonvolatile fashion [17]. The experimental project started out with Markus Becherer's doctoral project by fabricating and characterizing Co/Pt multilayer nanomagnets, and later engineering their switching fields by introducing artificial nucleation centers (ANCs) via FIB irradiation. Soon after, NML-based circuits have been realized by former doctoral candidates, e. g. a majority gate, followed by a 1-bit full-adder and even exploring 3D circuitry. The NML building blocks and the material systems have been further engineered, enabling driving field pulses in the nanosecond range, domain-wall logic, and low-power logic operations [18], [19]. Furthermore, material systems exhibiting DMI have been investigated to use magnetic skyrmions as information carriers [20]–[22]. Throughout this time, our group collaborated with György Csaba (Markus' Ph.D. supervisor) and Wolfgang Porod at the University of Notre Dame, and they started exploring the field of Magnonics within the Ph.D. program of Ádám Papp after he performed the simulations of the NML devices experimentally shown in Munich. Following this constellation of group work, we proposed a DFG project for my Ph.D. position and a post-doc project for Ádám on combining the principles of NML with YIG – the 'hybrid spin-wave platform', introduced in the following section.

1.3 Objective

The objective of this research project was to develop an experimental spin-wave platform to flexibly alter the magnetic properties of YIG locally, thereby steering wave propagation, to realize computing functions in the magnonic domain. Key aspects are the fabrication of magnetic media to carry and manipulate spin waves, to investigate coupling mechanisms and control their interaction, and eventually to implement SW computing elements in order to showcase the platform's performance and potential. Efficient and robust fabrication methods play a central role in pushing the technology readiness of spin-wave devices, a milestone that has been poorly addressed so far.

Although the platform was initially planned to consist of Co/Pt hard magnets on top of YIG, similar functions could be realized by using direct focused-ion-beam irradiation instead, besides offering much better visualization in optical metrology. Fig. 1.1 shows the proposed concept in the

DFG grant No. 429656450. Here, the Co/Pt magnets featuring perpendicular magnetic anisotropy (PMA) are fabricated on top of YIG to influence the spin-wave dispersion relation locally with their emitted dipole fields. With this, optically inspired structures can be formed, e. g. a grating or a graded index profile by using the stay-field profiles. One way of looking at a periodic array of Co/Pt magnets on top of YIG is magnonic crystal[23], the magnetic counterpart of a photonic crystal, i. e. a periodically recurring alternation of the magnetic properties. There has been extensive research on this topic[24] in the last two decades, and the presented arrangement using PMA is one new way of realizing a reconfigurable [25] version of this. However, the magnonic crystal just served as a showcase example to express the potential of the platform – the actual vision was to realize numerous computing functions via magnetization profiles on YIG of arbitrary shape.

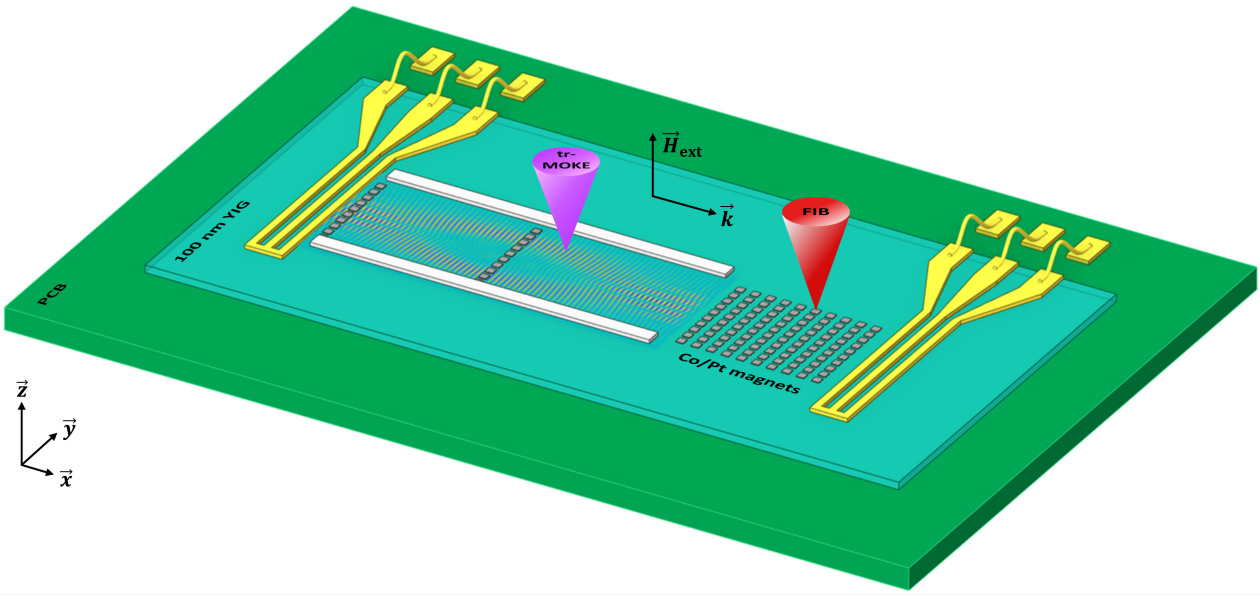

Figure 1.1 Schematic illustration of the hybrid spin-wave platform initially proposed in the DFG grant No. xxx. A 100 nm thin YIG film on a GGG substrate with coplanar microwave antennas on top is bonded to PCB carrier to electrically excite and detect spin waves. The spin waves traveling in YIG are influenced by the emitted dipole fields of Co/Pt nanomagnets, and the wave patterns can be visualized with time-resolved Kerr microscopy. As an additional engineering step, the switching field of the Co/Pt magnets can be lowered selectively, allowing the generation of alternating magnetization patterns reconfigurably with a global field.

As an advanced step, FIB irradiation can be used to selectively lower the switching field of individual magnets in an array, allowing the creation of arrangements with different magnetization orientations by using a global field. As long as the switching fields are higher than the bias field needed for YIG, the Co/Pt magnets maintain their magnetization direction and can be switched reconfigurably, offering a degree of freedom in pattern generation.

On the road to fabricating the magnetic layers of the platform, a side project of FIB-irradiating YIG directly to change the magnetic properties turned into the main objective of this thesis as we obtained such promising results that I wanted to spend all my time pursuing this course. Here's a brief piece of history of how we got to change gears: During an informal workshop on Mumax3 with Ádám Papp in early 2019, Simon Mendisch and I talked about fabrication complications when irradiating the Co/Pt magnets on YIG, and Ádám wondered if we could irradiate YIG directly also. Simon, the FIB expert in our group at the time, brought up the potential issue of excess surface charge when irradiating insulators, but the high acceleration voltage of 50 kV might "bang in" the ions either way. We debated about potential effects and concluded that it is probably too much hassle for nothing, we forgot about the idea and went on with our workshop. That evening I did some research following

our discussion and could only find one paper where the irradiation of YIG had been tried out [16], although with very few data points and vague statements, but in principle proof that it could work. Since we had a good ferromagnetic resonance (FMR) setup as a characterization tool that I built during my master's thesis, I wanted to give this experiment a try. Simon helped to set up the irradiation, and we did a quick proof of principle, unveiling that the resonance field indeed changes. Soon after, I put a student, Carolin Calcagno, on this project, and she did a series of irradiations on YIG, also with different film thicknesses, and helped us to characterize the effect in more detail. From here, Ádám saw the potential of this technique and pushed to fabricate optical structures on YIG that we could measure with his newly developed trMOKE microscope.

Quantitatively, changing the external field (by Co/Pt magnets) or the saturation magnetization (via FIB irradiation) express nearly the same effect in the spin-wave dispersion relation, they induce a quasi-linear shift of the curve in frequency space (discussed in Sec.1.4.1), where both directions can be accomplished with both methods (ion-dose-dependent for FIB, magnetization orientation dependent for Co/Pt magnets). One main difference is the range of achievable change, which is more limited by FIB (the anisotropy change saturates), whereas in the case of Co/Pt magnets, the magnitude of dipole fields depends on the magnetic moment, which can be engineered by the number of Cobalt multilayers (this is ultimately compromised by a single domain state and maintaining the PMA). Now, the hybrid platform, aka the Co/Pt nanomagnets on top of YIG, is definitely the winner when it comes to reconfigurability, but on the downside, the stacks' seedlayer is Platinum, one of the most commonly used spin sink materials for YIG [26], [27] to explore spin pumping. This can potentially be solved by avoiding direct surface contact, e. g. using a SiO_2 spacer layer between the Co/Pt stack and YIG. However, a major drawback in the experimental visualization is the opacity of the stacks towards the 405 nm laser used in the time-resolved MOKE, hence not allowing to study the resulting spin-wave pattern in YIG underneath. The beauty of using direct FIB irradiation is not only the much higher spatial resolution offered (> 10 nm), but also practicability (the fewest process steps, no additional materials are needed) and applicability (ion-implanters are industry-standard). For research proposes, the direct imaging of spin-waves in (un-)irradiated YIG allows the most precise characterization of the effect needed for device designs.

1.4 Spin-wave propagation characteristics

In this section, the relevant aspects of spin-wave theory in magnetic thin films are presented to the reader. To begin with, a macro-spin model is assumed, i. e. an effective magnetic field H_{eff} is stronger than the films saturation magnetization M_{s} and anisotropy field H_{a} in this specific direction, summarized in the effective magnetization $M_{\mathrm{eff}} = M_{\mathrm{s}} - H_{\mathrm{a}}$, leading to the precession of spins about this equilibrium direction. This precession can propagate, and a spin wave is then defined by the relative phase shift between adjacent magnetic moments. The wave number k of a spin wave is expressed by the physical length after which the phase has rotated by 360 °, and it is connected to the precession frequency in the spin-wave dispersion relation $\omega(k)$ [28], [29]. The orchestrated precession can be excited by an oscillating magnetic field of high frequency f (gigahertz) perpendicular to the orientation of the magnetic moments [30]. The fundamental state of precession is uniform, i. e. all spins precess in phase and with a resulting wave number $k = 0$, also known as ferromagnetic resonance (FMR) with the frequency $f_{\mathrm{FMR}}(H_{\mathrm{eff}})$. A spin wave is expressed as a higher mode of precession, excited when shifting away from $f_{\mathrm{FMR}}(H_{\mathrm{eff}})$ by either changing H_{eff} or f along the dispersion curve $f(k)$, which in turn is material-specific. The excited spin-wave type depends on dominating magnetic interactions in the magnetic medium and can be classified by the magnitude of k. Based on the exchange term $\lambda_{\mathrm{ex}} k^2$ with the exchange constant λ_{ex}, excited waves are called exchange spin waves for $\lambda_{\mathrm{ex}} k^2 >> 1$ (short-range energy), dipolar or magnetostatic spin waves when $\lambda_{\mathrm{ex}} k^2 << 1$ (long-range energy), and dipole-exchange spin waves in the transition regime.

1.4.1 Magnonic dispersion relation in thin films

Spin waves traveling in magnetic media inherently have non-linear dispersion characteristics, meaning the propagation wavelength $\lambda = 2\pi/k$ is not directly proportional to the wave frequency $\omega(k)$ as it is the case for light in vacuum ($\epsilon_r, \mu_r = 1$) with the characteristic relative permittivity ϵ_r and permeability μ_r, and waves travel with the group velocity $v_g = \omega/k = c$ that is equal to the phase velocity $v_p = c/n$, whereby $n = \sqrt{\epsilon_r \mu_r}$ is the index of refraction.

In dispersive media, waves of different frequencies (or wavelengths) travel at different phase and group velocities $v_g(\omega) = c/n_g$, and the dispersion characteristics are determined by the wavelength- or frequency-dependent index of refraction $n(\omega)$, and the corresponding group index $n_g = n(\omega) + \partial n/\partial\omega$. This dependency is called chromatic dispersion in optics, and the shape of $n(\omega)$ depends on the electromagnetic properties of the medium [31].

Similarly, magnetic parameters in spin-wave media, here considered as magnetic thin films, influence the dispersion characteristics. These are the effective magnetic field $H_{\text{eff}} = H_{\text{DC}} + H_{\text{demag}} + H_{\text{a}} + ..$ that includes a sum of different fields such as the external DC field H_{DC}, the geometry-dependent demagnetizing field H_{demag}, and the anisotropy field H_{a}, the saturation magnetization M_{s}, the film thickness d, and the exchange stiffness constant A_{ex}. A useful approximation of the dipole-exchange spin-wave dispersion relation [28] analytically derived by Kalinikos and Slavin [32] for arbitrary field orientation is given by

$$\omega(k) = \sqrt{(\omega_{\text{H}} + \omega_{\text{M}}\lambda_{\text{ex}}k^2)(\omega_{\text{H}} + \omega_{\text{M}}\lambda_{\text{ex}}k^2) + \omega_{\text{M}}F} \tag{1.1}$$

$\omega(k)$ is the spin-wave frequency of the respective wavelength k, $\omega_{\text{H}} = \gamma\mu_0 H_{\text{eff}}$ with the electron gyromagnetic ratio γ, $\omega_{\text{M}} = \gamma\mu_0 M_{\text{s}}$, and the exchange constant $\lambda_{\text{ex}} = 2A_{\text{ex}}/\mu_0 M_{\text{s}}^2 = l_{\text{ex}}^2$ [7] with the exchange length l_{ex}. The field-angle dependence is given by the factor

$$F = P + sin^2(\theta)\Big\{ 1 - P(1 + cos^2(\varphi)) + P(1-P)\frac{\mu_0 M_s}{H_{\text{eff}} + dk^2} sin^2(\varphi) \Big\} \tag{1.2}$$

and

$$P = 1 - \frac{1 - exp(-kd)}{kd} \tag{1.3}$$

whereby the angles θ and φ denote the polar and azimuthal angles of H_{eff} with respect to the wave vector k and the film surface □. The geometrical arrangement is illustrated in Fig. 1.2a. Fig. 1.2b shows exemplary dispersion curves of dipole spin waves in a YIG thin film for different field (magnetization) orientations and spin-wave propagation along the x-direction. Hereby, the material parameters $d = 100\,\text{nm}$, $M_{\text{s}} = 1.15\,\text{A/m}$, $B_{\text{DC}} = \mu_0 H_{\text{DC}} = 275\,\text{mT}$, and $A_{\text{ex}} = 3.65 \cdot 10^{12}\,\text{J/m}$ were used and the anisotropy fields were neglected. For larger wave numbers, the exchange contribution becomes non-negligible and the slope of the dispersion curves changes significantly (Fig. 1.2c). For simplicity, the wave vector is expressed in $2\pi/\mu m$, hence the resulting SW wavelength can be easily read as $1/k_x$.

The angle configurations point out the three characteristic precession modes: Forward Volume (FV), Backward Volume (BV) and Magnetostatic Surface (MS) SWs. Their characteristics are discussed in the following section using typical material parameters of the YIG thin films exploited in the experiments presented in this work.

1.4.2 Magnetostatic precession modes

Under the magnetostatic approximation, i. e. the sample dimensions are small compared to the free-space wavelength and the waves represent a solution to Maxwell's equations, three distinct types of

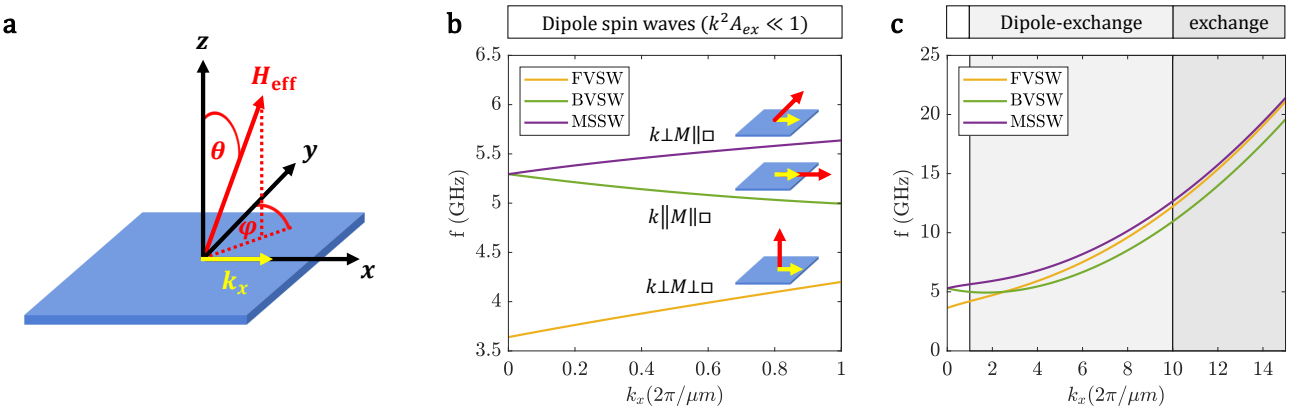

Figure 1.2 Spin-wave propagation types with respect to effective field orientation. a) Geometrical arrangement illustrating the angles (θ,φ) with respect to the H_{eff} and the spin-wave propagation direction. b) Spin-wave dispersion relations of a YIG thin film (d=100 nm, B_{DC}=275 mT, $M_s = 1.15 \cdot 10^5\, A/m$, $A_{\text{ex}} = 3.6 \cdot 10^{12}$ J/m) for three characteristic field orientations, denoting the spin-wave type in the legend. The dispersion curves show dipole spin waves only - the range relevant to the experiments presented. c) Dispersion curves in the dipole, dipole-exchange, and exchange regime, indicated by the greyscale in the background. The slope of the curve, i. e. the group velocity, increases quadratically when the exchange interaction becomes dominant when the wave number k becomes large.

spin waves, often referred to as propagation modes, can be identified depending on the effective field orientation, and hence the magnetization M, with respect to the spin-wave propagation direction k and the film surface normal $n_\square$. These correlations are expressed by the angles (θ,φ)=($\angle(H_{\text{eff}}\, n_\square)$,$\angle(H_{\text{eff}}\, k)$) in Equ. 1.2. Under the assumption that θ is the angle from the surface normal in $+z$ direction and φ the angle from k aligned along $+x$, magnetostatic surface spin waves (MSSW) are excited at (90°,0), backward volume spin waves (BVSW) at (90°,90°), and forward volume spin waves (FVSW) at (0,0).

Orthogonally magnetized films: Forward Volume waves

Magnetostatic forward volume spin waves (FVSW) are excited when $H \perp k$ and the film is magnetized out-of-plane, $H \perp \square$. The peculiarity of this precession type is its isotropy in the plane of the film, i. e. the dispersion is invariant of the direction of $k = k_{\text{x}} = k_{\text{y}}$, since spin waves always propagate perpendicular to the bias field. The group and phase velocity point in the same direction, although their values are different, hence the name forward waves. Furthermore, the amplitude is distributed in the volume in a sinusoidal fashion. The explicit analytical form of FVSW dispersion relation is given by [32], [33]

$$f_{FVSW} = \sqrt{f_{\text{H}}\left(f_{\text{H}} + f_{\text{M}}\left(1 - \frac{1 - exp(-kd)}{kd}\right)\right)} \tag{1.4}$$

with the parameters $f_{\text{H}} = \gamma\mu_0 H_{\text{eff}}$ and $f_{\text{M}} = \gamma\mu_0 M_s$. For large k values, the exchange contribution becomes non-negligible and $f_{\text{H}} = \gamma\mu_0(H_{\text{eff}} + M_s\lambda_{\text{ex}}k^2) = \gamma\mu_0(H_{\text{eff}} + 2A_{\text{ex}}/\mu_0 M_s k^2)$. Note that in this configuration the applied field is reduced by the demagnetizing field $-M_{\text{s}}$, and the cutoff frequency becomes $f_{\text{H}} = \gamma\mu_0(H_{\text{DC}} - M_{\text{s}})$.

Fig. 1.3 shows the magnetic parameter dependence for FVSW dispersion curves in YIG thin films, distinguishing the impact of the external field, the effective magnetization, and film thickness. Hereby, the top row (a-c) depicts a large k-range where the slope is dominated by $\lambda_{\text{ex}}k^2$, and the bottom row (d-f) shows a magnification of the dipole regime, the k-range relevant to this work. Changes in the

magnetic field and the magnetization appear to have equal influence with an opposite sign on the quasi-linear frequency shift in the dispersion of dipole SWs. The slope is mostly determined by the film thickness, whereby the uniform precession $k = 0$ is unaffected by a change of d.

The feature of isotropic propagation allows to draw the analogy to electromagnetic waves for FVSW and to directly adapt principles from optics to design spin wave devices. Consequently, most attention is given to this propagation type throughout this thesis. The out-of-plane direction presents a hard axis for regular YIG thin films on GGG [34], hence bias fields larger than M_{eff} are required to reach the cutoff frequency necessary to excite this propagation type.

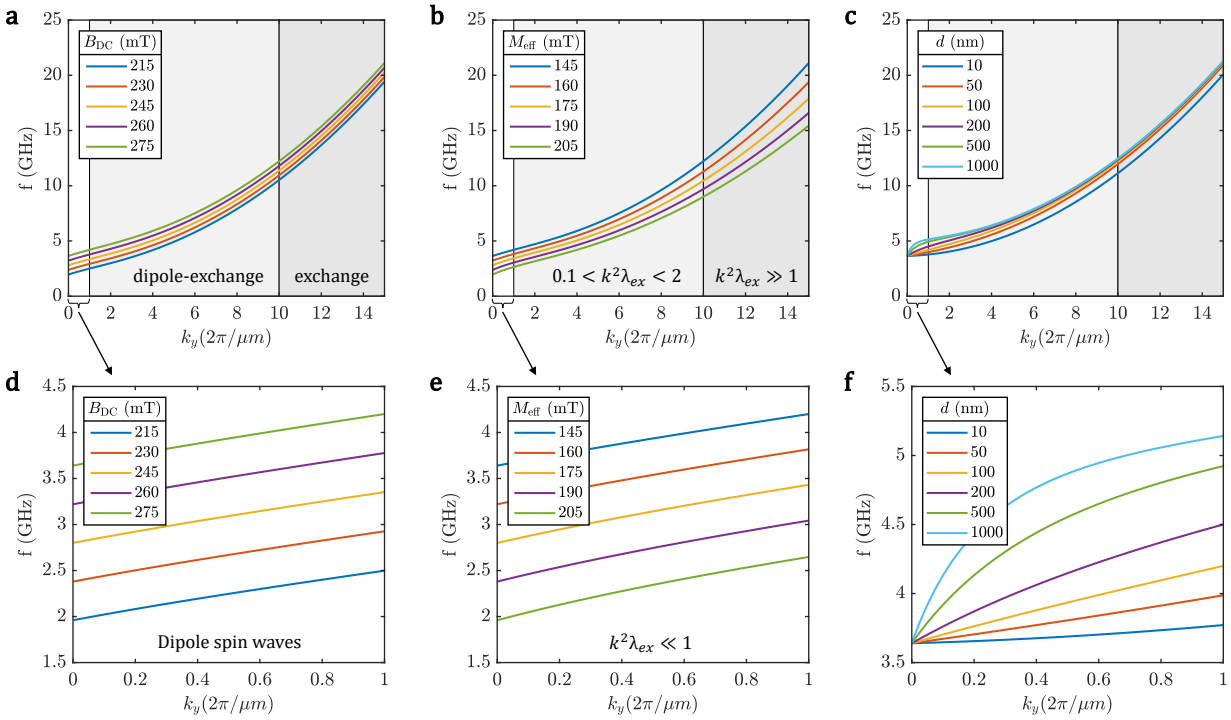

Figure 1.3 Forward Volume dispersion characteristics using typical material parameters of a YIG thin film. a-c) dispersion curves for a large k-range illustrating the influence of bias field (a), effective magnetization (b), and film thickness (c) on the curve shape. The propagation regimes are highlighted by the greyscale with respect to k. d-f) Magnification of the dipole regime (small k-range) showing the influence of magnetic parameters. Here, the slope is mostly determined by the thickness, field, and magnetization changes that cause quasi-linear shifts in frequency space.

Tangentially magnetized films: Backward Volume waves

Magnetostatic backward volume spin waves (BVSW) are excited when the film is magnetized in-plane $H \parallel \square$, and spin waves propagate in the direction of the effective field $H \parallel k$, whereby the dispersion is unaffected if the propagation is parallel or antiparallel to H. Due to the asymmetry of field and wave vector, these waves propagate isotropically, i. e. k becomes direction-dependent. Equ. 1.5 shows

the solution of the general dispersion relation for this particular propagation configuration [32], [33].

$$f_{BVSW} = \sqrt{f_H \left(f_H + f_M \frac{1 - exp(-kd)}{kd} \right)} \tag{1.5}$$

$f_H = \gamma \mu_0 H_{eff}$ and $f_M = \gamma \mu_0 M_s$. The main peculiarity of BVSW is the partially negative group velocity $v_g = \partial\omega/\partial k$, expressed by the slope of the dispersion curve. This configuration excites volume waves, the amplitude is sinusoidally distributed, but the group velocity points in the opposite direction (negative) than the phase velocity (positive), which is why this propagation type is called backward volume. An increase in k in the dipole regime is then associated with a decrease in $\omega(k)$. Due to the magnetization in the film plane, the magnetic easy axis of YIG, much lower bias fields are required to reach the cutoff frequency for BVSW, and the demagnetization can be neglected $f_H = \gamma \mu_0 H_{DC}$. For the inclusion of exchange contributions in the cutoff frequency, please refer to the FVSW section.

Tangentially magnetized films: Magnetostatic surface waves

Magnetostatic surface spin waves (MSSW), also known as the Damon-Eshbach mode (DE), are excited when the film is magnetized in-plane $H \parallel \square$, i. e. the easy axis, but spin waves propagate perpendicular to the effective field $H \perp k$. In contrast to volume waves, MSSW are localized to one of the film surfaces, and the precession amplitude distribution across the film thickness is exponential, with a maximum at the film surface. However, the group and phase velocities point in the same direction, consequently, MSSW are forward waves. Again, due to the broken symmetry of the field with respect to the surface, this type of wave exhibits anisotropic propagation and the solution of the dispersion relation shown in Equ. 1.6 [32], [33] is only valid for k_x, but invariant of the direction sign.

$$f_{MSSW} = \sqrt{(f_H + f_M/2)^2 - (f_M/2)^2 \exp(-2kd)} \tag{1.6}$$

The demagnetization in $f_H = \gamma \mu_0 H_{eff}$ can be neglected as the film is magnetized in the film plane and $H_{eff} = H_{DC}$. The direction/sign of k along the x-direction and that of H along the y-direction determine whether propagation happens on the top or the bottom surface and can be switched by a 180°. When the propagation direction is reversed, the concentrated fields shift from one side of the film to the other - this phenomenon is called field displacement non-reciprocity. However, in practical experimental systems, the film thickness is much smaller than the wavelength ($kd << 1$) and the amplitude distribution across the thickness can be assumed uniform [35]. As opposed to volume waves, there is only a single propagation mode on the surface instead of various thickness modes.

1.5 Magnon-based computing

Contemporary computing architectures work with electric charges as information carriers, and their controlled movement in modeled systems performs the computation. Integrated circuits of highest density are commonly based on complementary metal-oxide semiconductor (CMOS) technology, and hereupon built transistor-based logic gates cover the full spectrum of Boolean operations at low power levels. This technology has been continuously developed over the years, offering highest integration densities, and matured design guidelines at highly optimized fabrication efforts. However, on the road to device scaling, fateful power densities and leakage currents lead to reduced reliability and inefficiency, slowly but surely posing a dead end for this technology.

The field of Spintronics is one of many interesting beyond-CMOS computing alternatives, the electron spin is used as an information carrier instead of moving electric charge, making it particularly attractive because of the intrinsically low energy consumption of magnetic excitation and the absence of heat loss.

Spin-wave computing [7] uses wave-like magnetic excitations to perform computation and can be looked at as a subfield of Spintronics [36], [37] Spin waves are excited at high frequencies [38], and a compelling advantage over electromagnetic waves is their orders of magnitude smaller wavelength at microwave frequencies.

Numerous device concepts have been proposed and some experimentally realized, first and foremost accommodating for Boolean logic operations with spin-wave logic gates [39]–[42] as building blocks. The emerging spin-wave circuits are aimed to be embedded in existing CMOS environments to obtain hybrid computing systems that take advantage of computation tasks that are more efficient in the spin-wave domain.

Spin waves are wave-like oscillations of magnetic spins, and it only seems natural to take advantage of their powerful features in wave-based computing paradigms. In this case, the information is carried by the wave properties that are amplitude, frequency, and phase. Again, a number of promising non-binary architectures have been proposed, e. g. the concept of magnonic holographic memory [43] or a magnetic cellular nonlinear network [44].

Optical computing [45], [46], i. e. exploits the use of photons in visible light or infra-red beams to transmit and process information, but the digital format never became competitive to CMOS technology due to the reduced optical device integration density and photon confinement at small scales. With the emphasis on non-Boolean signal processing, spin waves could show a real advantage over photons due to their propagation characteristics, e. g. smaller wavelengths when used with the computational primitives of optics. This format of optics is often referred to as Fourier optics [47], and ideas on the magnonic version are given in Sec. 1.5.2.

1.5.1 Building blocks of spin-wave devices

The main functional blocks of spin-wave devices can generally be categorized into the input interface, the functional medium combined with the steering mechanism to alter the functionality, and the output interface. A general overview with a few common effects and utilized mechanisms is depicted in Fig. 1.4.

The simplest excitation mechanism is based on the magneto-electric effect using microwave transducers that directly creates a microwave magnetic field, and there have been various optimization efforts to explore and tune their wavelength efficiency [35], but also power efficiency as they are prone to have high insertion loss [48]. Other generation mechanisms use spin-polarized current [49] to exert torque on the magnetization, that can for example be realized via tunable spin-torque nano-oscillators [50].

Focusing on the functional medium, this incorporates the building blocks of spin-wave devices, in the most basic form this could be magnetic thin film or an assembly of waveguides [51]. There are many promising device concepts reaching from Boolean spin-wave logic over unconventional computing to quantum Magnonics. Examples are magnonic crystals [24], spin-wave transistors [8], majority gates, (directional) couplers [52], multiplexers [53], and even amplifiers [54]. Steering mechanism include the modification of any parameter that is part of the SW dispersion relation, e. g. current induced anisotropy changes [55].

To contextualize the efforts taken in this work, the employed methods are highlighted in purple in the text and specified in the circles next to the building block modules. The vision of this thesis is to show the potential of FIB as a manipulation technique of propagating spin waves, coherently excited by coplanar transducers, in the functional medium YIG, deployed as a refractive index modification and demonstrated with optically inspired spin-wave computing elements.

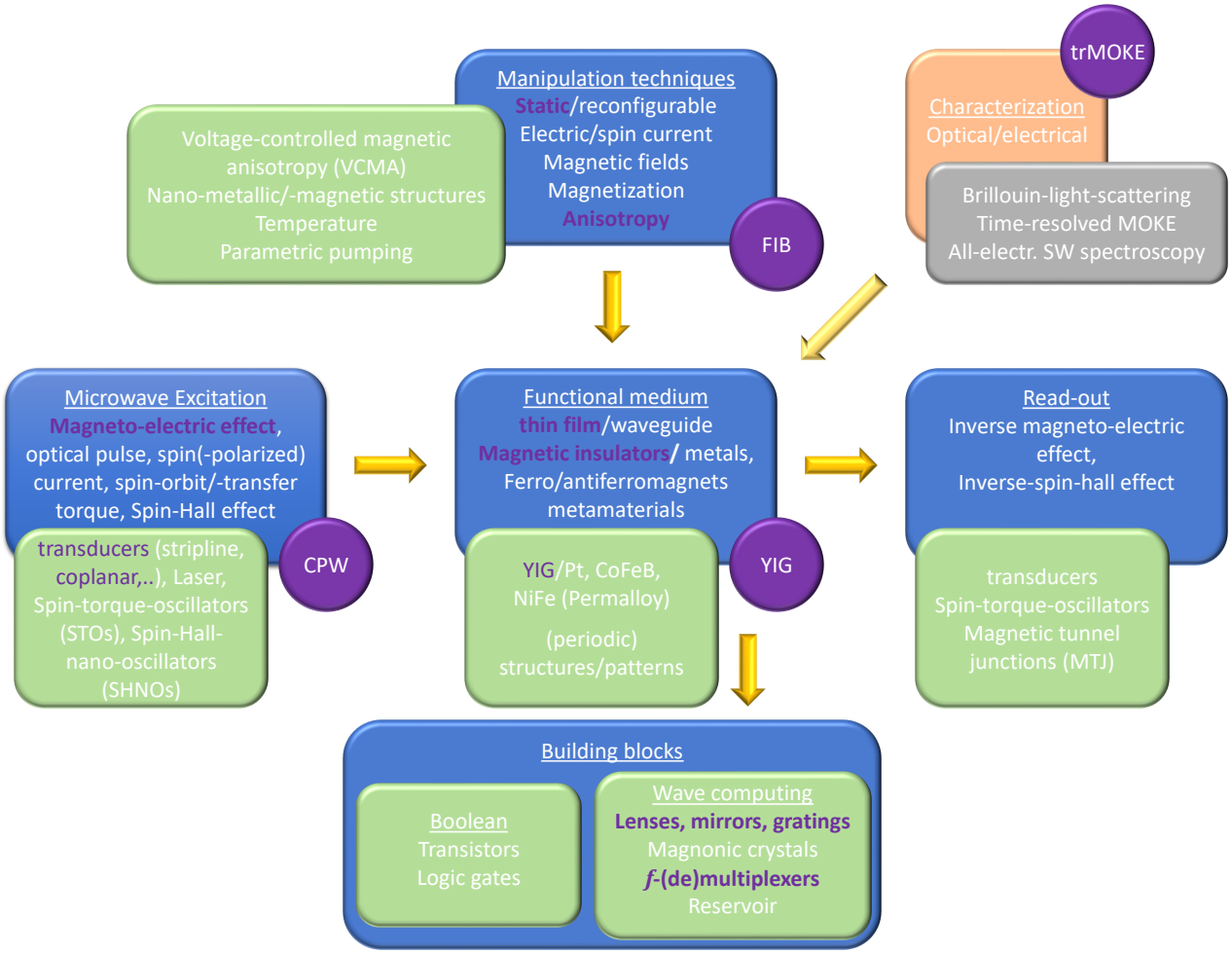

Figure 1.4 Mindmap of the functional blocks of spin-wave devices (blue modules), including exemplary effects and methods (green). Most efforts have been taken to study features and effects in functional media, which is obviously the part of highest complexity as it incorporates the essential building blocks. The simplest and most reliable excitation mechanism is provided by magneto-electric transducers, although exhibiting high insertion loss. SW read-out technologies are far from being reliable and efficient, and the shown characterization techniques (orange) are being used to study the wave properties, partly used as an attempt to design a successful read-out.

1.5.2 Optically inspired magnonic computing

An interesting route toward the usability of spin-waves as information carriers in signal processing tasks is to build the analogy to optical computing by adapting its principles to spin-waves while exploring their superiority to photons, represented in the subfield of "magnon optics" [56] or optically-inspired spin-wave computing [57]. This is not to confuse with "optomagnonics" [58], where the interaction between photons and magnons in solid-state systems is investigated.

There are two categories of optical computing, digital and analog, and we specifically focus on the analog format, hence exploiting the physical characteristics of waves and their interactions with optical devices. Analog optical computing (AOC) offers significant improvement in computational speed and efficiency in certain applications, e. g. pattern recognition, and allows parallel data processing due to the inherent attributes of light - photons are uncharged and do not interfere with each other as easily as electrons. The AOC architecture is established on the Fourier transform properties of a lens (Fourier optics), and promises the real-time processing of large data amounts that are represented in the amplitude and phase of a light wave [59]. The application of AOC in artificial neural networks found great popularity in recent years due to its enormous processing power [60], [61].

In magnon optics, spin-waves offer even richer dispersion features than light, the frequency-wavevector relation is inherently nonlinear and they can propagate anisotropically. The simplest way to replicate optical primitives is to use Forward-Volume spin waves, they exhibit isotropic propagation and their dispersion is quasi-linear in ultra-thin YIG films for small changes of k, the closest it can get to light, but in principle, this is also possible with spin waves of anisotropic nature [62], [63]. Like light, spin waves can be focused and diffracted by geometrical and refractive index modifications, whereby n can be modeled with any parameter that impacts the SW dispersion relation.

Besides replicating optical shapes like lenses [64] to perform Fourier transformations, a new factor of flexibility is offered by device designs aided by machine learning, as opposed to conventional design methods where a device is designed to deliver a dedicated output. A particularly useful method when using machine learning is the inverse design, whereby the desired output is defined at first, and the device performance is 'reverse-engineered'. The corresponding new subfield of inverse magnonics [65]–[67] is again inspired by optics, where the approach has been proposed for photons [68], [69], and it can be used for practically any spin-wave device, from binary data processing to more unconventional methods like neuromorphic computing. A full demonstration of an inverse-designed spin-wave component, namely an unconventional lens [3], from the training of magnetic parameters to the simulation of the machine-learned pattern over the experimental realization is shown in Chapter 5.

Adopting the principles of neural networks offers a new era of unconventional computing, it is possible to solve complex problems like classification and to perform pattern recognition of various data types. Neuromorphic computing needs special hardware to model complex levels of interconnections that imitate the function of the human brain , i.e. neuromorphic architectures with (artificial) neurons as information carriers. Exploiting wave computing paradigms appeared to be highly efficient in this manner when adding nonlinearities [70] to the system, which requires much less power when using spin waves [66], [71].

2 Experimental methods

2.1 YIG film fabrication and characterization

The fabrication of Yttrium Iron Garnet (YIG) thin films marks the beginning of the research project that is subject to this work. With the great help of Simon Mendisch, who used to be the fabrication expert in our group at the time, we managed to fabricate high-quality YIG thin films comparable to those used by leading researchers in the Magnonics community when used as a spin-wave medium [72]. The results were presented at the Magnonics conference in Brindisi, Italy in 2019 [73].

To suffer minimal damping, YIG is deposited onto Gadolinium Gallium Garnet (GGG) substrates, purchased from Saint-Gobain Crystals, due to the closest matching lattice constant. We use RF magnetron sputtering (Fig. 2.1) to fabricate thin films of the renowned configuration $Y_3Fe_5O_{12}$, and we obtained the best film qualities with a working pressure of 40 µbar and an RF Power of 100 W, resulting in a deposition rate of 6.6 nm/min. Sputter-deposited YIG is amorphous, and re-crystallization is achieved with a subsequent annealing process in an oxygen atmosphere at 700 °C for 4-8 hours with a ramp-up time of 10 °C/h and a cooldown of 1 °C/h.

In the experiments subject to this work, a film thickness $d = 100$ nm was chosen to maintain a stable and reproducible film quality. We fabricated samples down to $d = 50$ nm, but find the detection of spin waves to become tricky. As a quality indicator, we use the powerful characterization method of broadband Ferromagnetic Resonance (FMR), as it reliably determines magnetic parameters that are relevant to spin-wave dispersion and propagation length, and we obtain values of M_{eff} between 110 and 120 kA/m, and a Gilbert damping α_{G} from 0.0005 down to 0.0001. The measurement of an exemplary YIG thin film is shown in. Fig. 2.2. The physical film quality is certainly not as perfect as with LPE growth [74], especially at the interface to GGG (for details, see Fig. 2.8).

It is to mention that the films we find to allow the longest spin-wave propagation lengths possess a lower effective magnetization M_{eff} of around 115 kA/m than the intrinsic value of YIG (140 kA/m). At some point, we found the M_{eff} value of fabricated samples to drift to larger values, seemingly attributable to a crack in the target leading to gas enclosures and causing impurities. After the target was replaced, a working pressure of 8 µbar became the new sweet spot for optimal film quality in terms of magnonic performance.

For the electrical excitation of spin waves (SWs), shorted co-planar microwave antennas with center conductor S and gap G widths ranging from 2 to 5 µm are fabricated on top of the YIG film using a chromium mask and a negative photoresist (AZ MIR 701). Due to the limited resolution of the contact mask process, the lift-off of the 1 mm long antennas (excluding tapering) appeared to be too unreliable. For that reason, the excess parts of the electron-beam evaporated aluminum layer (300 - 400 nm) were etched off using a phosphoric acid-based etchant (TechniEtch Al80) with a rate of approximately 30 nm/min, which was found to be sufficiently selective to the YIG film underneath. As a side note, it turns out that crystalline YIG can hardly be etched with phosphoric acid, but amorphous (unannealed) YIG at a rate of about 10 nm/min.

We later gained access to a maskless aligner instrument, and thanks to Matthias Golibrzuch we do use this much more convenient lithography tool combined with a lift-off process ever since. Interestingly, we were also able to fabricate structures in YIG via lift-off with surprisingly clean edges, a technology that could be extremely useful for device fabrication. Johannes Greil will look into this in more detail during his doctoral project. As a side note, we never had access to an E-beam lithography writing tool, but due to the optical resolution limit of the trMOKE tool we are solely able to image dipole-dominated spin-waves ($\lambda > 1\mu m$) and there is not much point to fabricate thinner antennas that could excite shorter wavelengths.

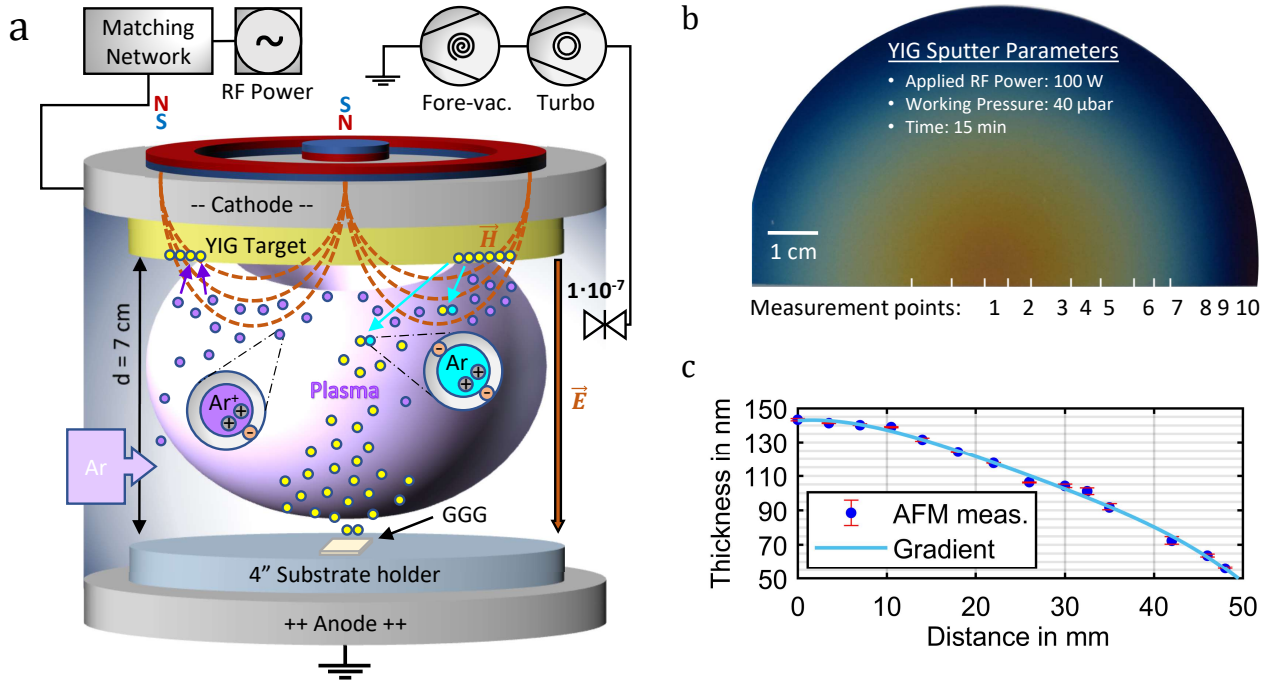

Figure 2.1 Sputtering process of Yttrium Iron Garnet. a) Sketch of the sputtering tool used for the thin film deposition. b) YIG deposited on a 4" silicon wafer to illustrate the radial sputter gradient. YIG was subsequently etched off alongside the edge with the marker points to measure the film thickness. c) AFM thickness measurement to determine the radial gradient. The deviation within the inner square centimeter is negligible. Note that the maximum thickness on the wafer is larger than on a single 1x1 cm chiplet, as it did not fit into the 1 cm deep dent of the sputtering plate, and therefore was closer to the target.

2.2 Time-resolved Magneto-optical Kerr Microscopy

Detecting magnetization changes of a medium can be accomplished by using the interaction with light (which is a propagating electromagnetic wave by definition) and investigating its property change in response to external forces that impact the magnetization such as the magnetic bias field. As a physical representation, the magneto-optical Faraday and the Kerr effect are of most relevance, as they are both first-order effects that denote the non-reciprocal polarization rotation of light by interaction with a magnetic field parallel to its propagation direction. Faraday rotation occurs when light transmits through a magnetic material, but the more practical effect to use when it comes to characterization is the Kerr rotation and ellipticity, which occurs when light is reflected from a magnetic surface. If light gets reflected at any interface below the surface, and transmits part of the substrate, the reflected signal will incorporate both, the Faraday and the Kerr effect.

The cutoff frequency of magnonic dispersion is usually in the gigahertz range with measurable wavelengths starting in the μm-range (see Sec. 1.4.1), and hence, time- and spatial resolution are needed to probe the fast change in the dynamic Susceptibility and to image its resulting wave vector in space. Furthermore, the dynamic magnetization components of interest ($\mathbf{m_x}$ and $\mathbf{m_y}$) in this work are in the film plane (FVSWs), and can only be detected if the light hits the sample surface at an angle. The Kerr effect is explored in a longitudinal fashion according to the sample-on-chip vs. objective geometry. The components that account for the aforementioned peculiarities are a pulsed laser beam

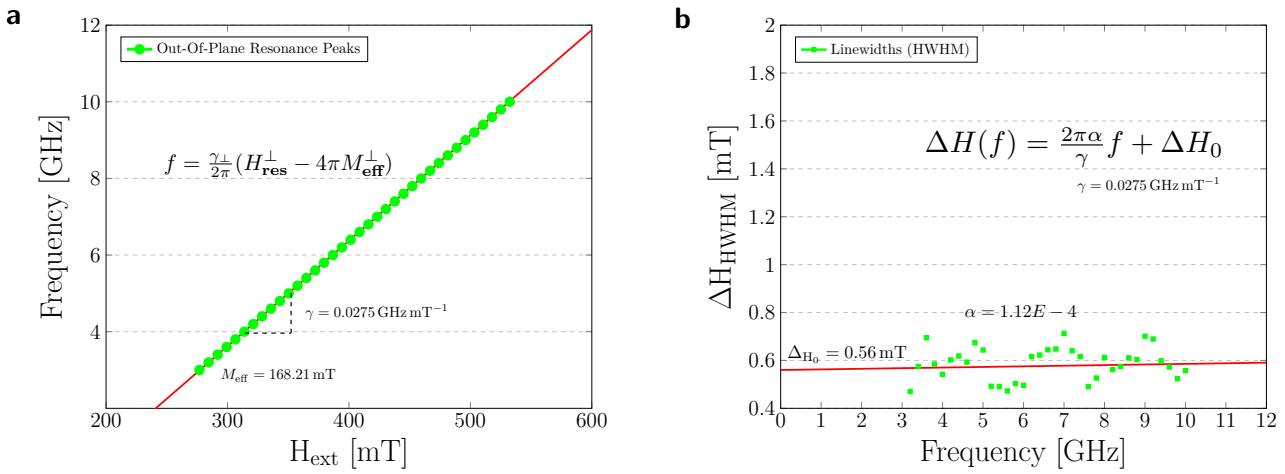

Figure 2.2 Characterization of an exemplary sputter-deposited YIG thin film by means of VNA-based ferromagnetic resonance. The optimal sputter parameters were found at a working of 40 μbar with 25 sccm Argon flow and 100 W microwave power, leading to a deposition time of 15 min for $d = 100\,\mathrm{nm}$. The ideal annealing procedure in O_2 atmosphere was found at 700 °C for at least 4 hours. a) Kittel fit of out-of-plane FMR peaks, indicating the effective magnetization and the gyromagnetic ratio. b) Damping fit α_G of the resonance field linewidths using the baseline-corrected magnitude of S_{21}.

($\lambda = 405\,\mathrm{nm}$) with picosecond resolution and μm x-y stage. The laser wavelength was chosen to obtain the largest magneto-optical response of YIG [75], but principally any wavelength with good enough Kerr contrast can be used.

This chapter explains the construction of the time-resolved magneto-optical Kerr effect microscope(trMOKE) designed and built by Ádám Papp during his Post-doc stay at TUM. Unfortunately, he did not have time for any documentation of his work before he left Munich in 2019, as we only managed to get the first working experimental results on YIG shortly before that moment in time. This chapter is not only the compulsory explanation of the measurement method but also aims to address potential questions of the interested reader that help to understand, operate, improve, and even built such a setup. The finishing of the trMOKE microscope laid an important foundation for the experimental work on spin-wave devices in our group and became a central part of our long-time collaboration with Adam Papp and György Csaba.

2.2.1 Functional Principle

To probe spin waves, which can be understood as orchestrated precessions of magnetic moments, one needs to detect the momentary, rotational phase of magnetization of at least two locations within one time period of precession $T = 1/f_{\mathrm{rf}}$ to fulfill the Nyquist sampling criterion. This is where the undersampling approach comes into play, and the procedure is illustrated in Fig. 2.3. The idea is to use short laser pulses (pulse width $< 1/2f_{\mathrm{rf}}$) at a repetition rate f_{rep} that is not only synchronized to the excitation signal f_{rf} but is also an integer divisor of it. The laser pulses are a downmixed version of the initial signal, which depicts the rotational state of magnetization by making use of the stroboscopic effect. To measure the precession in the down-converted signal electronically with preserved phase information, the laser pulses (or the excitation signal) are shifted by the amount of the lock-in frequency f_{lock}. This creates the reference points for a coherently occurring phase in a further down-converted signal, that can be sampled and demodulated at this very lock-in frequency.

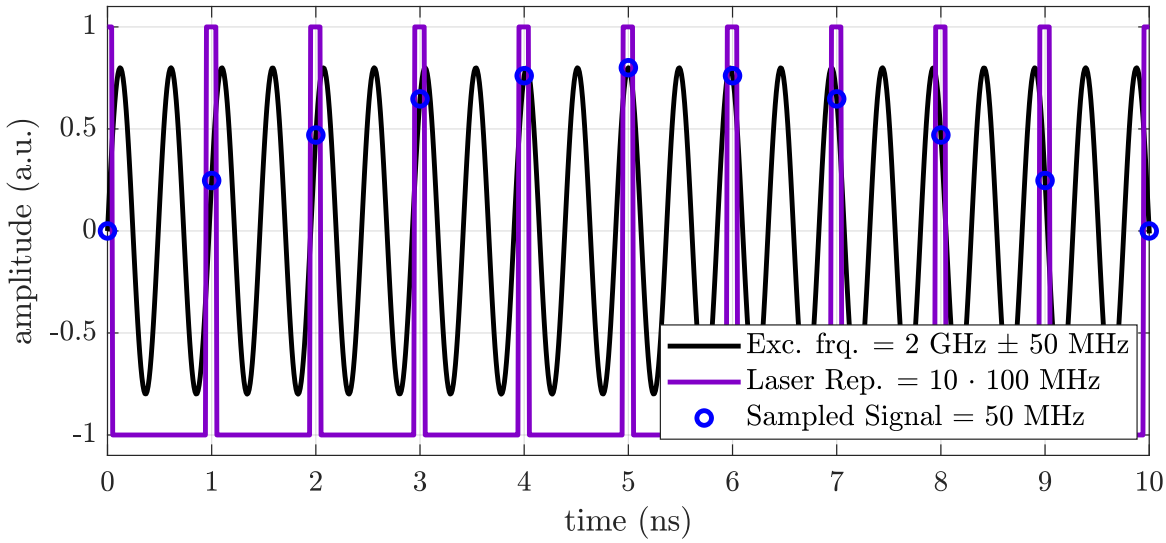

Figure 2.3 The principle of stroboscopic undersampling in the time domain. For illustration purposes, the pulsed laser signal, here 100 MHz, is up-mixed to 1 GHz. The lock-in shift (also increased by a factor of 10 for better demonstration) enables reconstructing the initial signal (here 2 GHz) at a very low sampling frequency.

Consequently, the undersampling condition requires that

$$f_{\mathrm{rf}} = n \cdot f_{\mathrm{rep}} \pm f_{\mathrm{lock}} \tag{2.1}$$

which limits the minimum frequency step size to

$$f_{\mathrm{step,min}} = f_{\mathrm{rep}} \pm f_{\mathrm{lock}} \tag{2.2}$$

This is a special constellation of a time-resolved MOKE measurement that is also referred to as Super-Nyquist Sampling [76], it represents an extreme case of undersampling where the excitation source does not have to be modulated. Furthermore, the real and imaginary parts of the magnetization are measured contemporarily in contrast to conventional modulation approaches, where they are measured consecutively with a delay stage for the laser pulses.

2.2.2 Setup Components and Schematic Overview

The tr-MOKE setup was built under economical constraints, mostly instruments already available in the lab were used, and only inevitable parts such as the picosecond laser (Taiko PDL-1) were purchased. The foundation consists of a Zeiss microscope with a 3-axis (x-y-z) micrometer stage and a 100x magnification objective. Spin waves in the YIG film are excited by feeding the microwave antennas with the RF source (SRS386) through the chip carrier (photograph in Fig. 2.5) in combination with a DC bias field H_{dc} normal to film plane provided by a strong Neodymium permanent magnet underneath. Their wavelength is conditioned by the combination B_{dc} and f_{rf} according to the Forward volume dispersion relation (Sec. 1.4.2).

The RF source serves as the clock provider (10 MHz) for the laser trigger and the lock-in amplifier. The 405 nm laser is pulsed by an integer-N phase-locked loop (ADF4351 PLL board) that is again synchronized to the clock master. Typically, this is done at a 50 MHz repetition rate as this has proven to lead to a good signal-to-noise ratio, but the laser driver unit principally allows external triggers up to 100 MHz repetition rate that can be easily changed with the PLL board.

The laser beam is guided through an arrangement of optical elements that control its path: first, the incident beam is linearly polarized before it is directed close to the lateral edge of the microscope

objective with the purpose to hit the sample at an angle. Hereby, the beam is rerouted with dichroic mirrors that allow the ambient light of the microscope lamp to transmit, enabling vision on the sample surface with the camera. As a next step, the beam is reflected from the sample surface symmetrically to the incident angle and guided back through the mirrors parallel to the incident beam. A d-shaped mirror is used to separate the reflected beam and routes it to a $\lambda/2$ waveplate that rotates the polarization plane. The Wollaston prism separates the beam into two orthogonally polarized components at an angle of 20 degrees, and adjusting the prism's radial orientation is used to align the two beam parts horizontally to the balanced diodes of the photodetector (Thorlabs PDB450A, AC-coupled). The signal is balanced to equal intensity by adjusting the polarization plane ($\lambda/2$ waveplate).

The photodetector takes the difference between the two signal components that incorporate the Kerr rotation and also amplifies it. This amplification is switchable and needs to be set according to the bandwidth of the signal to be sampled by the lock-in amplifier (Zurich instruments MFLI) at the intermediate (or alias) frequency f_{lock}. An overview of the setup arrangement is shown in Fig. 2.4.

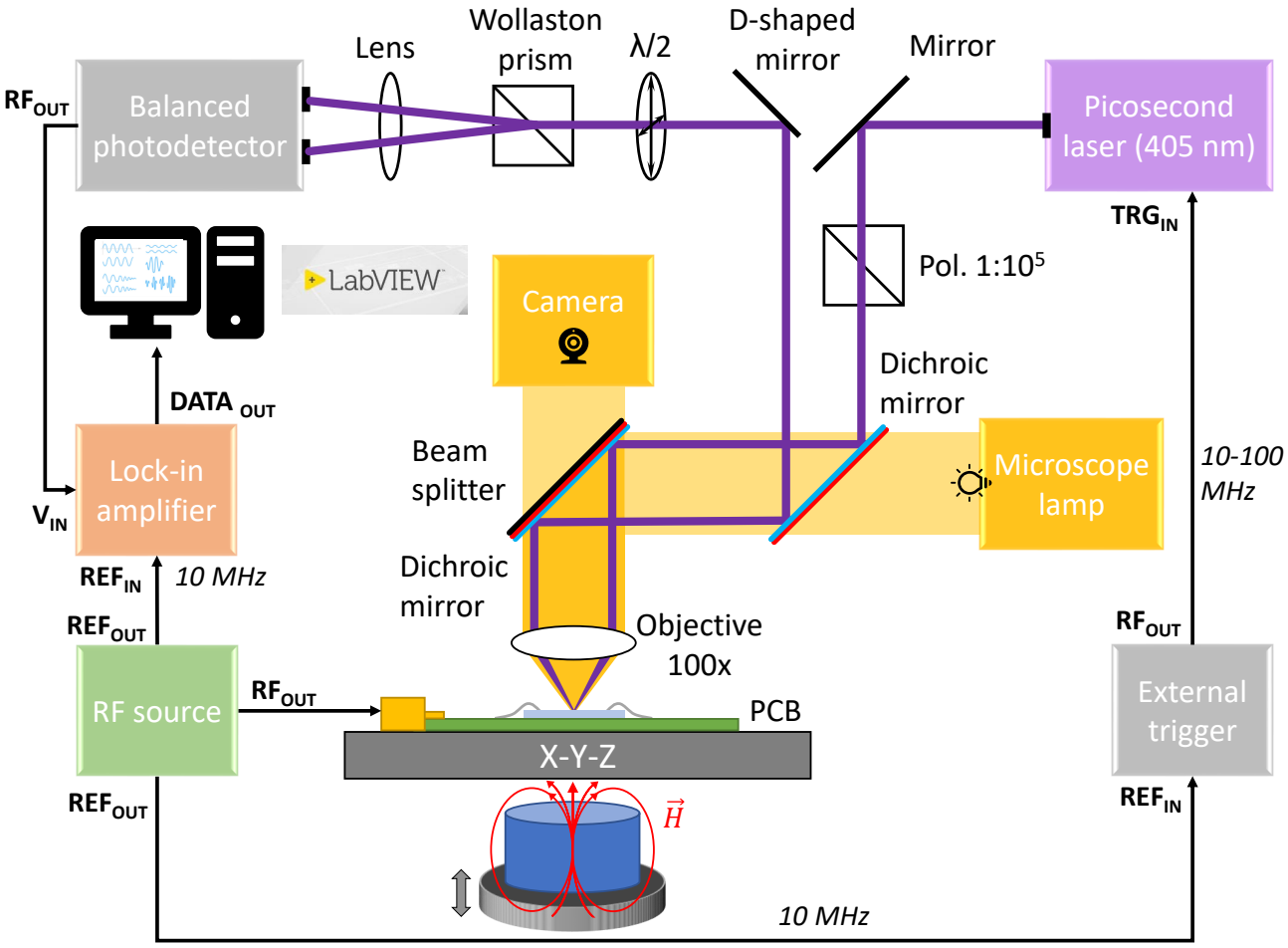

Figure 2.4 Schematic overview of the setup arrangement of the in-house developed time-resolved MOKE microscope, initially built by Ádám Papp. The laser optics are attached to a Zeiss microscope, wherein the beam is guided to the surface of the YIG sample (bonded to the PCB) at an angle. The longitudinal MOKE effect is necessary to probe the Forward Volume spin wave configuration, as the dynamic magnetization components m_x and m_y are in-plane.

For the out-of-plane bias field, a height-adjustable (motorized) permanent magnet underneath the

sample is used due to limited space and for simplicity. Off-axis stray fields make the alignment normal to the sample cumbersome and can cause deviations in the expected focal distances and diffraction angles of the presented elements due to portions of anisotropic wave components. This limitation is caused by the physical constraints with the out-of-plane bias field: a second (electro) magnet pole would collide with the microscope objective.

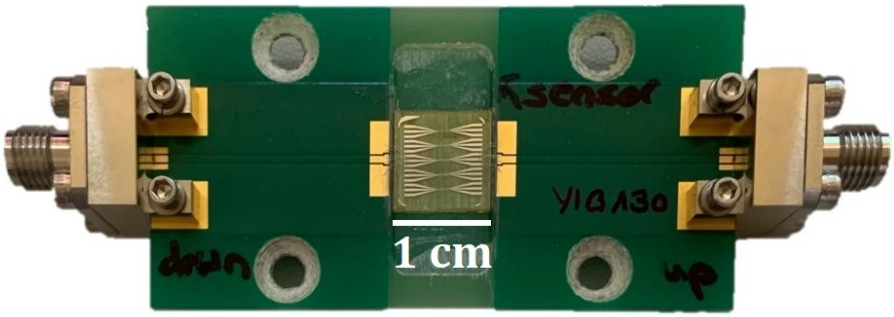

Figure 2.5 Photograph of a YIG sample mounted to the chip carrier. The microwave antennas on the sample are wire-bonded to the coplanar leads (roughly impedance matched) on the printed circuit board and can be connected to the RF source with the edge launch connectors. The chip carrier is large enough to fit the 100 x objective and is screwed to the X-Y stage when in operation.

The smallest detectable wavelength (currently about 1 μm) depends on multiple factors in the system. First and foremost, the X-Y micrometer stage (Ludl) has a minimum scanning step size of 0.4 µm, thus limiting that spatial resolution to about 1 μm on that end. The spatial resolution is ultimately restricted by the optical diffraction limit, and hence the minimum laser spot size. The minimal achievable focal spot size on the sample is about 1-2 μm^2 with the optics currently in use, which could potentially be improved by using additional lenses.

The largest detectable frequency is limited by the pulse width of the picosecond laser to $f_{\mathrm{max}} = 1/2p_{\mathrm{min}}$. The laser head (PicoQuant LDH-I Series) can produce pulses with a full width at half maximum (FWHM) of 50 ps at a laser power level of 10%, which is used in measurement mode, and hence the maximum excitation frequency is 10 GHz. As discussed earlier, the alias frequency used in the undersampling technique conquers the minimum frequency step size limitation in the amount of the laser repetition rate f_{rep} that is present in conventional trMOKE setups. Given the condition in Equ. 2.1 it becomes obvious that an infinitely small frequency step size is only feasible if the lock-in (and the photodetector) bandwidth is $\geq f_{\mathrm{rep}}/2$. Since the lock-in amplifier integrated into the setup has a maximum bandwidth of 5 MHz, the minimum frequency step size at f_{rep}=50 MHz would be 40 MHz. The laser driver (Taiko PDL M1) allows adjusting f_{rep}, but fewer repetitions result in losing a significant amount of signal. Spin waves have been successfully detected with f_{rep}=10 MHz by simply using the system clock as a trigger to accommodate the 5 MHz bandwidth limit of the lock-in amplifier when aiming to do frequency sweeps. This implies a minimum frequency step size of $f_{\mathbf{step,min}} = 5\,\mathrm{MHz}$ for $f_{\mathbf{rep,min}} = 10\,\mathrm{MHz}$, but a low repetition rate causes a significant loss of signal. For the experiments in this work, we used $f_{\mathbf{rep}} = 50\,\mathrm{MHz}$, but any wavelength within the optical detection limit and the antenna efficiency spectrum can be set by fine-tuning the height of the permanent magnet. The 2D SW patterns are recorded by stepping across the area with the x-y stage (0.4 µm step size), and with a dwell time of 0.5 s per step, scanning an area of 60x60 µm takes about 3 hours.

2.3 Magnetic parameterization of the FIB effect

In an early experiment, an entire YIG film has been irradiated with consecutively increasing ion doses, and the change of the ferromagnetic resonance (FMR) field was measured after each irradiation step. A change of the resonance field can be attributed to a change of the effective magnetization according to Kittel's equation [77]. For the in-plane configuration ($H_{\text{eff}} \parallel \square$), the relationship is

$$\omega_{\text{FMR}} = \gamma\mu_0\sqrt{H_{\text{eff},\parallel}(H_{\text{eff},\parallel} + M_{\text{eff},\parallel})} \tag{2.3}$$

with

$$\mu_0 M_{\text{eff},\parallel} = \mu_0(M_\text{s} - H_\text{a}) = \mu_0 M_\text{s} - \frac{2K_{\text{u},\parallel}}{M_\text{s}} \tag{2.4}$$

The anisotropy term $K_{\text{u},\parallel}$ in this orientation has a positive sign, hence it reduces the demagnetization contribution in this direction. For simplicity, the uniaxial anisotropy is assumed to have the main contribution to deliver the idea of how demagnetization can be affected, but the anisotropy field H_a can contain other components and their respective orders of contribution, such as crystalline and interfacial anisotropy [78]. In the out-of-plane configuration ($H_{\text{eff}} \perp \square$), the dependence resonance field on M_{eff} becomes linear

$$\omega_{FMR} = \gamma\mu_0(H_{\text{eff},\perp} - M_{\text{eff},\perp}) \tag{2.5}$$

with

$$M_{\text{eff},\perp} = \mu_0(M_\text{s} - H_\text{a}) = \mu_0 M_\text{s} - \frac{2K_{\text{u},\perp}}{M_\text{s}} \tag{2.6}$$

The sign of anisotropy term $K_{\text{u},\perp}$ becomes negative when the film is magnetized perpendicular to its surface and adds to the demagnetization field, explaining the need for higher fields in this orientation.

The resonance fields of two step-by-step irradiated YIG thin films with a thickness of $d = 100\,\text{nm}$ and $d = 60\,\text{nm}$, for the frequency of 9 GHz are shown Fig. 2.6, whereby the top row shows in-plane and the bottom row out-of-plane FMR measurements. The cumulative dose is assumed to be identical to the irradiation at a high dose in one run. The resonance field generally increases for small ion doses and decreases again when the "turn point" dose is reached.

For the out-of-plane configuration (Fig. 2.6b and d), this happens at a dose larger than $6{\cdot}10^{12}$ ions/cm^2 ($d = 100\,\text{nm}$) and at an even lower one for $d = 60\,\text{nm}$, thereafter the amplitude decreases significantly. In this orientation, a change of the resonance field is linearly dependent on the effective magnetization $M_{\mathbf{eff}}$ according to Kittel's equation, and the measured change of the resonance field ΔB_{FMR} of about 2-3 mT is in good agreement with the results on the FVSW wavelength change detected in this ion dose range Fig. 3.2, and the resulting $M_{\mathbf{eff}}$ change of about 1.5 % from 146.7 mT to 148.2 mT, fitted numerically using the dispersion curves.
Interestingly, the turning point of the resonance field change happens at a larger dose when the film is magnetized perpendicular to the film plane (Fig. 2.6a and c). We did not investigate the impact on spin-waves in the geometry, we only conducted experiments with FVSW focused on isotropic wave propagation. Here, the anisotropy contribution most likely has a different composition as a result of the ion irradiation.

Due to the ion implantation depth limit of Ga^+ in YIG of about 24 nm (see TRIM simulation in Fig. 4.5), the thin films used in the presented experiments are only partly "doped" in their top layer. Therefrom, it is intuitive to assume that a change in the film thickness also contributes to the modification of the spin-wave wavelength, especially since the change with ion dose is non-linear. To classify the effect for spin waves, the dispersion relation [28] dependence on $M_{\mathbf{eff}}$ and the film thickness are shown in Fig. 2.7b, c at experiment-relevant values, respectively. From here, it becomes obvious that the dispersion relation is quasi-independent of thickness for $k = 0$, as opposed to $M_{\mathbf{eff}}$ in Fig. 2.7c,

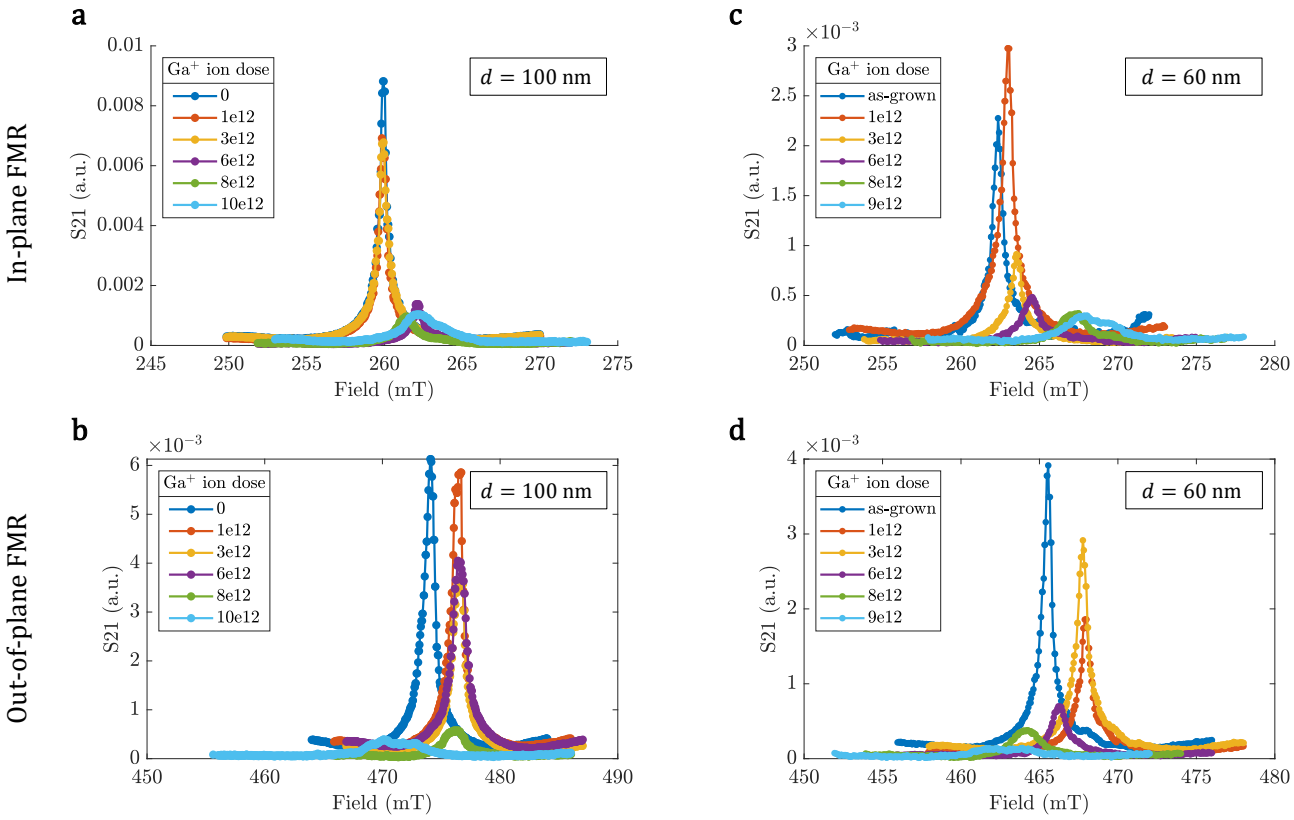

Figure 2.6 Ferromagnetic resonance fields B_{FMR} of consecutively ion-beam irradiated YIG thin films with different thicknesses (60 and 100 nm) at the indicated doses, shown for f = 9 GHz in all cases. In the in-plane configuration (a and c), B_{FMR} increases up to the range of ion doses shown, although with a clear decrease in signal amplitude. The steadiness seen in the low doses in (a) is most likely a measurement inaccuracy. The relative field shift ΔB_{FMR} is slightly larger for the thinner film in (c). At doses larger than depicted, B_{FMR} starts to decrease again (not shown for overcrowding reasons). When the films are biased perpendicular to their surface (b and d), the resonance field increases for low doses by about the same amount ΔB_{FMR}, but already decreases at lower ion doses.

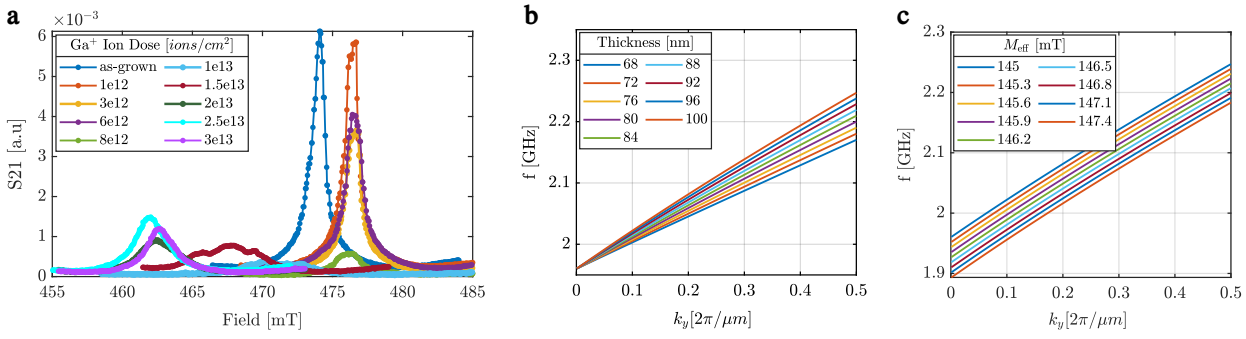

Figure 2.7 Considerations supporting the chosen parameterization of the FIB effect in YIG. (a) Ferromagnetic resonance measurements (f = 9 GHz) of a 100 nm thick YIG film incrementally irradiated at the indicated ion doses. The resonance field changes in response to the irradiation, which can be attributed to a change of $M_{\mathbf{eff}}$. (b) Spin-wave dispersion relation [28] dependence for a change of the film thickness. The parameters for an exemplary YIG film from FMR are used: $M_{\mathbf{eff}}$ = 145 mT, $H_{\mathbf{DC}}$ = 215 mT. (c) Spin-wave dispersion relation dependence (forward volume) for a change of the magnetization, t = 100 nm, $H_{\mathbf{DC}}$ = 215 mT.

hence a thickness change of the film would be invisible in the FMR measurements. For that reason, we believe the modeling of the magnetic parameter change induced by FIB using M_{eff} is justified, at least for the low dose regime exploited in the experiments. Fig. 2.7a shows the continuation of the measurement in Fig. 2.6b after the turning point. After the FMR signal vanished almost completely for a dose of $1 \cdot 10^{13}$ ions/cm^2, it seems to "wake up" again for higher ion doses, and we are currently investigating this high-dose range to possibly achieve a larger change of the magnetic properties by using a 'negative' irradiation, i. e. irradiating the surroundings of SW components instead of the structures themselves. In this dose regime, the thickness could actually play a role, supported by the ion-dose-dependent transition of the YIG texture from crystalline to amorphous (Fig. 2.8).

It is worth mentioning that the FMR measurements of the consecutively irradiated films are not perfectly precise, slight displacements of the samples on the waveguide can cause bias field variations leading to inaccurate resonance fields, and the amplitude can be affected by imperfect contact. Nonetheless, the overall trend of change can be clearly identified, and the results are absolutely supporting the investigations on the FIB effect on YIG. At this point, I would also like to thank Carolin Calcagno for her help with these time-consuming experiments.

Impact of ion-beam irradiation on the crystal level

The average penetration depth of 50 keV accelerated Ga^+ ions in YIG is estimated to be 24 nm according to SRIM simulations [79], meaning only a part of the total film thickness (100 nm) is affected by the ion irradiation. The observed magnetization change is likely a complex combination of multiple effects, mainly the anisotropy change due to dislocations in the YIG crystal structure leading to strain-induced anisotropy, and the interaction with the interface to the underlying film part (and with the underlying layer itself).

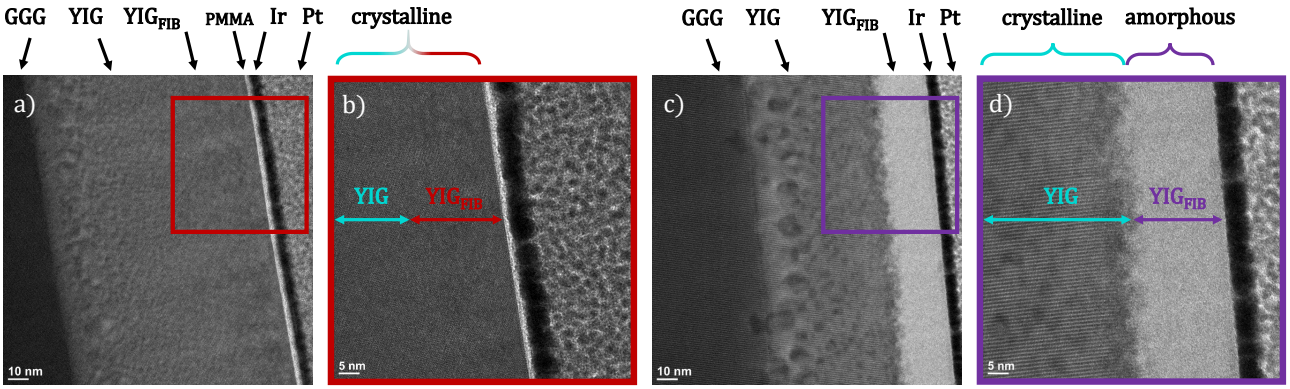

Figure 2.8 TEM images of FIB irradiated YIG thin films. (a) Cross-section of a YIG thin film irradiated at $1 \cdot 10^{13}$ ions/cm^2 and (b) snippet of (a) showing the top part and the expected ion implantation depth indicated. The crystallinity of YIG is preserved. (c) Irradiation impact in YIG at a higher dose of $1.3 \cdot 10^{14}$ ions/cm^2 and (d) snippet of (c) revealing an amorphous top layer down to approximately 25 nm from the surface.

To get insight into the structural properties of YIG, and more importantly, into the physical influence of Ga^+ ion irradiation, we imaged irradiated thin films with transmission electron microscopy (TEM). For a dose regime of 10^{12} to the lower 10^{13} ions/cm^2, where M_{eff} is modified with only a moderate increase in damping, there is no visible crystalline damage in YIG (Fig. 2.8.a, b). At the interface to GGG, coarse structural bumps can be recognized, which could come from the high working pressure used during sputtering or an imperfect GGG surface, leading to a reorientation of growth direction. We neither think these are voids since the crystallinity inside of them is visible nor that they have

anything to do with the ion irradiation since it does not reach that far. We do notice that these defects appear even stronger in the sample shown in Fig. 2.8.c, d, which is most likely due to a skipped sputter-cleaning step of the GGG. The ion dose is an order of magnitude higher (10^{14} ions/cm^2), and spin waves are not detectable anymore with our measurement tools. The top layer of the 80 nm thick YIG film has turned amorphous, whereby its thickness (25 to 28 nm) is close to the expected ion-implantation depth. In principle, spin waves could be able to travel underneath, but the uncontrolled interface of unknown width might just add to the degree of destruction.

The demonstrated physical properties of the two ion dose regimes can be used for spin-wave steering in different ways, i. e. the low dose for tuning the relative magnonic refractive index and the high dose to suppress spin-wave propagation locally. Studying the underlying cause of the ion-dose-dependent change of M_{eff} deserves its own study and is beyond the scope of this work. Interestingly, we found that the effect of FIB manipulation in YIG can be nearly reversed by recrystallization via high-temperature annealing (the resonance frequency shifts back close to the initial value). Again, this needs much more investigation and such a process step would not be practical in terms of reconfigurability.

2.4 Design and fabrication details of FIB structures

Refractive index n modifications can be achieved with low ion doses, and a convenient way to achieve smooth transitions of n is changing the filling factor in the pixel space of the FIB image (i. e. halftoning). This way, only one global dose is applied, which means the beam current does not have to be changed pixel-wise. The effective ion dose is equivalent to the filling ratio, presuming that the spin-wave wavelength is much larger than the pixel size, e. g. a filling of 50% is half of the applied dose. Fig. 2.9.a shows an illustration of the effect. (It is important to mention that 50% filling does not directly mean 50% M_{eff} change (see Fig. 3.2.d) because of the non-linear relation between the two.) With this approach, we can realize magnetization landscapes with a resolution up to the minimum pixel size of the FIB image (10 nm). Furthermore, we can use the length of irradiated regions to create phase changes as desired, as shown in Fig. 2.9.b, and we used this example to choose the length for the phase plate in Fig. 3.4.a (6 µm should be approximately 180 °). The dwell time is used to set a specific dose per pixel, which is usually on the low µs timescale, and irradiating an entire image takes less than a minute.

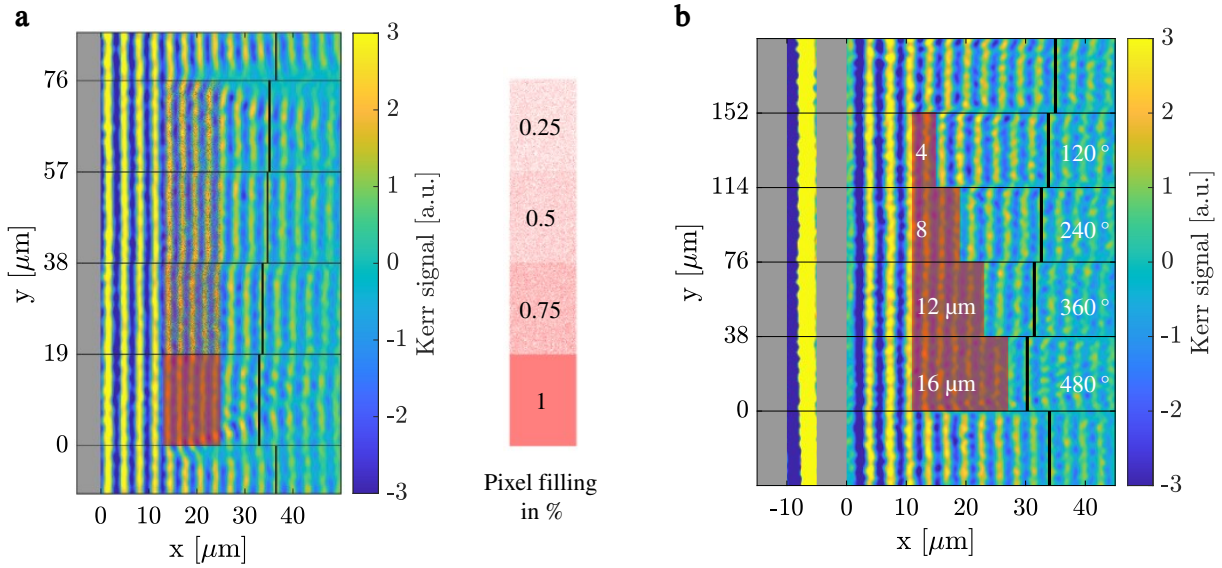

Figure 2.9 Dose and geometry driven M_{eff} patterning in YIG. (a) Demonstration of different filling factors and the resulting (small) wavelength change, highlighted by the indicated phase shift after the irradiation areas. (b) Phase change demonstration of spin-wave propagation through irradiated areas of different lengths.

3 Publication #1: Spin-wave optics in YIG realized by ion-beam irradiation

This chapter is a full reprint of the published article
M. Kiechle, A. Papp, S. Mendisch, *et al.*, "Spin-wave optics in yig realized by ion-beam irradiation", *Small*, p. 2 207 293, 2023. DOI: 10.1002/smll.202207293.
The experiments shown in here express the potential of the developed fabrication process for spin-wave devices using direct FIB irradiation to modify the magnetic properties of YIG locally. This is demonstrated by various flavors of optically inspired computing components for spin waves in the discovered operation ranges with respect to the ion dose.

3.1 Abstract

We present direct focused-ion-beam writing as an enabling technology for realizing functional spin-wave devices of high complexity, and demonstrate its potential by optically-inspired designs. It is shown that ion-beam irradiation changes the characteristics of YIG films on a submicron scale in a highly controlled way, allowing one to engineer the magnonic index of refraction adapted to desired applications. This technique does not physically remove material, and allows rapid fabrication of high-quality architectures of modified magnetization in magnonic media with minimal edge damage (compared to more common removal techniques such as etching or milling). By experimentally showing magnonic versions of a number of optical devices (lenses, gratings, Fourier-domain processors) we envision this technology as the gateway to building magnonic computing devices that rival their optical counterparts in their complexity and computational power.

3.2 Introduction

A major motivation behind magnonics research is to replicate the functionality of bulky optical components in chip-scale devices that are amenable to integration with microelectronic circuitry [47], [56], [80]–[84]. This way, the functionality of coherent optical computers could also be cloned in the magnonic domain. Spin waves (SWs) display interference phenomena that resemble that of optical waves, but they offer submicron (possibly sub - 100 nm) wavelength and can be launched and detected by electrical means. Chip-scale optically-inspired devices also provide a pathway to much needed energy-efficient neuromorphic and edge-AI computing components [65], [66].

It has, however, remained elusive to produce spin-wave optics that approach the 'ideal' behavior of optical components. This is largely due to the fact that so far no practical technology has been demonstrated to control the propagation characteristics of spin waves to the extent that is possible in optics. Ideally, one would want to realize any fine-grained spatial distribution of the index of refraction, as this provides a high degree of freedom in device design.

Magnonic devices are almost exclusively made from yttrium iron garnet (YIG) substrates, having low attenuation that enables propagation over long distances. Lithographic patterning of YIG films allows defining some spin-wave optic functions [85] but has technological challenges [14], [86], as etched or milled film edges introduce undesired behaviors [11]. Even a well-controlled YIG patterning technology would be insufficient to replicate the propagation of electromagnetic waves, which propagate in vacuum, and optical devices can be made by patterning a transparent material to an

appropriate shape. Essentially, refractive spin-wave optics need additional materials or intrinsic YIG film modifications, as magnons do not propagate in air.

A few pathways have been proposed to realize engineered YIG substrates. It is possible to use localized magnetic fields to steer spin waves [87], but this requires a second magnetic layer to generate the fields and arbitrarily-shaped field profiles cannot be realized. Previous work has shown the use of heat distributions [62] to generate refraction-index profiles, a solution likely impractical in chip-scale devices. Local exchange bias may also be used for magnonic optics [88], but so far this works only on metallic systems, which are highly-damping in nature.

In multilayered magnetic systems, it is well established that focused ion beam (FIB) irradiation modifies the magnetic properties [15], [18] without actually removing material or creating edges. The FIB irradiation affects magnetic properties on a sub-50 nm size scale, which is a resolution that is hardly achievable by the combination of lithography and etching. The effect of FIB on magnetic multilayers motivated our work to study the effects of direct FIB-ing on the magnetic properties of YIG. Using 50 keV gallium ions (Ga^+), the applied ion doses are chosen to not physically remove material, but to implant Ga^+ into the YIG thin film and locally alter the crystalline structure.

In our work, we first demonstrate the effect of FIB irradiation on spin waves in YIG for plane-wave propagation and characterize the dependence of magnonic wavelength on FIB dose, obtaining an index of refraction n. Lenses and diffraction gratings are designed with a binary irradiation pattern – in a similar fashion to elementary optical devices, where light propagates either through glass or vacuum.

We find that the effect of FIB irradiation on YIG films can be modeled adequately by assuming an effective magnetization value $M_{\mathbf{eff}}$ that varies with the FIB dose, which is in agreement with the findings in another work [16]. The locally changed $M_{\mathbf{eff}}$ results in a local change of the wavelength, which, in turn, may be modelled as a spatially varying index of refraction n. As a consequence, FIB irradiation allows the realization of (almost) arbitrary two-dimensional n profiles.

Going beyond binary patterns, we demonstrate that FIB irradiation is especially useful for graded-index (GRIN) magnonics [57], [89] as it allows a continuous and high-resolution variation of n across the film surface. As a highly meaningful example of such systems, a **4f** Fourier-domain signal processor is shown in Sec. 3.4. The demonstration of a **4f** system opens the door to the realization of a variety of optically-inspired computing systems [90] using magnons. We envision that the FIB technology shown here will readily provide access to magnonic devices that may rival on-chip optics in their functionality, and consequently act as the gateway to magnonic integrated circuits (in analogy to photonic ICs). While spin waves have limitations, such as damping that should be compensated by some amplification mechanism for large-scale devices, they have benefits, such as nonlinearities [66], [91], that open up applications unreachable for photonic ICs.

3.3 Experimental methods

The effect of focused ion beam (FIB) irradiation is characterized by recording the spin-wave (SW) waveform using longitudinal time-resolved magneto-optical Kerr effect microscopy (trMOKE) and determining the SW wavelength change at various ion-dose levels. Fig. 3.1 gives an overview of the experimental techniques used for fabrication and metrology. An in-house sputter-deposited YIG thin film (thickness t = 100 nm) with co-planar microwave antennas (signal, gap width S, $G = 2$ - 5 µm) is bonded to a PCB board from where it is fed with a microwave signal. Areas next to the excitation antennas are FIB-irradiated at different ion doses and shapes. Fabrication details can be found in Sec. 2.1. Subsequently, 2D spin-wave patterns are imaged with a longitudinal, time-resolved Kerr microscope in forward volume configuration. The scale bar in all these images represent the Kerr signal of the trMOKE microscope, and are scaled in arbitrary units. The signal amplitude is not calibrated, so these values cannot necessarily be directly compared. In our custom-built trMOKE apparatus (detailed description in Sec. 2.2) the film is magnetized out-of-plane (along M_z) and the dynamic m_x and m_y components display wave propagation. The FVSW mode is isotropic

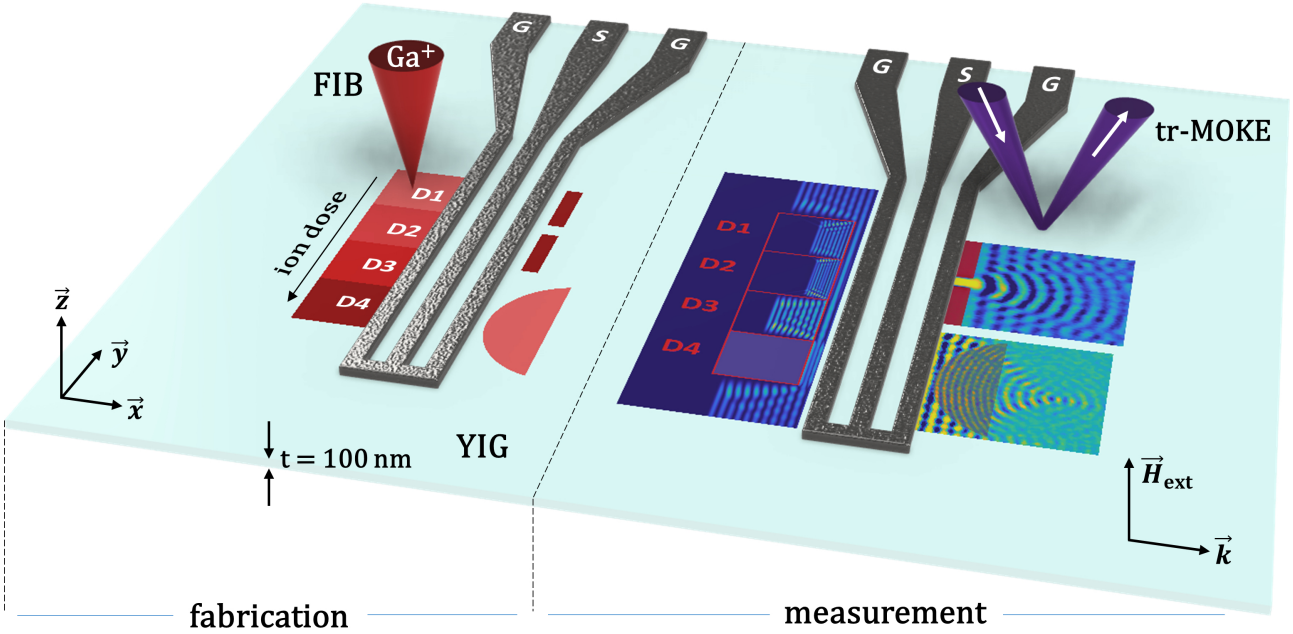

Figure 3.1 Representation of the experimental arrangement. Left part: areas in YIG next to the excitation antenna are directly irradiated with FIB at different ion-dose levels (indicated by the intensity of the red color), and an ion-dose dependent change of M_{eff} is found. This is used for the application examples: a lens at a low dose with a modified n and a single slit at a high dose. Right part: spin-wave propagation patterns in the FIB-irradiated regions are imaged with trMOKE.

and therefore shows the closest analogy to optical wave propagation. The spatial resolution of the trMOKE is limited to about 0.4 µm due to the smallest possible step size of the x-y stage, as well as the optical diffraction limit of the applied laser lightsource and the objective lens, limiting the shortest detectable spin-wave wavelength to about $\lambda = 1$ µm. The FIB pixel size (beam diameter + dwell space) can be as small as 10 nm, meaning the writing technique can be applied to small-scale geometrical shapes way beyond the optical detection limit.

3.3.1 Characterizing the effect of FIB irradiation in YIG

50 keV accelerated gallium ions (Ga^+) are used to irradiate YIG thin films at ion doses ranging from $1{\cdot}10^{12}$ to $1{\cdot}10^{15}$ ions/cm^2, with the purpose of manipulating the magnetic properties locally. As a dose calibration method, regions with linearly increasing ion doses are irradiated next to the excitation antenna and the SW wavelength change due to a modification of the effective magnetization M_{eff} is measured. Fig. 3.2 shows the resulting wavelength profiles vs. the applied ion dose. The degree of change in the magnetic properties is dependent on the applied Ga^+ ion dose and also on the acceleration voltage if the film thickness is larger than the ion penetration depth. The SRIM [79] simulated mean ion implantation depth of Ga^+ in a 100 nm thick YIG film is 24 nm and makes about a third of the total thickness (considering the effective thickness due to e. g. Ga diffusion into the first few (atomic) layers, sputter-process imposed film thickness variations, etc.). Nonetheless, we characterize how spin-wave propagation is affected in the effective layer and therefore the effect is modelled across the entire film thickness. Insights into FIB-irradiation-induced changes of YIG on the crystal level can be found in Sec. 2.3. As a main message, the reason we believe that the parameter changing the SW dispersion relation locally is M_{eff} is because we observed a change in the resonance field on fully irradiated films, which is solely dependent on M_{eff} and the applied frequency according to Kittel's equation. Furthermore, M_{eff} incorporates an anisotropy term that is likely to be affected by the FIB-induced strain in the crystal and potentially the underlying cause of the modification.

Interpreting the results in terms of micromagnetic parameters, we find that FIB irradiation of YIG can be accurately modeled in terms of modifying M_{eff} and the magnetic damping α ion-dose depen-

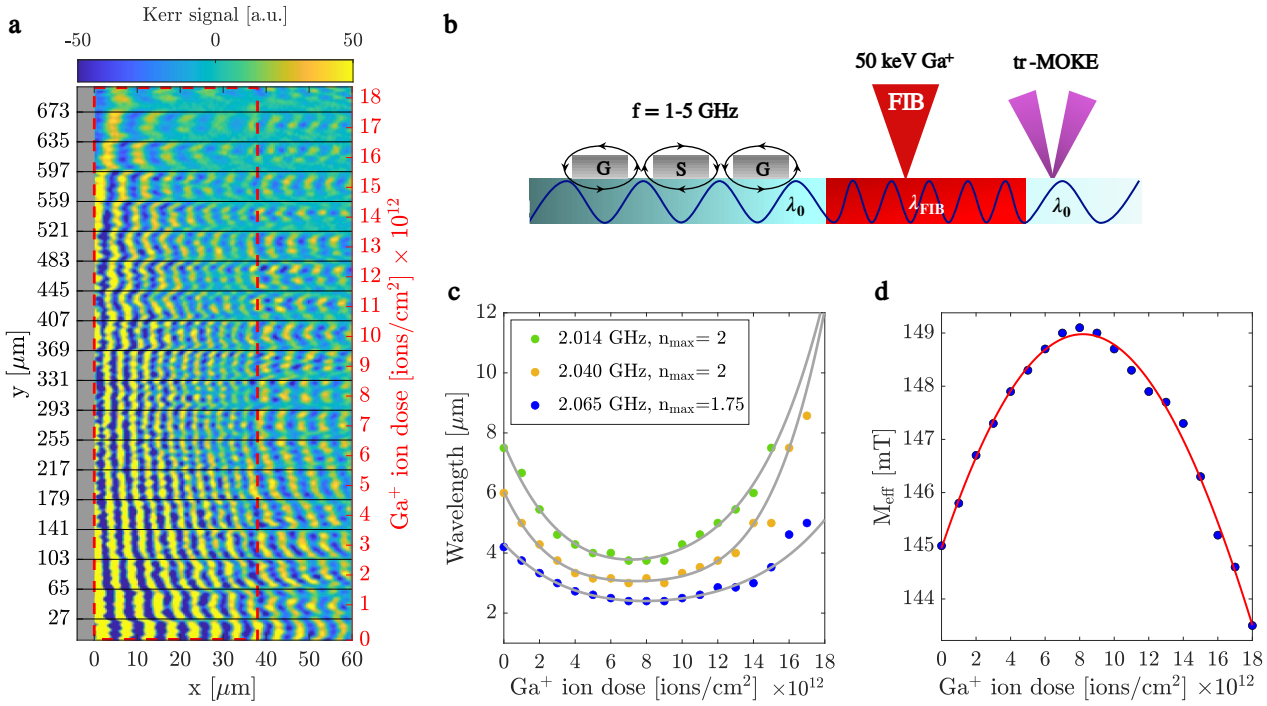

Figure 3.2 Illustration of the ion dose dependent change of $M_{\mathbf{eff}}$ in YIG. (a) trMOKE image of coherently excited spin waves (groundline of antenna shown on the left) in regions of linearly increasing ion doses (separated by horizontal lines, irradiated area indicated by red frame). The bottom row shows the actually excited wavelength in unirradiated YIG. (b) 1D sketch of the experiment: The area next to the excitation antenna is FIB irradiated, whereby the magnetization and hence the wavelength is locally changed. (c) Wavelength change vs. ion-dose profile at different frequency settings with an external field of 214 mT. (d) Ion-dose-dependent change of $M_{\mathbf{eff}}$, numerically calculated from the SW dispersion relation.

dent. A low ion dose (up to $6 \cdot 10^{12}$ ions/cm^2) increases $M_{\mathbf{eff}}$, and hence decreases the wavelength, while α increases only moderately (see Fig. 3.2.c - d). For higher ion doses, a turning point is reached and $M_{\mathbf{eff}}$ decreases again until spin-wave propagation is inhibited (doses larger than $1 \cdot 10^{14}$ ions/cm^3). There is multiple reasons we do not see spin waves at higher doses. First, as the wavelength goes up, the excitation efficiency of the coplanar waveguide diminishes. At even higher doses the cutoff frequency for spin waves (ferromagnetic resonance frequency) increases above the excitation frequency, thus spin waves are completely inhibited. Measuring these regions at higher frequencies is possible, and the damping is still not critically high. The wavelength vs. ion dose profile is non-linear and frequency-dependent due to the inherent non-linear dispersion relation of spin waves. In the low-dose regime, $M_{\mathbf{eff}}$ is slightly increased, which is used for the demonstration of optical elements with a distinct refractive index in analogy to glass.

Applications of higher complexity, such as continuous refractive media, can be modeled by saturation-magnetization landscapes. Using FIB, this means changing the ion dose point by point. Alternatively, it is also possible to change the filling factor in pixel space to set the value of $M_{\mathbf{eff}}$. This way, only a single ion dose has to be applied, and the average magnetization is changed due to a density gradient. We use a pixel size of 40 nm in the experiments (we can go as low as 10 nm), which is about two orders of magnitude smaller than the applied spin-wave wavelength. This technique (demonstrated in Sec. 3.4.2) is well suited for continuously changing wave propagation properties, as is done with graded-index (GRIN) optics [89].

A more trivial (but often-needed) use of FIB irradiation is to apply a high dose that entirely blocks propagation, or, in other words, destroys the magnetic properties ($M_{\mathbf{eff}} = 0$), and hence reflects SWs, such as shown in [2]. This allows the creation of refractive and diffractive optics using the same tools.

3.3.2 Tuning the magnonic index of refraction and saturation magnetization by FIB

In order to design spin-wave 'replicas' of optical devices, it is instructive to define the magnonic index of refraction n. The effective change of the magnonic refractive index $n_{\mathbf{eff}}$ is extracted from the wavelength change in the untreated vs. the irradiated YIG film part (λ_0 vs. $\lambda_{\mathbf{FIB}}$):

$$n_{\mathbf{eff}} = \lambda_{\mathbf{0}}/\lambda_{\mathbf{FIB}} \tag{3.1}$$

The highest achievable refractive index $n_{\mathbf{max}} = \lambda_0/\lambda_{\mathbf{min}}$ corresponds to the ion dose that generates the highest $M_{\mathbf{eff}}$, and hence the smallest possible wavelength $\lambda_{\mathbf{min}}$ with respect to the initial parameters. In order to model the correlation of FIB irradiation and the magnetic properties, the effect of FIB is best understood as an ion-dose dependent change of the effective magnetization $\Delta M_{\mathbf{eff}} = M_{\mathbf{eff,FIB}} - M_{\mathbf{eff,0}}$. The results are shown in Fig. 3.2.d (see previous section for details). Due to the highly nonlinear nature of the magnonic dispersion relation, $n_{\mathbf{eff}}$ is only valid for a certain spin-wave frequency f and the corresponding wavelength λ_0. We target wavelengths λ_0 that can be efficiently excited and detected by the coplanar waveguide antennas in use. Generally, the refractive index for a specific wavelength can be calculated by numerically solving the SW dispersion relation[28] for k-vectors at the initial $M_{\mathbf{eff,0}}$ and for $M_{\mathbf{eff,FIB}}$ at the respectively chosen ion dose:

$$n_{\mathbf{eff}} = k(M_{\mathbf{eff,FIB}}, f, H_{\mathbf{ext}}, t, A_{\mathbf{exch}})/k(M_{\mathbf{eff,0}}, f, H_{\mathbf{ext}}, t, A_{\mathbf{exch}}) \tag{3.2}$$

In Eq. 3.2, f is the microwave frequency used for excitation, $H_{\mathbf{ext}}$ the applied bias field normal to the film plane (forward volume), t is the film thickness, and $A_{\mathbf{exch}}$ is the exchange stiffness. This approach of defining a refractive index profile is similar to previous works, where a micromagnetic modelling of the dispersion relation is used for spin-wave lenses with a thickness or magnetization gradient [92], [93].

3.4 Results

3.4.1 Design and fabrication of optically inspired magnonic elements

To replicate the behavior of conventional optical elements (i. e. glass lens), one may utilize a single modified refractive index $n_{\mathbf{eff}}$ value in addition to that of intrinsic YIG (where $n_{\mathbf{eff}} = 1$). Fig. 3.3.a shows a trMOKE image of a plano-convex lens realized with this binary technique. The Lensmaker's

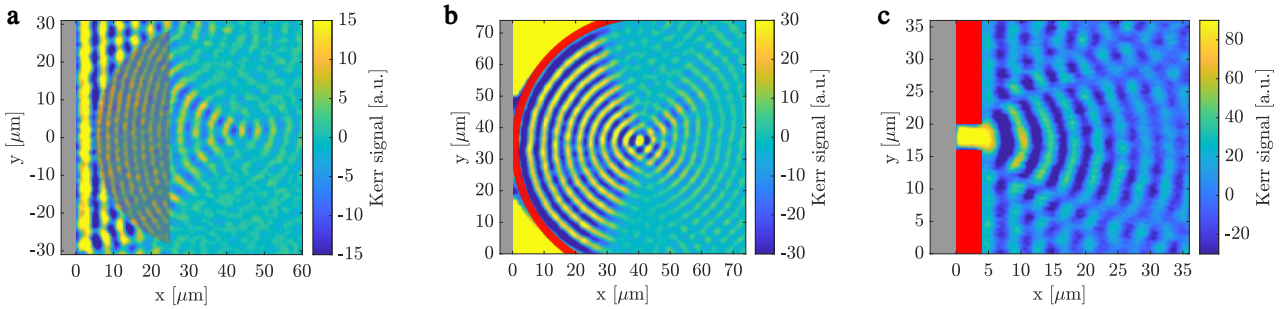

Figure 3.3 Demonstration of refractive, diffractive and reflective optical components fabricated with FIB irradiation, recorded with trMOKE. (a) D-shaped spherical lens with a curvature radius of 30 µm and a clearly shortened wavelength in the inside (semi-transparent red, n about 1.8). (b) A semicircular source (R=40 µm) with spin waves excited through the high-amplitude resonance behind the circle. The high-amplitude region appears as a saturated yellow region. Red lines indicate a high FIB dose that blocks spin wave propagation. (c) An 'optical' slit (4 µm width).

equation[94] is used for the given refractive index of 1.8 at a dose of $7{\cdot}10^{12}$ ions/cm^2. This is the maximum $n_{\mathbf{eff}}$ change achievable at this wavelength. The lens has a curvature radius of 30 µm and

thickness of 20 µm, resulting in a focal distance of about 37 µm. The trMOKE measured image of the lens reveals parameters closely matching the design target calculated from the optical formulas. The focal amplitude is weak compared to the excitation, probably because reflections occur on the surfaces of the lens and damping is slightly higher in this particular sample, but the focusing is clearly visible nonetheless. A different way of using the FIB irradiation is shown in Fig. 3.3.c, where we show single-slit spin-wave diffraction achieved by locally destroying the magnetization in the red areas through irradiation at a high ion dose of $1{\cdot}10^{15}$ ions/cm^2. The resulting diffraction pattern is a mixture of the expected diffraction pattern for a single slit, and a plane wave that couples through from behind the FIB irradiated part. To complete the parallels with elementary optical components, Fig. 3.3b demonstrates a circular-shaped source focusing spin waves at a distance that equals the radius. The curved surface acts as a secondary spin-wave source, where spin precession is driven by the high-amplitude, spatially-uniform oscillations of the area between its spherical backside and the excitation antenna. The primary non-linear precession excites linear spin waves on the inside of the circle via dipole coupling, a mechanism explored in [2].

Another useful focusing instrument in optics is the zone plate, where the focal distance is a function of lateral geometry, particularly the arrangement of the zones as opposed to thickness and curvature, as it is the case for conventional lenses. In the following, we use the properties of a Fresnel zone plate to demonstrate three different working mechanisms depending on distinct operation regimes of the FIB irradiation with respect to ion dose. In the first case, we use a low ion dose to create a phase shift, in the second case, a high-dose irradiation locally blocks SW propagation, and in the third case, SW transmission is completely inhibited with a high-dose region, and spin waves are excited indirectly on the patterned edge via dipole coupling.

A key function in optics is the ability to shift the phase of waves, and we show this feature by the example of a Fresnel phase plate in Fig. 3.4.a. The focusing effect occurs via constructive interference

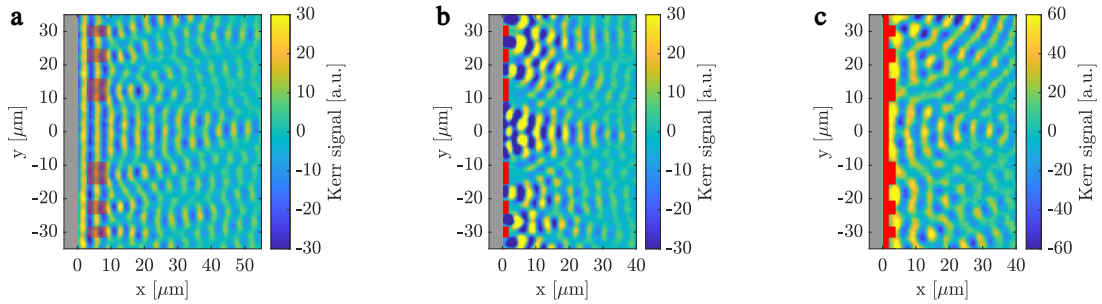

Figure 3.4 Spin-wave diffraction and focusing in FIB-treated regions (red areas) by reference to an optical (Fresnel) zone plate, visualized with trMOKE. Different ion doses are used for distinct operating mechanisms. (a) Phase-shift-induced focusing achieved with a low ion dose. The shortened wavelength in the FIB areas exits the zones with a phase shift close to 180 °. (b) A high ion dose that causes a local barrier for spin waves, analogously to an optically opaque region. (c) A blocking wall before the actual zone plate in combination with a high excitation amplitude excites spin waves via dipole-field coupling on the back surface. The low and high parts of the zone plate create an initial relative phase difference necessary for focusing.

of beams propagating with respect to a 180 ° phase difference to each other. This phase shift is achieved by the change of n over the 6 µm length of the zones (semi-transparent red overlays) so that the 180 ° phase difference occurs at the zone plate's exit plane from the difference of the wavelengths. Here, an ion dose of $7{\cdot}10^{12}$ ions/cm^2 was used, as it creates the largest difference in n, and the length was chosen with the help of a supplementary experiment (Fig. 2.9.b). Alternatively to this phase-shift-based zone plate, a Fresnel zone plate can be realized by simply blocking waves in the regions where they would destructively interfere at the desired focal point. In this device (Fig. 3.4.b) the phase shifters are replaced by regions fabricated with a large ion dose (red lines irradiated at a dose of $1{\cdot}10^{15}$ ions/cm^2). A third zone-plate demonstration uses the effect we also exploited in the circularly shaped source in Fig. 3.3.b, i. e. a coherent wavefront is created at the boundary of a high-dose region.

By shifting the wavefront about $\lambda/2$ between the zones, the desired focusing effect is achieved, as shown in Fig. 3.4.c. The geometrical arrangement of the zones is chosen to focus a 4 µm wavelength at a distance of 40 µm from the exit plane. Since the excited wavelength is different in (a), (b) and(c), the observed focal distance varies accordingly. Diffractive devices demonstrate the high resolution of FIB patterning and serve as proof that negligible damage is caused outside the irradiated area in the YIG films.

3.4.2 Gradient-index and Fourier optics for spin waves

In Fourier optics [45], [59], linear processing functions mostly rely on the Fourier-transform property of lenses – easily moving between the real and the Fourier domain enables a number of signal processing primitives. Similarly, Fourier-optics devices for spin waves could serve as building blocks for useful computing and information-processing functions.

Perhaps the most illustrative of Fourier optics devices is the 4f system illustrated in Fig. 3.5.a. The image (encoded in wave amplitude and phase on the image plane) is Fourier transformed by the first lens and this Fourier transform appears in the Fourier plane, which is inverse-Fourier transformed by the second lens. Any Fourier-domain manipulation of the image (such as filtering, convolution, matched filtering) can be accomplished by a filter placed in the Fourier plane that alters the magnitude and/or phase of the spectral components of the image.

While Fourier optics components could be put together from concave lenses such as the one shown in Fig. 3.3.a, the lens boundaries introduce undesired reflections and diffraction effects, which can largely be avoided in graded-index (GRIN) optics, where the wave steering is done with a gradually changing refractive index across the fiber diameter instead of introducing geometrical modifications with a singular index. Consequently, graded-index magnonic elements require the ability to realize gradually changing magnetic properties, such as simulated in[84]. Since FIB irradiation can continuously tune $n_{\mathbf{eff}}$ of a magnetic film by changing the filling factor of an image in pixel space, we can create a magnetization landscape of arbitrary shape, including a GRIN lens[62] or GRIN fibers[95]. Graphically, FIB-ing an image with every other pixel irradiated is the equivalent of half the ion dose, and the amplitude of a desired profile can be used to determine the filling ratio locally. Since the pixel size is much smaller than the SW wavelength, spin waves experience a smooth transition.

To produce a refractive-index gradient of a certain shape, the ion-dose profile needs to be determined for the desired wavelength (or index of refraction) profile. Here we used the measurements from Fig. 3.2.c. In case of a GRIN lens, the wavelength profile for a parabolic refractive-index change can be written as[96]

$$\lambda = \frac{\lambda_{\mathbf{FIB}}}{1 - 0.5(2\pi y/4f)^2}. \tag{3.3}$$

Hereby, $\lambda_{\mathbf{FIB}}$ is the resulting wavelength of the ion dose used for the design (ideally the smallest achievable wavelength), y is the lateral distance from the optical axis, and f is the desired focal length of the lens. For the calculation of the required ion-dose profile that results in the desired magnetization gradient, we used the ion dose vs. wavelength profile from Fig. 3.2.c and inserted the inverted version into the GRIN lens wavelength profile (Eq. 3.3), resulting in the ion-dose profile in Fig. 3.5.b. This profile is used for the density distribution of the FIB image in pixel space, and the 2D irradiation pattern of a 4f GRIN lens with a diameter of 18.5 µm and a length of 76 µm is shown in Fig. 3.5.c. Experimentally, this image is irradiated at a peak ion dose of $5.2{\cdot}10^{12}$ ions/cm^2, resulting in respectively lower doses across the diameter due to the density variation. Note that the image in Fig. 3.5.c is binary, i. e. only one global ion dose (red) is used for the irradiation. Hereby, $\lambda_{\mathbf{FIB}}$ is the resulting wavelength of the ion dose used for the design (ideally the smallest achievable wavelength), y is the lateral distance from the optical axis, and f is the desired focal length of the lens. For the calculation of the required ion-dose profile that results in the desired magnetization gradient, we used the ion dose vs. wavelength profile from Fig. 3.2.c and inserted the inverted version into the GRIN lens wavelength profile (Eq. 3.3), resulting in the ion-dose profile in Fig. 3.5.b. This profile is

used for the density distribution of the FIB image in pixel space, and the 2D irradiation pattern of a 4f GRIN lens with a diameter of 18.5 µm and a length of 76 µm is shown in Fig. 3.5.c. Experimentally, this image is irradiated at a peak ion dose of $5.2{\cdot}10^{12}$ ions/cm^2, resulting in respectively lower doses across the diameter due to the density variation. Note that the image in Fig. 3.5.c is binary, i. e. only one global ion dose (red) is used for the irradiation. The measured spin-wave profile of the fabricated GRIN lens – performing a Fourier transform of the plane wave excited by the microwave antenna right behind the lens – is shown in Fig. 3.5.d. (To avoid confusion, we note here that this is a full-pitch GRIN lens, thus the Fourier plane and the second image plane fall both inside the lens.) The focal distance is slightly longer than the design value (45 µm instead of 38 µm), which is most likely a result of a bias field inaccuracy or a deviation from the desired ion dose. At the exit plane, a reverse FT should occur, i. e. the plane wave is reconstructed. Due to the slightly longer focal length, the experimental lens is less than a full pitch, thus the waves at the exit are still slightly divergent.

To demonstrate FT properties of this GRIN lens, we irradiated a diffraction grating in front of the GRIN lens entrance plane by using a high dose, as shown in the slit experiment in Fig. 3.3.b. The

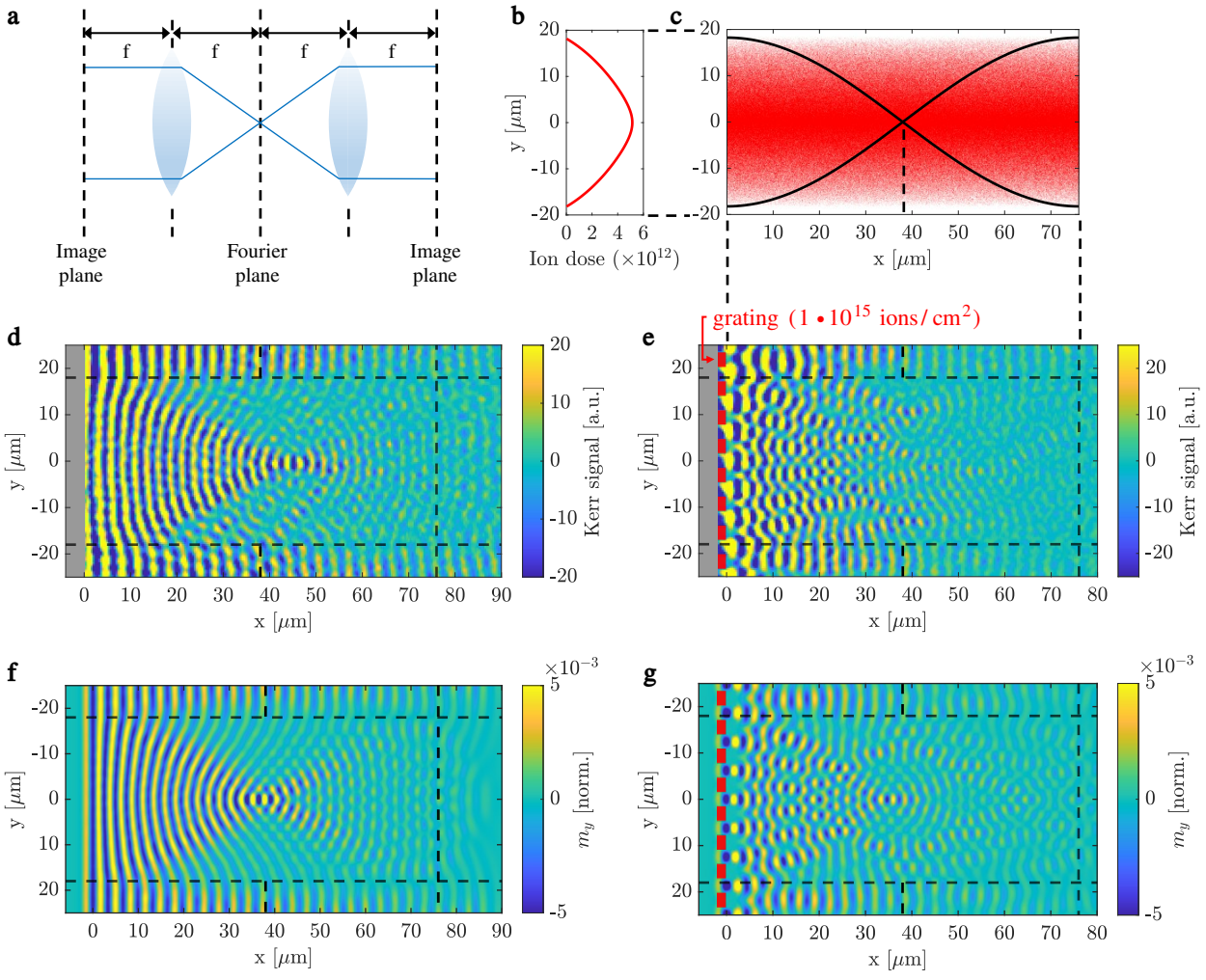

Figure 3.5 Demonstration of a 4**f** system for spin waves realized with a FIB-irradiated graded-index magnetization. (a) Working principle of a conventional **4f** system based on two consecutive lenses. (b) 1D ion-dose profile calculated from the measured wavelength change vs. ion dose profile. (c) 2D irradiation pattern (binary) of a full pitch GRIN lens realized by a filling-factor variation in the FIB image. (d) trMOKE image of the GRIN lens irradiated in YIG. (e) A diffraction grating is irradiated at the anterior plane. The system images the first order diffraction at 30 ° on the Fourier plane. (f) and (g) show the corresponding simulations for (d) and (e), performed with the calculated magnetization gradient and expected damping, respectively.

grating is designed to have a diffraction angle of 30 ° for $\lambda_0 = 3.1\,\mu m$ wavelength (grating constant $= 2\lambda_0 = 6.2\,\mu m$, thickness = 2 µm). The expected Fourier plane (FP) should occur at 38 µm, and we observe a slight deviation that has also occurred in the focal distance when we tested the GRIN lens with a plane wave. The occurring focal points left and right of the center peak in the FP represent the first-order diffraction of the grating, and correspond to the expected diffraction angle. The inverse Fourier transform (image of the grating) at the exit plane at 76 µm is, however, too weak to be visible in the measurement, potentially because of too high damping.

We performed micromagnetic simulations using mumax[3] to provide a reference for the ideal GRIN-lens operation. We used the same geometry as in the experiment, with the same excitation frequency applied. The saturation magnetization of the YIG film ($M_\mathbf{s} = 121\,kA/m$) was determined using ferromagnetic resonance (FMR) measurements. The external bias field ($B_\mathbf{ext} = 221.8\,mT$) was selected to match the experimental wavelength. In the irradiated regions, we used $M_s^{FIB} = 122.85\,kA/m$, also selected to produce the same wavelength as in the irradiated regions in the experiments. This corresponds to a 1.5 % change in saturation magnetization due to irradiation. We selected damping values to match the experimental decay, $\alpha = 6 \times 10^{-4}$ and $\alpha_\mathbf{FIB} = 12 \times 10^{-4}$, corresponding to a doubling in damping due to irradiation. Lateral discretization was set to 40 nm, with a single layer in the thickness direction (100 nm). The simulations closely match the experimental results, except for the focal length, which was equal to the design value in the simulations. The simulations show that the performance of our GRIN lens is mainly limited by two factors: (1) The relatively large damping in our films should be improved for a clear demonstration of recollimation/inverse Fourier transform. (2) Waves enter the GRIN lens from the sides due to diffraction, and these distort the interference patterns. For an improved demonstration, one should either limit the excitation of waves to the GRIN-lens input aperture, or block waves from entering through the sides. We suggest that this could be also realized using the proposed FIB technique.

3.5 Discussion

We can group the presented devices based on multiple properties: First, some part of the devices in this paper are refractive, i. e. ion irradiation is used for changing the effective refractive index in the specified region, while others are reflective or diffractive, i. e. relatively high doses are used to produce a perimeter around the device geometry. Here, the saturation magnetization in the YIG film changes abruptly – practically falling to zero. In the former case, spin waves propagate through the irradiated region (although with modified dispersion), while in the latter case spin waves are blocked, reflected, or generated on the boundaries between the intrinsic and irradiated YIG regions. This brings us to the next distinction based on whether the device is used for manipulating an incident wavefront or if it is used to indirectly excite a wavefront with a desired shape. From the perspective of functionality, we have demonstrated elements for focusing waves and also diffraction gratings (the zone plates being a combination of the two). The most sophisticated demonstration we present here is the GRIN lens and the 4f system based on it, which contains a pointwise varying refractive irradiation that is used for focusing waves, combined with a diffraction grating that block parts of the incident wavefront in a periodic manner, transmitting only a single spatial-frequency component. The above distinctions provide justification of the rich selection of demonstrations in this paper, representing the flexibility and wide applicability of a single fabrication technique to implement a wide range of optical elements. This set of devices can be considered complete in the sense that a full linear signal processor might be realized based on them, as demonstrated through the 4f system.

The refractive-index modification for spin waves in YIG through a FIB-induced magnetization change can be accurately calculated from the ion-dose-dependent wavelength change. With this, we are able to design devices not only where binary refractive arrangements are needed, but also create smooth magnetization transitions (gradients) that are essential in GRIN optics. With the strategy to use a halftoning technique (stochastical filling factor in pixel space) on the FIB image to produce an ion-dose gradient, one global ion dose can be used for the entire image, eliminating the need for

multiple irradiation steps. Since the spotsize of the FIB is two orders of magnitude smaller than the spin-wave wavelength, this simplification is not expected to degrade the device performance.

As the complexity of the 4f system is the highest among the presented devices, the limitations of the technology (spin waves and also our facilities) is the most evident here. It is visible in Fig. 3.5.d, e that damping limits the useful length of the GRIN lens to tens of wavelengths. We presume that our demonstration is not optimal from this perspective in multiple ways: with better-quality (homogeneity and damping) YIG films, and by optimization of parameters to achieve higher group velocity, we expect that it is possible to increase the propagation distance and thus the practical device size by at least an order of magnitude. There is also a limitation of the numerical aperture in the 4**f** system, which is posed by the limited variability of the effective saturation magnetization (and therefore the maximum achievable refractive index) induced by irradiation. Although we demonstrated that a refractive index comparable to optics is achievable ($n \approx 1.8$), a higher change would improve the applicability and performance of magnonic devices. We see a potential improvement here, as we estimate that less than a third of the YIG film is affected by the FIB due to the shallow penetration depth. By using lighter ions, e. g. He^+, we expect that a stronger effect is achievable. Finally, a strong disturbance of the interference pattern is caused by the waves that are generated adjacent to the fabricated devices. This could be avoided by separating the device laterally from the neighboring structures, for which FIB irradiation could also be used, both for creating reflective and absorbing boundary conditions, exploiting the steeply increasing damping at moderately high doses.

Magnonic systems themselves have limitations, perhaps the most important one is the finite damping that limits the realizable device size and complexity. Thus, spin waves are not an ideal fit to directly replicate classical optical building blocks, instead, they are more suitable for the approaches used in nanophotonics [66], [68] – we believe that our technique is also applicable to the realization of such structures, as the achievable resolution with FIB (≈10 nm) can easily serve that. The automatic design of magnonic devices combined with a flexible and versatile fabrication method has the potential to raise the bar for magnonic device concepts, enabling the realization of circuits [97], and drive the field towards practical applications.

In terms of applications, the 4f system (and similar constructions) carries the biggest potential. Based on the 4f system it is possible to realize a wide class of linear (Fourier domain) signal processing applications as it was well established in the field of optical computing [59]. Thus, successful implementation of 4f systems with spin waves may allow any linear signal-processing task to be implemented in the magnonic domain. Such tasks are essential building blocks of neuromorphic computing pipelines and are in great demand for edge AI tasks [98].

3.6 Conclusion

Our paper presents FIB irradiation of YIG as a straightforward technology to manipulate the index of refraction precisely and in a quasi-continuous way, enabling chip-scale magnonic clones of optical components. We demonstrated various use cases how elements known from optics can be adapted in the spin-wave domain by using FIB. The FIB direct-writing technology offers flexible, rapid, high-resolution prototyping, while it avoids many challenges of traditional patterning methods, such as the inability to produce gradients and inevitably introducing defects on patterned edges. Although FIB itself is not directly applicable for mass production, the presented devices could be straightforwardly mass-produced using the implanter technology omnipresent in industrial settings.

Due to its flexibility, high resolution, wide availability and a path toward mass production, we believe that the presented technology has the potential to drive a magnonic revolution and turn spin-wave-based, chip-scale computing devices to a practical reality.

Acknowledgements

The authors want to thank all staff members and researchers working in the lab facilities of ZEIT^{lab}, and Tatyana Orlova and Maksym Zhukovski at the Imaging Facility at University of Notre Dame. We would also like to thank the motivated students involved in this project, especially Carolin Calcagno. Funding from the German Research Foundation (DFG No. 429656450), the German Academic Exchange Service (DAAD, No. 57562081) and the Bavaria California Technology Center (BaCaTeC) is acknowledged. A.P. received funding from the PPD research program of the Hungarian Academy of Sciences. G.C. acknowledges financial support from the Horizon 2020 Framework Program of the European Commission under FET-Open grant agreement no. 899646 (k-NET).

3.7 Personal contribution

This work was originally published as M. Kiechle, A. Papp, S. Mendisch, *et al.*, "Spin-wave optics in yig realized by ion-beam irradiation", *Small*, p. 2 207 293, 2023. DOI: 10.1002/smll.202207293 and presents the fundamental discoveries of my doctoral research in the Nanomagnetic devices group of Dr. Becherer at the Technical University of Munich. In the following, I will list my contributions to this work sequentially in line with to the experimental procedures.

YIG thin film fabrication

The magnetic substrate used for the experiments is a 100 nm thin Yttrium Iron Garnet film on a GGG substrate, the most commonly used carrier material for spin waves because of its record low damping. The availability of those films is sparse, the fabrication process for high-quality films is delicate and costly. In the beginning of my PhD program, we decided to establish our own fabrication process via RF-magnetron sputter deposition, and after 6 months of experimenting with the process parameters, I was able to offer a film quality comparable to those of my peers[72], giving us room for plenty of experiments.

Coplanar microwave antennas

As a next step, I developed a fabrication process for coplanar microwave antennas on top of YIG that are used for the excitation of spin waves. I performed basic microwave simulations to use an appropriate geometry, and designed a contact-mask layout for the lithography. The aluminum deposition was done via E-beam evaporation, and subsequently etched selectively with a TMAH-based developer. This process has always been the bottleneck of fabrication, but has been used for most experiments shown in this work. It was later done by Matthias Golibrzuch, who had a much more efficient tool (maskless aligner) at hand, which made life so much easier (I regret we did not talk sooner).

Time-resolved MOKE measurements

The trMOKE apparatus was developed and put together by my colleague Ádám Papp during his one-year postdoc time in our group, and he has taught me everything about this valuable microscopy technique. After he left, I was able to improve some features, especially the critical bias field alignment that is intended to be perfectly perpendicular to the sample surface. Most of the spin-wave measurements shown in this work have been recorded by myself, I post-processed the data and extensively discussed the results with Ádám, leading to many experimental iterations.

Direct focused-ion-beam irradiation of YIG

The centerpiece of this work, direct FIB irradiation of insulating YIG thin film, was thoroughly developed and conducted by myself. This starts with a pre-characterization of the respective sample, whereby an ion-dose map is irradiated along the antennas to measure the dose-dependent impact on magnetic properties by the spin-wave wavelength change visualized via trMOKE microscopy. This ion-dose map is then used for the optical designs whereby the magnetic properties can be used to model a magnonic refractive index.

Design of optically inspired spin-wave components

The optical counterparts for spin waves shown in this work were mostly designed by myself, especially the 4f processor, certainly with the help of Ádám Papp who also provided many inspirations with this previous work[57]. I created the binary images for the irradiation script-based in Matlab, and in case of the 4f processor converted the ion-dose profile to the refractive index profile of a GRIN lens.

4 Publication #2: A concave grating for spin waves in the Rowland arrangement

This chapter is a full reprint of the published article
Á. Papp, M. Kiechle, S. Mendisch, *et al.*, "Experimental demonstration of a concave grating for spin waves in the rowland arrangement", *Scientific Reports*, vol. 11, no. 1, pp. 1–8, 2021. DOI: 10.1038/s41598-021-93700-z.

4.1 Abstract

We experimentally demonstrate the operation of a Rowland-type concave grating for spin waves, with potential application as a microwave spectrometer. In this device geometry, spin waves are coherently excited on a diffraction grating and form an interference pattern that focuses spin waves to a point corresponding to their frequency. The diffraction grating was created by focused-ion-beam irradiation, which was found to locally eliminate the ferrimagnetic properties of YIG, without removing the material. We found that in our experiments spin waves were created by an indirect excitation mechanism, by exploiting nonlinear resonance between the grating and the coplanar waveguide. Although our demonstration does not include the separation of multiple frequency components, since this is not possible if the nonlinear excitation mechanism is used, we believe that using linear excitation the same device geometry could be used as a spectrometer. Our work paves the way for complex spin-wave optic devices – chips that replicate the functionality of integrated optical devices on a chip scale.

4.2 Introduction

Information processing in today's computers is done almost exclusively by charges (electric currents). Photons, albeit they are ideal for information transmission, never became a mainstream technology for computing. Despite their numerous advantages, photonic devices have practical limitations: they are challenging to integrate on-chip and optical wavelengths (about a micrometer) are huge compared to nanoscale devices, limiting the scalability of any photonic interference-based device.

Spin waves are wave-like excitations in magnetic materials that travel via coupling between precessing magnetic moments. In our current investigation, we consider spin waves in ferro-, and ferrimagnets, but we note that spin waves are shown to exist in antiferromagnets and paramagnets as well [99]. Their wavelength can be adjusted in a wide range (from several micrometers down to potentially nanometer scale), and they have an electronics-friendly frequency range (1-100 GHz) [47]. This makes spin waves attractive for on-chip applications, especially in wave-based microwave signal processing. They also interact with each other (scatter), and the resulting nonlinearity may enable general-purpose computation. Unlike electromagnetic waves that can propagate in vacuum, spin waves exist only in (magnetic) medium and one needs high-quality materials to achieve ideal conditions for propagation and also carefully designed waveguide structures to launch (and pick up) the waves. It has only recently become possible to demonstrate short-wavelength, long-distance propagation [100], [101], spin-wave equivalents of optical laws [102] or larger-scale refractive devices using local heating [62]. Spin-wave variants of complex optical devices have been shown recently by experimental demonstrations [88], [103] – including an anisotropic spectrometer design [104].

A key element of such a spin-wave optics device is a source that launches coherent spin waves. In the simplest case, the source of spin waves can be a simple coplanar waveguide that is placed atop the magnetic film. For many device constructions, such a simple construction is insufficient. Microwave waveguides alone are fairly inefficient at short spin-wave wavelengths [105] and they are limited to the generation of plane wavefronts or curved wavefronts with relatively small curvature. For the generation of short-wavelength spin waves or non-planar wavefronts, lithographically patterning the edge of the magnetic film is desirable. A periodically patterned edge can serve both as a wave source and a diffracting element.

For sake of completeness, we note that there is a number of emerging physical phenomena that one, in principle may use as sources of spin waves, such as spin-transfer and spin-orbit torques [106], [107] or optical methods. Still, waveguide-based (Oersted-field-based) generation of spin waves is perhaps the most straightforward method to use in microwave devices.

The focus of the present paper is the experimental study of such a patterned edge as a spin-wave launcher. We use Focused Ion Beam (FIB) irradiation to write a high-resolution concave grating pattern in a yttrium iron garnet (YIG) thin film. The grating is used in the Rowland spectrometer arrangement, which is frequently used in optical and X-ray spectroscopy [108]. This arrangement does not require a separate lens component, and thus it is ideal for waves with limited propagation length. We experimentally demonstrate that the edge of a FIB-irradiated pattern in YIG generates a coherent spin-wave wavefront. Using time-resolved Magneto-optical Kerr Effect (trMOKE) imaging we found that the diffraction patterns closely match those expected from theory and micromagnetic simulations. An unexpected discovery was that in our experiments spin waves were not primarily excited directly by the field of the waveguide. Instead, spin waves were generated indirectly by the dipole fields of high-amplitude, nonlinear, and long-wavelength standing waves that developed behind the grating in the unirradiated area. This process has a significantly higher efficiency of spin-wave generation at a distance from the waveguide. However, this quasi-homogeneous oscillation behind the grating only forms at a sufficiently high amplitude and only if a single frequency component is applied.

4.3 Spectral Decomposition with a Concave Diffraction Grating

The main component of the proposed device is a concave diffraction grating that acts both as a wave source and as a diffractor. The fabrication of such a grating requires sub-wavelength patterning resolution as the pitch of the grating has to be comparable to the spin-wave wavelength. We use the so-called Rowland arrangement, a detailed description is given in [85]. The device generates a spectral decomposition of a time-domain signal by converting temporal frequency components to spatially separated spin-wave intensity peaks. The layout of the fabricated device is shown in Fig. 4.1. The microwave signal is converted to spin waves by a waveguide antenna. Each frequency component of the signal generates spin waves with corresponding wavelengths. Along the edge of the grating (FIB-irradiated region), the time-varying magnetic field is almost homogeneous, but due to the abrupt parameter change in YIG, every point along the edge acts as a wave source (also described in [109]). The curved grating not only diffracts different wavelengths in different directions but also focuses the wavefronts. The drawing of Fig. 4.1**b** shows the geometry to determine the diffraction pattern. With a concave grating of radius R and ridge pitch d, the diffraction peaks (i.e. wavelength-dependent focal points) will form on a circle with radius $R/2$ drawn tangentially to the grating (Rowland circle). The n^{th}-order diffraction angle can be calculated as $\alpha = \arcsin\left(\frac{n\lambda}{d}\right)$, where λ is the wavelength of the spin wave. In traditional optical or X-ray Rowland spectrometers the wave source is placed opposing the curved grating, which reflects the waves, acting as a secondary source. Such arrangement would be rather impractical for spin waves: the relatively long path between the source and the diffraction grating will cause much higher attenuation of spin waves. Thus, it is desirable that the grating and the source are in the same structure, i.e. the coherent spin-wave source itself is shaped as a curved diffraction grating. In this geometry, diffraction is caused by the phase difference between waves that originate from the bottom and the top of the ridges. This phase difference will also depend on the

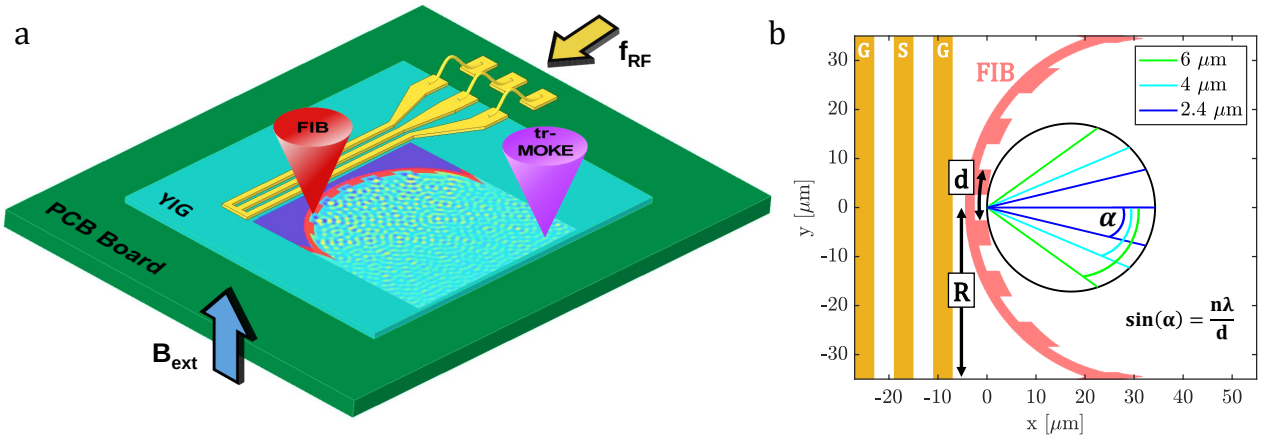

Figure 4.1 **a**) Sketch of the experimental setup, indicating the coplanar waveguide, the FIB irradiated grating, the trMOKE probing laser, and the spin-wave interference pattern. **b**) Geometry of the curved diffraction grating in the Rowland arrangement. The angle under which the first-order diffraction peak is seen from the center of the grating is denoted by α.

ratio of the ridge depth and the wavelength, which does not influence the diffraction angle, but it changes the relative amplitude between diffraction orders. In the designed structure the ridge depth also introduces an amplitude difference between waves that are generated on the top and the bottom of the ridge. The device is thus a combination of an amplitude grating and a phase grating.

We fabricated the designed device and recorded spin-wave interference patterns with trMOKE. The trMOKE images at three different excitation frequencies are shown in Fig. 4.2. Diffraction peaks are clearly observed close to the expected diffraction angles, as indicated by black lines. In case of the smallest wavelength the second-order peaks can also be observed ($\frac{2\lambda}{d} < 1$). We found that the peaks are not perfectly focused along the Rowland circle, but an arc can be fitted to the peaks that works well for all three wavelengths. We attribute this to the fact that our grating is much wider than conventional concave gratings (180° instead of a few degrees), and thus the approximations used in the derivation of the Rowland circle do not hold perfectly. This is confirmed by micromagnetic simulations, which also show that focal points are located on an arc with a slightly smaller curvature (see Fig. 4.4**c**). Another possible cause of deviations is the slight anisotropy of spin waves introduced by a tilt in the external bias field, which can not be fully eliminated in our current experimental setup.

We also note that side lobes (smaller peaks next to the labeled peaks) in Fig. 4.2 are due to the Airy pattern formation around the focal point (seen as circular pattern in the 2D scan). Since the size of the presented device is only an order of magnitude larger than the wavelength, these side lobes are filling a large portion of the output space, but with scaling up the device size compared to the wavelength this portion would decrease. Asymmetry of these peaks (e.g. in Fig. 4.2**d**) is probably due to fabrication defects.

4.4 Generation Mechanism of Spin Waves by Nonlinear Resonance

In most spin-wave devices, the magnetic field of the waveguide is directly responsible for launching the spin waves, as described in [85]. The relatively delocalized magnetic field of the waveguide and the localized demagnetizing field of the film edge jointly create a high, periodically changing torque and launch the spin waves [109].

We found that in our device an indirect, nonlinear mechanism is dominant for spin-wave excitation. In the design presented in [85] all material in the YIG film is assumed to be removed behind the grating. However, our FIB method is performed as the final fabrication step, after the CPW is already in place. We did not irradiate the total area between the grating and the CPW, only a narrow region, which is wide enough to block spin waves at the designed wavelength to significantly couple through

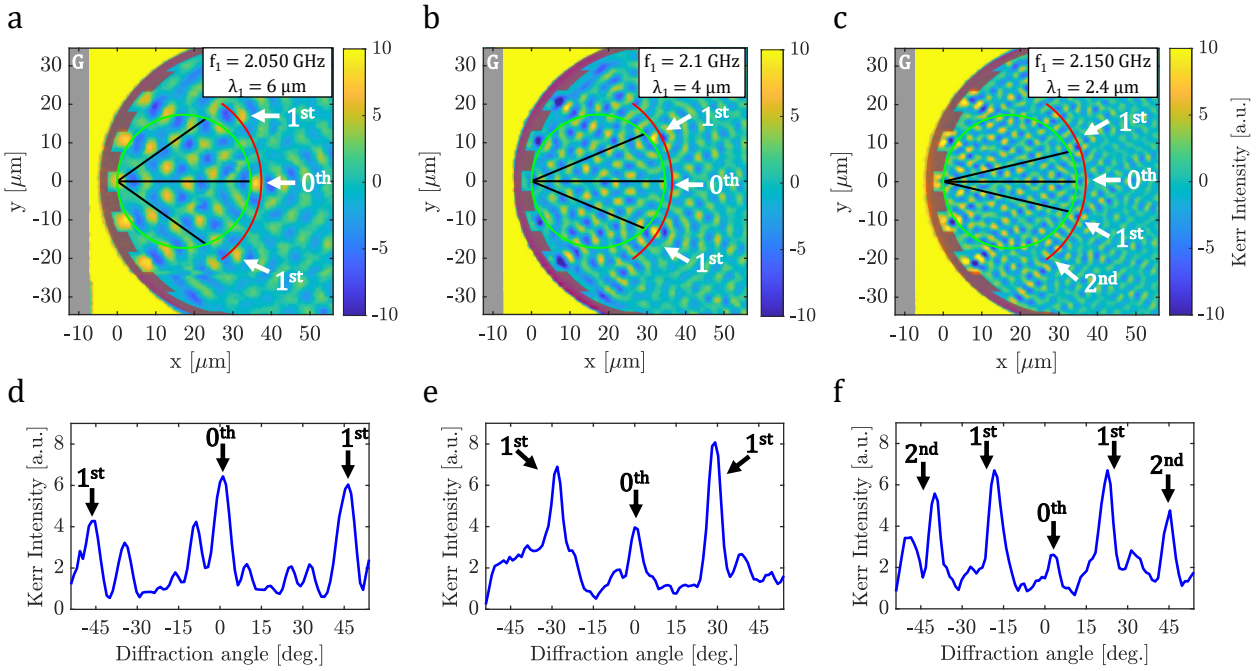

Figure 4.2 Spin-wave interference patterns recorded by trMOKE at three different excitation frequencies at constant bias field. In **a-c**) the FIB irradiated region (grating) is indicated by a semi-transparent red overlay (radius R=30 μm, pitch d=12 μm), the gray stripe represents the ground line of the CPW. The green circles are the theoretical Rowland circles with a radius R/2, while the radius of red arcs are fitted to the data. Black lines indicate expected diffraction angles, and white arrows point to focal points in the measured data. The microwave power is kept at 5 dBm. **d-f**) Spin-wave intensities extracted along the red arcs in **a-c**).

via dipole fields. However, at sufficiently large excitation amplitudes the static (OOP) component of the magnetization decreases, which in turn decreases the demagnetization field of the YIG film [110]. This results in a higher effective field, and with that the spin-wave wavelength increases. The wavelength at sufficiently large amplitudes becomes much larger than the distance between the CPW and the grating and the spin waves that are generated under the CPW reflect back from the back side of the grating, creating a standing-wave pattern. Since the wavelength is much larger than the size of the region between the CPW and the grating, this resembles a homogeneous resonance in that region. This large area has a considerable oscillating dipole field that acts on the edge of the grating, launching secondary spin waves that form the Rowland interference pattern. We note that this mechanism does not change the frequency of the generated waves, only their wavelength in the strongly excited area behind the grating. One could refer to this effect as an amplitude-dependent 'refractive index' in this region. Waves that are indirectly excited on the edge of the concave grating have the same frequency and wavelength as if they were generated by direct linear coupling from the waveguide. The trMOKE images of Fig. 4.2**a-c** already show the high-amplitude region on the left of the grating: it is observable that in this region the colormap is saturated and without apparent pattern, indicating large-amplitude, uniform precession. The applied microwave power was set to 5 dBm at the RF source, however the actual spin-wave amplitude depends on the frequency due to mismatches in the RF signal path and physical shape of the magnetic field of the CPW.

The dipole field of the quasi-homogeneous resonant excitation reaches significantly farther than that of the short-wavelength spin waves, thus it can excite coherent spin waves on the ridges of the grating. This field is in fact much stronger at this distance than the magnetic field of the CPW, becoming the dominant effect for spin-wave generation on the grating edge.

Figure 4.3 shows the spin-wave-generation process in more detail. At sufficiently small excitation power ($P_{\mathrm{rf}} = 0\,\mathrm{dBm}$), linear spin waves are excited under the CPW. These small-amplitude, short-

wavelength spin waves cannot significantly couple through the FIB-irradiated region. However, the Oersted field of the CPW is not sufficient to create spin waves at the grating edge, that could be detected by our trMOKE apparatus. In Fig. 4.3**b** (P_{rf} = 5 dBm) nonlinear behavior is observable behind the grating, but the nonlinear wavelength is not yet long enough to create uniform precession. One can observe a partial interference pattern on the right possibly due to larger uniform standing waves on the top. At P_{rf} = 10 dBm excitation power (Fig. 4.3**c**) the resonance almost uniform (apart from the top region being out-of phase), and the interference pattern is complete. Here we note that although in Fig. 4.3**c** we used higher excitation power (10 dBm) than in Fig. 4.2 (5 dBm), we do not see fully homogeneous resonance behind the grating in the former case. This is mainly because in Fig. 4.3 we used a grating that is twice the size of the grating in Fig. 4.2, thus the distance and the area behind the grating is larger, requiring higher amplitude to fill. Also, the proportion power that reaches the antenna varies greatly from sample to sample, as fabrication variations and experimental conditions change transmission characteristics of the microwave path line. Thus, direct comparison of amplitude levels is not possible between different experiments.

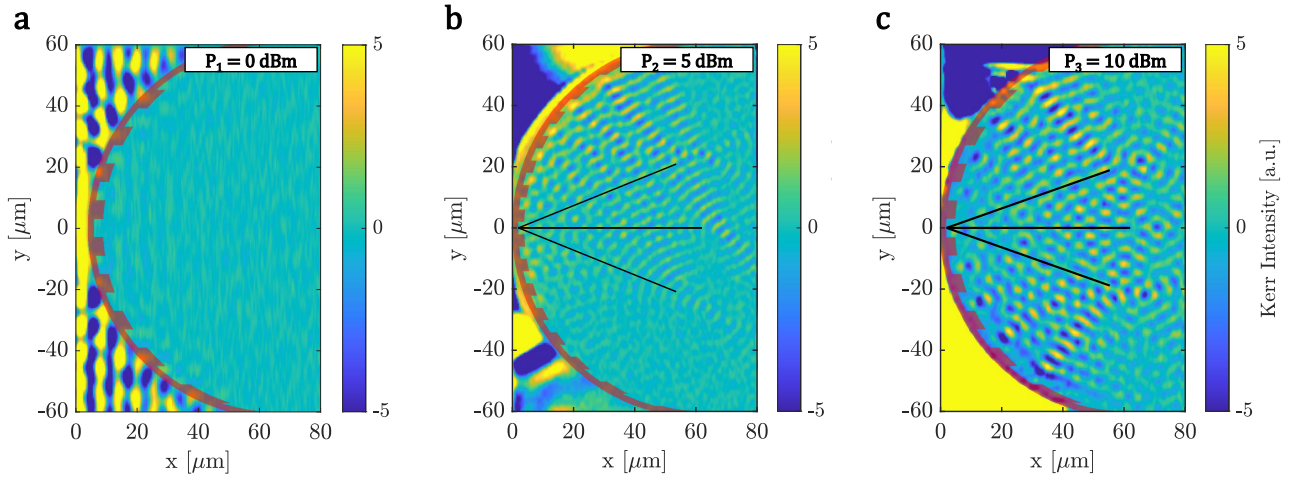

Figure 4.3 TrMOKE images of miscellaneous gratings expressing the difference in performance with respect to small **a)**, higher **b)** and high **c)** microwave current applied at the input waveguide. The right edge of the CPW ground line is 3 μm away from grating posterior in each case. The semi-transparent red overlay indicates the FIB-irradiated region, black lines show expected diffraction angles. The grating operation visibly enhances with the level of uniformity in the nonlinear spin wave excitation behind the FIB area.

To gain more insight into the excitation process, we performed both one-dimensional and two-dimensional micromagnetic simulations using mumax3 [111]. These simulations confirmed the behavior that we observed in the experiments (Fig. 4.4). At small excitation fields, spin waves beyond the grating are very small in amplitude (Fig. 4.4**a**). At a higher (nonlinear) excitation field, however, a uniform standing wave is observed between the grating and the CPW, and coupling through the FIB region is strong (Fig. 4.4**b**). Left from the CPW the wavelength change of the spin waves can be observed as they decay due to magnetic damping. Beyond about 50 µm propagation self-modulational instability is also causing spikes in the waveform [112]. 2D simulations also confirmed the operation of the device (Fig. 4.4**c**). Here the diffraction angles match perfectly the theory, but the position of the focal points are also somewhat behind the Rowland circle. This is the same effect we observe in the experiments. Gratings with larger radius and shorter width would probably not suffer from this deviation, especially at small diffraction angles. However, the position of the peaks is predictable, so this does not affect the usability of the device.

An additional, very unusual aspect of this nonlinear excitation can be observed in Fig. 4.2**c**. In case of the direct excitation mechanism one would expect that segments of the grating that are closest to the CPW will excite the highest amplitude waves, since the field of the CPW decays with the lateral distance. However, here we observe exactly the opposite: the strongest "beams" seem to form on the farthest parts of the grating, and amplitudes are less strong in the middle part, which is very close to

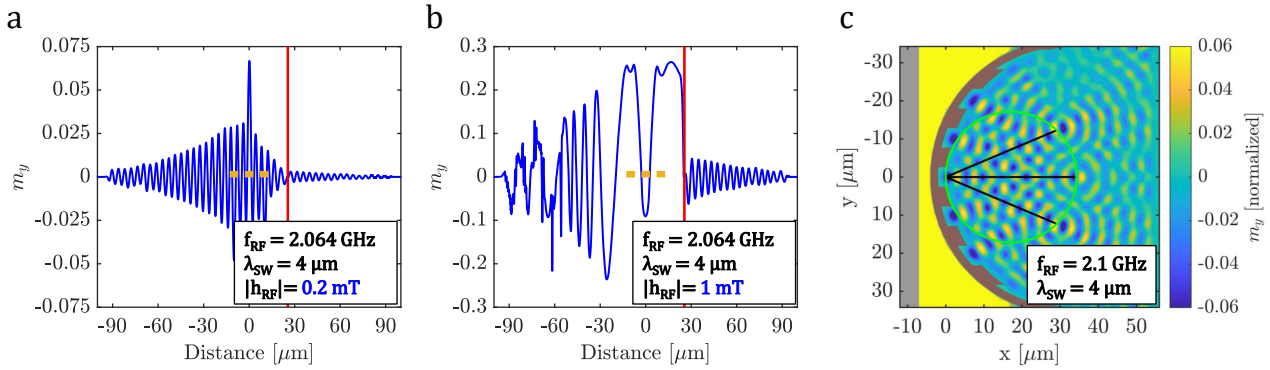

Figure 4.4 Micromagnetic simulations of nonlinear indirect excitation of spin waves. Yellow rectangles indicate the CPW position and width. The red stripe represents the FIB irradiated region, modelled by zero M_s. **a)** is a 1D example of linear excitation, while **b** is a strongly nonlinear case. **c)** represents a 2D simulation of the experimental scenario in Fig. 4.2**b**.

the CPW (Fig. 4.3**c**). This is because the largest area where homogeneous oscillations can occur are on the sides, where there is enough distance between the CPW and the grating. The larger the area, the higher are the dipole fields, and the higher the excitation on the opposite side of the grating. Thus, the discovered indirect excitation mechanism is in comparison very efficient at exciting short-wavelength spin waves on a finely patterned edge at a distance from a straight (or slightly curved) waveguide. This can be advantageous in applications where a complex wavefront has to be launched.

A significant limitation of the nonlinear excitation method is that it only works for single-frequency excitations. If multiple frequency components are excited, the uniform standing waves cannot form, moreover nonlinear mixing creates unwanted spectral pollution. If multiple frequencies are present in the excitation signal (as it is often desirable in a spectrum analyzer), the nonlinear method cannot be used, but, as we demonstrated, the proposed method is very effective at creating devices with complex interference patterns at a single frequency.

4.5 Methods

4.5.1 Sample Fabrication and Characterization

YIG thin films were deposited on a GGG substrate using rf-magnetron sputtering (we used 100 nm thick films in the grating experiments). Their magnetic properties were evaluated by means of ferromagnetic resonance (FMR), revealing a saturation magnetization of M_s=120 kA/m and a damping constant of $\alpha_{YIG} = 4.4 \times 10^{-4}$. For the excitation of spin waves shorted aluminum CPW antennas were fabricated on top of the YIG film. The antennas were wire bonded to a PCB based CPW with connections to an RF signal generator (Stanford Research SG 386).

The gratings were fabricated in YIG next to the CPW via FIB irradiation. We used 50 keV Ga^+ ions with a relatively low dose (10^{15} ions/cm^2), which is high enough to almost completely destroy the magnetic properties of YIG, but no material is removed. Much higher doses (in case of ion milling) would likely deteriorate the YIG film around the patterned region due to ion scattering, which makes this method more suitable. Sub-micron resolution patterning can easily be achieved (possibly down to 100 nm in our facility). A similar method was recently described in [16], where comparably lower doses were used to change magnetic properties of YIG on film level. Here, we deliberately used higher doses to drastically reduce the saturation magnetization of YIG locally, to create a region which inhibits spin-wave transmission. We found that this method is in effect very similar to actually removing material, as it was proposed in [85].

The effect of FIB irradiation was also investigated using transmission electron microscopy (TEM). In Fig. 4.5**b**,**c** TEM images indicate that the crystalline structure of YIG is completely destroyed down to

a depth of approximately 25 nm, and further significant damage is observable at even higher depths. These results are in good agreement with the previously performed SRIM simulations of our system in Fig. 4.5**a**, suggesting a peak implantation depth of 24 nm.

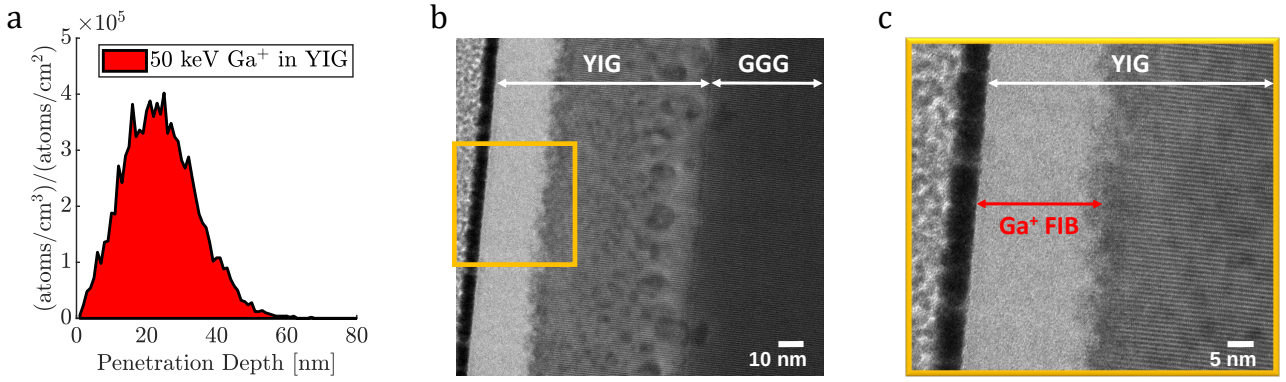

Figure 4.5 Crystal investigation of the FIB impact in YIG by means of TEM. **a)** Shows the simulated ion implantation depth for 50 keV Ga^+ ions in $Y_3Fe_5O_{12}$. A cross-sectional image of a 80 nm thick irradiated YIG film is depicted in **b)**. **c)** The magnification of the orange square in **b)** exposes an amorphous toplayer of the thickness expected from the SRIM simulations in **a)**.

Ga^+ ions are relatively large compared to other frequently used ions such as He^+, which explains their low penetration depth and the resulting bilayer formation in YIG. We only had access to Ga^+ FIB, but SRIM simulations suggest that higher implantation depths could be achieved with He^+ ions, and, with higher doses compared to Ga^+, similar modification of YIG properties could be achieved with better uniformity across the film thickness.

4.5.2 Imaging of 2D Spin-Wave Patterns

To image spin-wave interference patterns we built a time-resolved magneto-optical Kerr microscope (trMOKE). Since the Rowland spectrometer requires isotropic spin-wave propagation (as in optics), we had to use out-of-plane bias. In principle slightly anisotropic waves could also be used, as investigated e.g. in [63], but this requires a redesign of the Rowland grating shape. With the requirement of an out-of-plane bias, we designed our trMOKE to measure the longitudinal Kerr effect, i.e. it is sensitive to changes in the in-plane magnetization component that lies in the incidence plane of the laser [113]. We used a ps-laser with 50 ps pulse width and 405 nm wavelength (PicoQuant Taiko PDL M1 with LDH-IB-405 laser head). With this, we can measure spin waves up to approximately 5 GHz frequency (with 10 MHz steps) and down to 2 µm wavelength. We scan through the sample with an XYZ stage with 0.4 µm resolution. Larger area scans (such as the ones presented in this paper) take about a few hours of measurement time. We use a stroboscopic technique in which the excitation signal is phase locked to the lock-in amplifier and the ps-laser, thus we can extract phase information as well. The amplitude scale is not calibrated, but we estimate that the setup is sensitive to a few percent change in in-plane magnetization.

Currently our setup uses a permanent magnet under the sample for biasing. This makes calibration challenging due to the inhomogeneous field profile. The bias field values in the measurements are approximate values with a few mT uncertainty, and perfect out-of-plane biasing is difficult to achieve.

The spin-wave amplitude and phase were recorded using the following measurement parameters: scanning time step 500 ms, at a sampling rate of 26.16 Samples/s, the step size in x and y direction was 0.8 µm (2 microsteps of the stage). To correct for potential errors in the step size, the recorded data had to be stretched/compressed slightly to fit the applied FIB masks (red overlay) on the grating in the recorded data. The deviation is still small, after fitting a step size of 0.38 µm was used in the X direction instead of the assumed 0.4 µm. This fitting is required due to a possible step-size difference in the X and Y axis of either the trMOKE or the FIB stage. Furthermore, a slight rotation

of the recorded pattern was also required due to alignment errors when mounting the sample in the microscope. No image enhancement techniques were applied on the raw data.

4.5.3 Micromagnetic simulations

Micromagnetic simulations were performed in mumax3[111]. We used experimental values for parameters where they were available (M_s=120 kA/m and $\alpha_{YIG} = 4.4 \times 10^{-4}$, 100 nm thickness), and values from literature where we could not directly measure parameters ($A_{ex} = 3.65 \times 10^{-12}$ J/m). For discretization we used 30 nm×30 nm×100 nm cells, i.e. approximating the film by a single layer. The lateral cell size is somewhat larger than the exchange length $l_{ex} = \sqrt{2A_{ex}/(\mu_0 M_s^2)} \approx 20$ nm, but it is still at least a hundred times smaller than the wavelength, and no discrepancies could be observed compared to smaller cell sizes, while the simulation can be completed in a reasonable time. To avoid reflections, in the left and right hand side of the simulation 3 μm wide artificial absorbing layers were created using a quadratically increasing damping constant. On the lateral boundaries periodic boundary conditions (single repetition) were used to simulate a long waveguide and avoid energy loss on the sides. The external field was chosen to be 221 mT, using an analytical dispersion formula to match the measurement wavelength at the given frequency (the external field at the exact position of the sample cannot be measured with sufficient precision in our setup). The FIB irradiation was modeled as a region with (M_s=0 A/m. The field of the CPW was calculated by HFSS, assuming 1 mA current (peak) in the waveguide. The simulation was run for 180 ns, which was long enough to form a steady interference pattern.

4.6 Conclusions

Optically inspired spin-wave devices represent a promising route towards wave-based computing, which itself is an approach for post-von-Neumann computing. The Rowland grating we demonstrate here is a complex spin-wave optics device and the main component of the Rowland circle spectrometer proposed in [85]. The spin-wave patterns we observe behave remarkably similar to expectations and to the behavior of ideal isotropic waves.

Our device cannot yet operate as a fully functional Rowland spectrometer, due to the nonlinear excitation process that launches the spin waves. The standing waves in the waveguide region form only if a single-frequency excitation is applied at the waveguide. Simulations also confirm that spin waves are not launched if multiple frequency components are simultaneously applied on the waveguide and the device cannot yet perform spectral analysis of a signal with a multitude of frequency components. The device, however, allows the identification of a single applied frequency - this can be determined from the position focus on the Rowland circle. It is likely that a more sensitive read-out method (possibly micro-BLS) could detect spin waves generated directly by the waveguide and would prove that this device is a fully functional spectrometer.

A key result we demonstrate here is the utility of FIB irradiation to draw patterns in YIG with nanoscale precision but without removing material. This minimizes the damage to the adjacent YIG areas. The irradiated patterns can influence spin-wave propagation and may also act as wave sources nearby a waveguide. The manipulation of magnetic properties via FIB in other material systems is well-established, but we are not aware of fabricated spin-wave elements in YIG using a similar approach.

Besides demonstrating complex spin-wave patterns in YIG films, we also described a newfound way of creating spin waves via nonlinear resonance, a method that exploits high-amplitude standing-wave oscillations to indirectly excite short-wavelength spin waves with complex wavefronts. This method itself may have important device applications as it enables strong coupling between a complex-shaped spin-wave launcher (the Rowland grating) and the simple straight waveguide, in cases where only single-frequency excitation is required.

Acknowledgements

The authors are grateful for fruitful discussions and encouragement from Gary Bernstein, Hadrian Aquino (University of Notre Dame), Andrii Chumak (University of Vienna) and Philipp Pirro (TU Kaiserslautern). Many thanks to all staff members at TUM, especially Anika Kwiatkowski. Furthermore, we would like to acknowledge the support of the Central Electronics and Information Technology Laboratory – ZEIT^{lab}. This work was partially funded by the Deutsche Forschungsgemeinschaft (DFG, German Research Foundation) – Projektnummer (429656450) and Projektnummer (403505866), and by the US National Science Foundation (NSF) with a grant from the SpecEES (Spectrum Efficiency, Energy Efficiency, and Security) program. Ádám Papp received funding from the TUM TUFF postdoctoral grant, and from the postdoctoral grant of the Hungarian Academy of Sciences/Eötvös Loránd Research Network (PPD 2019). Levent Sahin was funded with a postdoctoral grant of Philipp Schwartz-Initiative and Simon Mendisch was supported by TUM International Graduate School of Science and Engineering (IGSSE). We are grateful for support from PicoQuant.

4.7 Personal contribution

This work was originally published as Á. Papp, M. Kiechle, S. Mendisch, *et al.*, "Experimental demonstration of a concave grating for spin waves in the rowland arrangement", *Scientific Reports*, vol. 11, no. 1, pp. 1–8, 2021. DOI: 10.1038/s41598-021-93700-z, and we decided to make this a first-coauthorship, as Ádám and I both put so much work into this project, in fact we did most of the experiments together, that we do not want to undervalue one or the other contribution. This is the first paper we published within my doctoral project.

Sample preparation

I sputter fabricated the 100 nm YIG thin films via sputter-deposition and characterized them using ferromagnetic resonance (FMR). For the metallization, I used E-beam evaporation to deposit 350 nm aluminum directly onto YIG. A contact mask with a negative resist was used to lithographically fabricate co-planar microwave antennas. There was no working lift-off process using the contact mask, and the aluminum was etched off by phosphoric acid, which was found to be sufficiently selective to YIG (etched three times slower).

Direct focused-ion-beam irradiation of YIG

After the preliminary experiments I conducted on YIG with direct FIB irradiation, and providing evidence that we can change the effective magnetization, we wanted to experimentally demonstrate Ádám's previous work where he designed a Rowland spectrometer for spin waves [85]. In short, he did the design, I did the experiment. The intuitive idea was to use a very high ion dose to locally destroy the magnetization, similar to physically etching a grating into YIG as suggested in the original design. An ion dose of $1.5 \cdot 10^{14}$ ions/cm^2 was not detectable with FMR anymore, and we chose $1 \cdot 10^{15}$ ions/cm^2 for the grating irradiation (the more the merrier). The structures irradiated at this high dose are optically visible, but AFM measurements confirmed that we did not physically mill into film, but likely roughening the surface. I also looked into fabricating absorbing boundaries via FIB and conducted experiments with gradually increasing ion doses next to the grating with the purpose to only use a small portion of the circle (part of the Rowland condition), and to stop the waves on the side to travel into the picture. The assumption we had back then that damping increases with ion dose does not hold as much as we thought, and using drastically higher doses would cause reflections. For that reason, we kept the half-circle and its continuations to deflect the waves next to grating.

Time-resolved MOKE measurements

Ádám set up the trMOKE microscope as part of his post-doc time in Munich, which we used for spatially resolving spin-wave patterns, and we measured the first curved grating on YIG. The separation of diffraction modes did not work as expected, and furthermore, we did not understand the importance of the excitation amplitude at the time. After Ádám left Munich, I continued the experiments, used smaller antennas, varied the grating geometries, did a ton of bias field adjustments, and then tested the wave excitation at different frequencies.

Interpretation

After I found the working triple of frequencies and with the expected diffracting angles, we wanted to try simultaneous excitation at two frequencies, but found out that the amplitude (5 dBm) used for the excitation produced highly non-linear spin waves, visible as the uniform excitation behind the grating. When I used a lower amplitude for the excitation, actual waves form behind the grating, but waves would not travel past the other side. All authors have been involved in numerous meetings and discussions on the mechanism of excitation and the working principle, which is written down in the manuscripts discussion and conclusion.

5 Publication #3: A spin-wave lens designed with machine learning

This chapter is a full reprint of the accepted version for publication of the article
M. Kiechle, L. Maucha, V. Ahrens, *et al.*, "Experimental demonstration of a spin-wave lens designed with machine learning", *IEEE Magnetics Letters*, vol. 13, pp. 1–5, 2022. DOI: 10.1109/LMAG.2022.3209647.

5.1 Abstract

We present the design and experimental realization of a device that acts like a spin-wave lens i.e., it focuses spin waves to a specified location. The structure of the lens does not resemble any conventional lens design, it is a nonintuitive pattern produced by a machine learning algorithm. As a spin-wave design tool, we used our custom micromagnetic solver 'SpinTorch' that has built-in automatic gradient calculation and can perform backpropagation through time for spin-wave propagation. The training itself is performed with the saturation magnetization of a YIG film as a variable parameter, with the goal to guide spin waves to a predefined location. We verified the operation of the device in the widely used Mumax^3 micromagnetic solver, and by experimental realization. For the experimental implementation, we developed a technique to create effective saturation-magnetization landscapes in YIG by direct focused-ion-beam irradiation. This allows us to rapidly transfer the nanoscale design patterns to the YIG medium, without patterning the material by etching. We measured the effective saturation magnetization corresponding to the FIB dose levels in advance and used this mapping to translate the designed scatterer to the required dose levels. Our demonstration serves as a proof of concept for a workflow that can be used to realize more sophisticated spin-wave devices with complex functionality, e.g., spin-wave signal processors, or neuromorphic devices.

5.2 Introduction

There is an undisputed need to improve the efficiency (especially the power efficiency) of computing devices. The exponential growth of available computing power – from personal devices to large data centers – is limited by the energy consumption of the computing architectures. There is also a consensus that the power efficiency of digital, Boolean devices cannot be improved by simply replacing CMOS transistors with some different switching element.

Magnons can carry and process information at very high (several 10 GHz) bandwidths, dissipate very little energy (attojoules), and hence they are a potential candidate for beyond-Moore devices. Information processing does not necessarily have to be *digital*, instead wave-based, neuromorphic, and non-Boolean building blocks are widely seen as the most promising unconventional computing paradigms with CMOS being the most advanced digital technology platform without seriously competitive successors.

Spin-wave optical elements replicate the functions of optical computing blocks and provide a pathway to signal processing and computing functions. This motivates our work to design compact spin-wave optics elements, which are beyond the realm of classical optics. Magnonics went through an intense development in the past decade – in particular, it became possible to experimentally demonstrate devices that are magnonic versions of known optical structures in the spin-wave domain,

as proposed by [83] and [93]. The majority of magnonic devices demonstrated so far aims to replicate the behavior of the elements of classical optics. Nano-optical devices [68], however, may turn out to be a better fit for the capabilities and limitations of magnonics. One advantage nanophotonic devices have over classical optics is that they typically yield higher functionality in a smaller footprint – this could be a crucial benefit in magnonics, where damping limits device size. This observation motivates our work to design magnonic devices that are not derived from the elements of classical optics.

Nanophotonic devices are most often complex, non-intuitive scattering structures, often designed by machine learning methods [114]. We follow this route, by using our recently developed SpinTorch code [115] to design a linear scatterer that acts like a focusing lens, despite not at all resembling one in light of its structure.

Recently, multiple approaches emerged in the magnonics community for the inverse design of spin-wave scattering devices [65], [66]. These designs show a possible path towards neuromorphic computing with spin waves, magnonic signal processing and complex logical gates. However, the feasibility of experimental realization of the presented devices is not satisfactorily addressed in these works. Here we use a simple device – a lens – for the demonstration of a workflow that includes both the inverse design of the device, and a fabrication method to implement it.

5.3 Design of a Spin-Wave Lens with Machine Learning

In contrast to using fundamental design principles for spin-wave devices (e.g. optical design methods), the use of machine learning allows us to discover non-intuitive design geometries and may result in improved performance, more compact footprint, and higher level of integration compared to optical systems built from discrete components. In this work, we use a lens (focusing to a specified output location) as an example of such a design to demonstrate the operation of our micromagnetic inverse-design tool, and also the feasibility of experimental realizations of such designs by our experimental technique.

5.3.1 SpinTorch: a Micromagnetic Solver with Machine Learning Integrated

We have developed and implemented a micromagnetic simulator, SpinTorch [115], with built-in gradient-based optimization capability. We have previously demonstrated that this algorithm allows us to design spin-wave scatterers that can perform various computing tasks [66]. More specifically, we have shown that these scatterer designs can perform similar tasks as neural networks, e.g. solve classification problems, linear transformations, and even nonlinear functions if spin waves are used in the nonlinear amplitude regime.

SpinTorch is built on Pytorch [116], a machine-learning framework that is widely used to build and train neural networks. It has automatic backpropagation capability, which is realized by building a computational graph of the neural network during the forward run. In our case, this means backpropagation through time for spin-wave propagation. In SpinTorch, the trainable parameters can be any parameters of the micromagnetic simulation, e.g. spatial distribution of the external field, or saturation magnetization – the latter is used in this work. The desired functionality is defined through inputs and outputs, which can be transducers on the propagation medium. Training – or inverse design – is achieved in a series of epochs, during which spin waves are launched, interference patterns and output signals are calculated, and based on the gradients the design is updated until satisfactory performance is achieved.

5.3.2 Lens design

A relatively simple but nevertheless powerful application of SpinTorch is the inverse design of spin-wave optical elements. For demonstration of our methods, we chose to design a lens, i.e. a device that focuses a wavefront to a specified location. A classical lens in optics achieves focusing by refracting

waves on the lens surfaces: its operation is determined by the lens curvature and the relative refractive index of its material. In our machine-learning approach, the refractive index is varied pointwise in the specified design region by the algorithm. This 'distributed-parameter' approach enables better utilization of space, and control of aberrations in the system by the definition of an appropriate objective function.

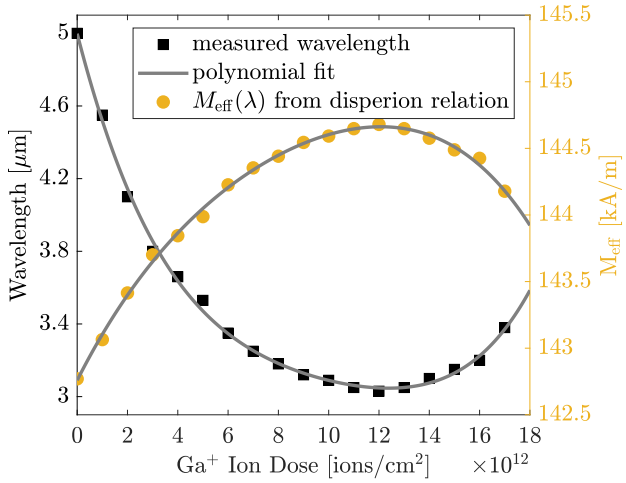

Figure 5.1 Nonlinear trend of the ion-dose-dependent change in YIG. The modified wavelengths λ_{FIB} were measured in 38x38 µm regions irradiated with the respective ion dose. Subsequently, the effective magnetization change was calculated from the respective λ_{FIB} and the spin-wave dispersion relation. The largest $M_{\text{eff}} = 144.7\,\text{kA/m}$ is used as the basis for the training.

In order to modify the refractive index of YIG for spin waves, we used FIB irradiation experimentally. In simulations and training, we modelled the effect of irradiation by a change in effective saturation magnetization (M_{eff}). The exact mapping between irradiation dose and M_{eff} was extracted experimentally through measurement of the wavelength (Fig. 5.1). We defined a 50 µm by 50 µm design region in the YIG film where the algorithm was allowed to modify the intrinsic effective magnetization between the intrinsic value $M_{\text{eff},0} = 142.8\,\text{kA/m}$, and the maximum achievable by FIB irradiation $M_{\text{eff,max}} = 144.7\,\text{kA/m}$.

We defined an artificial line source adjacent to the design region, which excites a linear spin-wave wavefront. Outputs were placed on the opposite side, circular regions with diameters of 1 µm arranged in the focal plane with 3.125 µm separation in between. Outside the design region, we included an absorbing boundary layer, which absorbs spin waves by a smoothly increasing damping coefficient. On the lateral sides of the design area, we also included 25 µm padding on both sides (truncated in Fig. 5.3 and Fig. 5.4, but shown in Fig. 5.2), where normal YIG parameters were assumed. This is required because in the experiment the excited wavefront is much longer than the irradiated region, so diffraction of waves from the neighboring regions should be considered for an optimal design.

For the simulation we used a damping coefficient value $\alpha_{\text{YIG}} = 7.9 \times 10^{-4}$, exchange coefficient $A_{\text{exch}} = 3.65\,\text{pJ/m}$, gyromagnetic ratio $\gamma_{\text{LL}} = 1.7595 \times 10^{11}\,\text{rad/Ts}$. A YIG-film thickness of 69 nm and 2D discretization of 100 nm by 100 nm were used. The excitation frequency was set to 3 GHz, the bias field to 282.5 mT (out-of-plane direction), which resulted in a spin-wave wavelength of $\lambda_0 = 5\,\mu\text{m}$ in the unirradiated regions, and $\lambda_{\text{FIB}} = 3\,\mu\text{m}$ where maximum FIB dose was applied.

We run the optimization in SpinTorch for 14 epochs, where each epoch consists of a forward micromagnetic simulation, a backward gradient calculation, and updating the design parameters, i.e. the saturation magnetization distribution (the result of the training is shown in Fig. 5.2a). Due to technical limitations of our FIB instrument, the final saturation magnetization pattern – which contained continuous values – had to be converted to binary values before irradiation (Fig. 5.2b). For this, we increased the discretization resolution by a factor of two in both lateral dimensions, and assigned a binary value to every pixel with a probability that was linearly mapped from the designed

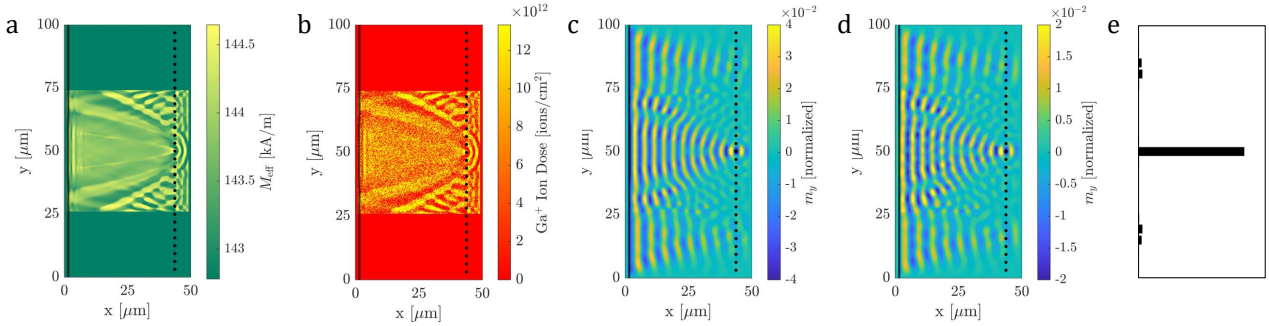

Figure 5.2 Sequence of the lens design flow. (a) Machine-learned saturation-magnetization pattern trained to focus spin waves to the center output. (b) Binarized scatterer pattern with increased resolution to match the FIB spot size and mapped to the corresponding ion dose values. (c) Spin-wave interference pattern calculated by SpinTorch after finished training (corresponding to the pattern in (a)). (d) Mumax^3 simulated spin-wave propagation in the binary pattern from (b). (e) Spin-wave intensities on the defined outputs in c).

pattern (this process can be referred to as stochastic halftoning). Here we assumed that since the pixel size is almost two orders of magnitude smaller than the spin-wave wavelength, spin waves will 'see' only the average values.

5.3.3 Design Verification with mumax^3

As a validation step of the training, we repeated the micromagnetic simulations in mumax^3 [111] with the final design pattern. Due to limitations of mumax^3 (the number of distinct M_s values is limited to 256), we only used two magnetization values (the intrinsic and maximum achievable with FIB) in the simulation patterns, this way also verifying our assumptions with the binary mapping. Fig. 5.2b and d show the binary pattern and the resulting interference pattern, respectively. A comparison with Fig. 5.2c shows good agreement between the two simulations, the slight noise in the mumax^3 simulation can be attributed to the non-exact stochastic approach taken in the binarization of the pattern.

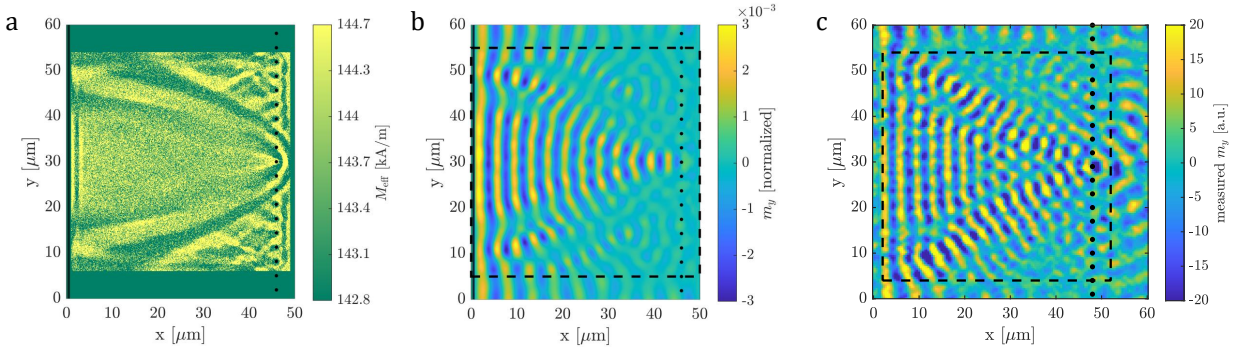

Figure 5.3 Focusing of spin waves by a machine-learning-designed magnetization pattern. (a) SpinTorch uses the two values $M_{\text{eff},0}$ and $M_{\text{eff,FIB}}$ as training parameters, and constructs a binary non-trivial saturation magnetization map by the inverse-design algorithm. (b) plane wave propagation through the pattern in (a) simulated in mumax^3. (c) Measured spin wave waveform in the FIB irradiated magnetization pattern, showing the wavefront focusing to the center output. The dashed rectangle corresponds to the 50x50 µm design area used for the training.

5.4 Experimental Realization

Direct focused-ion-beam (FIB) irradiation of yttrium-iron-garnet (YIG) films has been recently demonstrated as an efficient fabrication method for magnetization landscapes with nanoscale precision [1].

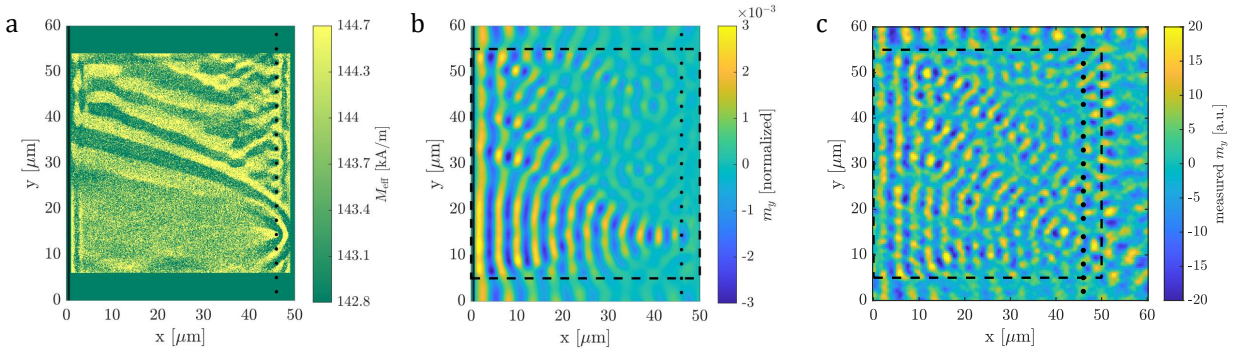

Figure 5.4 Offside focusing of spin waves to different output. (a) The binary magnetization pattern created in spinTorch. (b) mumax^3 simulation of a plane wave ($\lambda_0 = 5\,\mu$m) excited on the left, traveling through the binary magnetization pattern shown in (a). The wavelength changes due to the locally changing magnetization, which shapes the focusing to the side as originally intended. (c) trMOKE image of the FIB irradiated pattern with the wavefront focusing to the lower output.

For the experimental arrangement, a 69 nm thin YIG film with coplanar microwave antennas is used to excite spin waves with out-of-plane magnetic-field bias. The YIG film was fabricated with liquid phase epitaxy [74], and its magnetic parameters obtained from ferromagnetic-resonance (FMR) measurements are $M_{\mathrm{eff},0} = 142.8$ kA/m and $\alpha = 0.0004$. The 2D spin-wave patterns were recorded with longitudinal time-resolved magneto-optical Kerr effect (trMOKE) microscopy. A microwave frequency of $f = 3$ GHz at a power of $P =$ -10 dBm and a bias field of approximately $\mu_0 H_{\mathrm{dc}} = 282$ mT resulted in a spin-wave wavelength of $\lambda_0 = 5\,\mu$m, which was used as a basis for the simulations and experiments.

5.4.1 Engineering the Effective Magnetization in YIG via FIB

The change of the effective magnetization is ion-dose dependent, and the degree of change is measured by the wavelength change (λ_0 vs. λ_{FIB}) of spin waves traveling through irradiated regions (38x38 µm in size) of various ion doses. In Fig. 5.1 the ion dose vs. wavelength profile is shown (numerically on the left axis). It becomes clear that the trend is non-linear, and the trend turns around after achieving a minimal wavelength (doses beyond this value have little practical importance, since the damping strongly increases above this dose). We note that the profile shape changes when a different λ_0 is used, which is due to the non-linear dispersion relation. Additionally, the M_{eff} change with respect to the ion dose is presented, which was calculated using the dispersion relation. The ratio of $\lambda_0/\lambda(M_{\mathrm{eff,FIB}})$ can be modeled as the adjustable refractive index n in FIB-irradiated regions, given that $n = 1$ in intrinsic YIG. For the training of the binary lens patterns it is instructive to use the maximum achievable magnetization difference, hence the intrinsic value $M_{\mathrm{eff},0} = 142.8$ kA/m and largest $M_{\mathrm{eff,max}} = 144.7$ kA/m were used. The magnetization distribution obtained from the training in Fig. 5.3a and Fig. 5.4a can directly be used as an irradiation image in the FIB tool, and the yellow regions were irradiated at an ion dose of $1.3 \cdot 10^{13}$ ions/cm^2 with a pixel size of 50 nm (equivalent to the cell size used in the mumax^3 simulations).

5.4.2 Experimental Verification of the Lens Design

For the imaging of spin-wave propagation in YIG, we use an in-house developed time-resolved magneto-optical Kerr microscope (trMOKE). This setup is a stroboscopic scanning microscope based on a picosecond pulsed laser (405 nm), with coherent spin-wave excitation provided by a coplanar waveguide. Here the longitudinal MOKE is utilised, being sensitive to the in-plane dynamical component of the magnetization. The spatial resolution of our setup is about 1 µm, limited by the laser spot size and the minimum step size of the micro-resolution stage that is used to scan across the sample surface. Further details of the trMOKE setup are provided in [2].

The FIB irradiated patterns are optically invisible and no material in the YIG film is removed, merely the ion implantation causes a structural change of the crystal that changes the effective magnetization on the nanoscale, thus propagating spin waves with micrometer wavelengths face negligible discontinuities. For the purpose of demonstrating the design flow, i.e. the training of the M_{eff} map, its simulation with plane waves in mumax^3 and eventually the experimental verification of the FIB irradiated magnetization map, we show two lens-like operating elements that aim to focus spin waves to different locations. In the case of focusing to the center output, the trMOKE image (Fig. 5.3c) of propagating spin waves through the FIB irradiated magnetization pattern resembles the simulated scene, with the associated wave traces clearly visible. As for the offside focusing shown in Fig. 5.4c, the individual wave paths can still be recognized and the focus is in the right location, although not at highest intensity and the image itself has a much noisier background. There are many potential reasons for such imperfections, such as fluctuations in the ion beam current, resulting in an ion dose deviation, and therefore producing a different magnetization value. Using precise parameters is crucial, a small deviation in local magnetization changes can have a large impact on spin-wave interactions while propagating through. Aside from this, more common issues in spin-wave experiments such as imperfections in the YIG film or unwanted interference with waves entering the pattern from the side can distort wave form in the areas of interest. Magnetic damping is considerably low in YIG thin films, and spin-wave propagation in the few tens of micrometer areas shown in this work can propagate without much amplitude decrease. However, FIB irradiation adds a somewhat moderate damping contribution that will increase with the ion dose, which we did not take into account for the training.

Nevertheless, we observe good agreement between the simulated and experimentally fabricated magnetization patterns, and they show the intended behavior, i.e., focusing spin waves to a predefined location. This proves that SpinTorch can successfully design transfer functions/functional areas for spin waves and FIB can be used as an effective prototyping and fabrication tool for any magnetization pattern within the available range at nanoscale precision. Combining those two methods provides a powerful toolbox to design non-trivial spin-wave computing elements.

5.5 Conclusion

We demonstrated a general design method for spin-wave optics through the specific example of a lens. We experimentally verified our designs via direct-FIB irradiation of YIG films. Our results show a good agreement between simulation and experiment, we hope that this demonstration could ignite interest in inverse magnonics as a possible route towards nanoscale signal processors and computing devices.

While there have been numerous demonstrations of magnonic logic [104], [117]–[119] and optically-inspired spin-wave computing [80], none of these designs could overcome the challenges of the field, first of all the inefficiency of the transducers combined with extremely small signal levels and moderately high damping. We believe that our results could be used to tackle some of these issues by increasing the complexity of the functions that can be realized in the spin-wave domain before readout or amplification of the signal becomes necessary.

Acknowledgment

The authors want to thank all staff members and researchers working in the lab facilities of ZEIT$^{\text{lab}}$, an organizational unit of the Department of Electrical and Computer Engineering at TUM. We highly appreciate the funding from the German Research Foundation (DFG No. 429656450 and DFG No. 271741898) and the German Academic Exchange Service (DAAD, No. 57562081). Ádám Papp received funding from the PPD research program of the Hungarian Academy of Sciences.

5.6 Personal contribution

This work was originally published as M. Kiechle, L. Maucha, V. Ahrens, *et al.*, "Experimental demonstration of a spin-wave lens designed with machine learning", *IEEE Magnetics Letters*, vol. 13, pp. 1–5, 2022. DOI: 10.1109/LMAG.2022.3209647 and presents a new design method for spin-wave devices using machine learning, in this case with a design inspired from optics. The design method is experimentally demonstrated and verified with the developed fabrication procedure within my doctoral research, that is direct focused-ion-beam irradiation of YIG.

Sample preparation

The YIG samples (69 nm) used in this work were provided from Carsten Dubs and fabricated by liquid-phase epitaxy (LPE), known to result in minimal strain and the lowest possible magnetic damping. I provided the layout for the microwave antennas, which were fabricated by Matthias Golibrzuch, and wire-bonded the sample to the chip-carrier with the help of Anika Kwiatkowski. The training with SpinTorch requires a pre-characterization of the maximum achievable magnetization ($M_{\mathrm{eff,max}}$) change by FIB irradiation, which individual for every sample. This involves an ion-dose map next to the microwave antenna, and the ion dose that produces $M_{\mathrm{eff,max}}$ together with the intrinsic magnetization $M_{\mathrm{eff},0}$ is then used for the training. The training is also wavelength-specific, and the carefully chosen experimental settings have to be reproduced at a later stage. The parameterization did not work out well with the first sample as we could not excite wavelengths below 7 μm and the design would have been too large overall. We performed those experiments on our own samples meanwhile but later moved back to a second LPE-fabricated YIG sample, where the excitation worked better. The intention was to obtain a higher magnetization change because of the thinner film (we usually use 100 nm), and hence a larger portion of the thickness being irradiated, but this did not work happen as expected. We finished the experiments for this sample either way and left the discussion out of the manuscript, as we were not able to understand the underlying cause at that point in time. We speculated that our samples have a much messier interface (also visible in the TEM images), that the effective thickness is about 70 nm and hence, about the same as the LPE-YIG film. After the pre-characterization, I discussed the results with Levente Maucha and gave the directions for the training outputs and geometrical/fabrication constraints.

Time-resolved MOKE measurements

This metrology gives access to spatially resolved spin-wave patterns by using a stroboscopic under-sampling technique. I measured the spin-wave wavelength changes in the dose map with different initial wavelengths to not only find a dose that produces the highest magnetization difference, but also to make that the chosen wavelength propagates efficiently in the irradiated part. This turned out to be more difficult with the LPE-fabricated YIG samples we used in this experiment, as the excitation was unexpectedly narrow in terms of SW wavelength. The initial purpose was to use a better sample for cleaner signal, but we speculated that because of the perfect interface to GGG the reflection, and hence the Kerr effect, is less. After we found a working configuration, the data was also post-processed for the training. Eventually, I measured the resulting spin-waves patterns in the FIB-modified YIG film with the target excitation wavelength.

Direct focused-ion-beam irradiation of YIG

The magnetization patterns obtained from training are converted to a binary image by using a filling factor change in pixel space, a technique also developed and verified within my project. The irradiation had to be done multiple times because of calibration and stabilization problems of the FIB tool's current. I fabricated a series of slight ion dose variations and eventually found the right dose for the pattern, which was resulted in the target output for the case of center- and offside focusing.

6 Conclusion

6.1 Main results

This work presents the establishment of an efficient fabrication technique for spin-wave devices, coming up trumps with its simplicity, universality, and excellent structural quality. Nanometer-thin YIG films were in-house fabricated and used as a spin-wave medium, the most commonly researched material in this manner due to its record-low damping properties. The structuring, precisely the dimension and technology control, of magnetic media is inevitable to the technological improvement of spintronic devices. Common structuring methods include wet chemical etching, ion milling, and even a liftoff process after the magnetic layer deposition [14] while using a photo resist mask. However, these processes are not only prone to cause rough surfaces and imprecise edges, they could unintentionally alter the magnetic properties and additionally, they are limited to larger structural sizes. The ion beam patterning method presented does not physically remove material, instead, it changes the material properties in a controlled manner, offering different applications with respect to the degree of modification via ion dose.

The technology's applicability has been demonstrated by means of various device component examples used in wave computing, whereby the ion-dose-dependent change had been modeled as an adjustable, effective refractive index for spin waves. A lens is the most fundamental component in optical computing due to its Fourier properties, and magnonic realizations based on conventional optics, graded-index optics, and even machine-learned versions are presented. The underlying technology emphasizes the power of this technique: it enables the generation of magnetic landscapes of arbitrary shape, including precise formations of gradients if desired and the resolution limit posed by that of ion-beam writing is suitable for nanoscale devices. For research purposes, this offers a rapid prototyping platform and makes room for new device ideas that can be readily tested and researched, and the technology is easily adaptable to industry standards (ion implanting).

The adaptation to metallic film-based spin-wave devices, attractive because of their larger group velocities, is obvious - FIB has been extensively used in these systems to manipulate the magnetic properties. Our group just recently performed a similar experiment to the ion-dose-dependent change on the magnetic properties with Cobalt-Iron-Boron (CoFeB) alloy as a magnetic layer in a W/CoFeB/MgO stack, although focusing on the impact on domain size and the resulting skyrmion formation [22], already demonstrating FIB as a setscrew of magnetic properties in metallic magnetic systems.

In summary, this work presents an important step in the technological advance of magnonic device fabrication and uses a technology that's compatible with industry standards (ion implanting). It readily provides many device-design inspirations and example implementations, also demonstrating useful application techniques like gradient realization with the filling factor approach. With this, we aim to make a valuable to contribution to the Magnonics community and to offer a useful tool for future research interests.

6.2 Outlook

The results of this work are only a foretaste of what can be accomplished, but yet the most important milestone to get things rolling in this direction. The FIB platform is a huge playground and here are a few of many ideas on how to proceed with this project.

The underlying effect of ion-beam manipulation of YIG needs to be characterized – the modeling of the effective magnetization might be sufficient for what is presented, but the separation of the potential bilayer interaction due to the penetration depth limit combined with the specific anisotropy component needs to be understood if one wants to use other spin-wave types such surface or backward volume waves or to take advantage of larger ion dose regime. Instead of using the increase of M_{eff} in the low-dose range as it is done in this work, the high-dose range offers an interesting way to increase the achievable amount of the refractive index n by inverting the irradiation and decreasing n of the surrounding area instead.

To better understand the layer physics in this high-dose regime (the crystallinity of the top layer could be severely affected), we want to pursue He^+ FIB irradiation, as this ion species fully penetrates the 100 nm YIG film and is therefore not only providing the reference of a modified monolayer but also exploring the achievable n-change when the film is irradiated at full depth.

The FIB-induced 'damage' is irreversible by practical means, and conversely, the demonstrated device features are not reconfigurable. This important feature could be accomplished by adapting the findings of this work to the initial idea (see introduction), to use switchable Co/Pt nanomagnets on top of YIG. The switching field distribution of these magnets, and hence the range of reconfigurability, can be enhanced by using PMA YIG (Ga^+-doped) as this requires much lower bias fields.

Spin-wave imaging with our trMOKE microscope poses a limit on the wavelength resolution, allowing the investigation of fabricated spin-wave devices with dipole-dominated spin waves only. The applicability of FIB in nanoscale device manufacturing can be tested by fabricating transducers that promote smaller wavelengths combined with a higher-resolution imaging technique using x-rays, and we are currently starting a collaboration to follow this track.

A Own Publications

Journal Articles

- M. Kiechle, A. Papp, S. Mendisch, V. Ahrens, M. Golibrzuch, G. H. Bernstein, W. Porod, G. Csaba, and M. Becherer, "Spin-wave optics in yig realized by ion-beam irradiation", *Small*, p. 2 207 293, 2023. DOI: 10.1002/smll.202207293.
- Á. Papp, M. Kiechle, S. Mendisch, V. Ahrens, L. Sahin, L. Seitner, W. Porod, G. Csaba, and M. Becherer, "Experimental demonstration of a concave grating for spin waves in the rowland arrangement", *Scientific Reports*, vol. 11, no. 1, pp. 1–8, 2021. DOI: 10.1038/s41598-021-93700-z.
- M. Kiechle, L. Maucha, V. Ahrens, C. Dubs, W. Porod, G. Csaba, M. Becherer, and Á. Papp, "Experimental demonstration of a spin-wave lens designed with machine learning", *IEEE Magnetics Letters*, vol. 13, pp. 1–5, 2022. DOI: 10.1109/LMAG.2022.3209647.
- S. Mendisch, V. Ahrens, M. Kiechle, Á. Papp, and M. Becherer, "Perpendicular nanomagnetic logic based on low anisotropy Co/Ni multilayer", *Journal of Magnetism and Magnetic Materials*, vol. 510, p. 166 626, 2020. DOI: 10.1016/j.jmmm.2020.166626.
- S. Mendisch, F. Riente, V. Ahrens, L. Gnoli, M. Haider, M. Opel, M. Kiechle, M. Ruo Roch, and M. Becherer, "Controlling domain-wall nucleation in Ta/Co-Fe-B/MgO nanomagnets via local Ga^+ ion irradiation", *Phys. Rev. Applied*, vol. 16, p. 014 039, 1 2021. DOI: 10.1103/PhysRevApplied.16.014039.
- V. Ahrens, S. Mendisch, W. Kaiser, M. Kiechle, S. B.-v. Gamm, and M. Becherer, "Focused ion beam irradiation for generation of skyrmionic bubble like structures", *Journal of Magnetism and Magnetic Materials*, vol. 523, p. 167 591, 2021. DOI: 10.1016/j.jmmm.2020.167591.
- V. Ahrens, L. Gnoli, D. Giuliano, S. Mendisch, M. Kiechle, F. Riente, and M. Becherer, "Skyrmion velocities in fib irradiated w/cofeb/mgo thin films", *AIP Advances*, vol. 12, no. 3, p. 035 325, 2022. DOI: 10.1063/9.0000287.
- V. Ahrens, C. Kiesselbach, L. Gnoli, D. Giuliano, S. Mendisch, M. Kiechle, F. Riente, and M. Becherer, "Skyrmions under control–fib irradiation as a versatile tool for skyrmion circuits", *Advanced Materials*, p. 2 207 321, 2022. DOI: 10.1038/s41598-021-93700-z.

Conference Contributions

- S. Mendisch, M. Kiechle, V. Ahrens, Á. Papp, and M. Becherer, "Engineering of sputter deposited yig - a comprehensive protocol for ultra-low damping magnetic thin films", Poster Presentation, Magnonics Conference, Carovigno (BR), Italy, Jul. 2019.
- M. Kiechle, Á. Papp, S. Mendisch, C. Calcagno, V. Ahrens, G. Csaba, and M. Becherer, "Spin-wave steering in fib irradiated yig thin films", Oral Presentation, Joint European Magnetic Symposia (JEMS), Uppsala, Sweden, Aug. 2019.

- M. Kiechle, Á. Papp, M. Golibrzuch, S. Mendisch, V. Ahrens, G. Csaba, and M. Becherer, "Reconfigurable magnonic crystals in yig based on co/pt magnets with perpendicular magnetic anisotropy", in *Annual Conference on Magnetism and Magnetic Materials (MMM)*, Oral Presentation, Las Vegas, NV, United States, Nov. 2019.
- M. Kiechle, Á. Papp, S. Mendisch, V. Ahrens, W. Porod, G. Csaba, and M. Becherer, "Spin-wave spectrum analyzer with a fib created grating", in *Annual Conference on Magnetism and Magnetic Materials (MMM)*, Oral Presentation, Las Vegas, NV, United States, Nov. 2019.
- M. Kiechle, Á. Papp, S. Mendisch, V. Ahrens, L. Sahin, W. Porod, G. Csaba, and M. Becherer, "Spin wave based spectrum analysis implemented with fib-created gratings in yig", in *Joint European Magnetic Symposia (JEMS)*, Oral Presentation, Virtual, Dec. 2020.
- M. Kiechle, Á. Papp, S. Mendisch, V. Ahrens, G. Csaba, and M. Becherer, "Spin-wave optics fabricated by fib irradiation of yig films", in *Joint MMM-Intermag Conference*, Oral Presentation (online), Virtual and New Orleans, L, United States, Jan. 2022.
- M. Kiechle, Á. Papp, S. Mendisch, M. Golibrzuch, V. Ahrens, W. Porod, G. Bernstein, G. Csaba, and M. Becherer, "Magnetization gradients via direct fib irradiation of yig", in *International Conference on Magnetic films and surfaces*, Poster Presentation, Okinawa, Japan, Jul. 2022.
- M. Kiechle, M. Golibrzuch, Á. Papp, C. Calcagno, J. Greil, S. Mendisch, V. Ahrens, G. Csaba, and M. Becherer, "Bistable co/pt nanomagnets to influence the field landscape of spinwaves in yig", in *International Advanced School on Magnonics (MAGNETOFON)*, Poster Presentation, Porto, Portugal, Jul. 2022.
- M. Kiechle, Á. Papp, S. Mendisch, V. Ahrens, G. Csaba, and M. Becherer, "Magnetization gradients via direct fib irradiation of yig", in *Magnonics Conference*, Poster Presentation, Oxnard, CA, United States, Aug. 2022.

B Bibliography

[1] M. Kiechle, A. Papp, S. Mendisch, V. Ahrens, M. Golibrzuch, G. H. Bernstein, W. Porod, G. Csaba, and M. Becherer, "Spin-wave optics in yig realized by ion-beam irradiation", *Small*, p. 2 207 293, 2023. DOI: 10.1002/smll.202207293.

[2] Á. Papp, M. Kiechle, S. Mendisch, V. Ahrens, L. Sahin, L. Seitner, W. Porod, G. Csaba, and M. Becherer, "Experimental demonstration of a concave grating for spin waves in the rowland arrangement", *Scientific Reports*, vol. 11, no. 1, pp. 1–8, 2021. DOI: 10.1038/s41598-021-93700-z.

[3] M. Kiechle, L. Maucha, V. Ahrens, C. Dubs, W. Porod, G. Csaba, M. Becherer, and Á. Papp, "Experimental demonstration of a spin-wave lens designed with machine learning", *IEEE Magnetics Letters*, vol. 13, pp. 1–5, 2022. DOI: 10.1109/LMAG.2022.3209647.

[4] A. Barman, G. Gubbiotti, S. Ladak, A. O. Adeyeye, M. Krawczyk, J. Gräfe, C. Adelmann, S. Cotofana, A. Naeemi, V. I. Vasyuchka, *et al.*, "The 2021 magnonics roadmap", *Journal of Physics: Condensed Matter*, vol. 33, no. 41, p. 413 001, 2021. DOI: 10.1088/1361-648X/abec1a.

[5] A. Chumak, P. Kabos, M. Wu, C. Abert, C. Adelmann, A. Adeyeye, J. Åkerman, F. Aliev, A. Anane, A. Awad, *et al.*, "Roadmap on spin-wave computing", *IEEE Transactions on Magnetics*, 2022. DOI: 10.1109/TMAG.2022.3149664.

[6] M. Mruczkiewicz and P. Gruszecki, "The 2021 roadmap for noncollinear magnonics", in *Solid State Physics*, vol. 72, Elsevier, 2021, pp. 1–27. DOI: 10.1016/bs.ssp.2021.09.001.

[7] A. Mahmoud, F. Ciubotaru, F. Vanderveken, A. V. Chumak, S. Hamdioui, C. Adelmann, and S. Cotofana, "Introduction to spin wave computing", *Journal of Applied Physics*, vol. 128, no. 16, p. 161 101, 2020. DOI: doi.org/10.1063/5.0019328.

[8] A. V. Chumak, A. A. Serga, and B. Hillebrands, "Magnon transistor for all-magnon data processing", *Nature communications*, vol. 5, no. 1, p. 4700, 2014. DOI: 10.1038/ncomms5700.

[9] T. Fischer, M. Kewenig, D. Bozhko, A. Serga, I. Syvorotka, F. Ciubotaru, C. Adelmann, B. Hillebrands, and A. Chumak, "Experimental prototype of a spin-wave majority gate", *Applied Physics Letters*, vol. 110, no. 15, p. 152 401, 2017. DOI: 10.1063/1.4979840.

[10] J. Chen, H. Wang, T. Hula, C. Liu, S. Liu, T. Liu, H. Jia, Q. Song, C. Guo, Y. Zhang, *et al.*, "Reconfigurable spin-wave interferometer at the nanoscale", *Nano Letters*, vol. 21, no. 14, pp. 6237–6244, 2021. DOI: 10.1021/acs.nanolett.1c02010.

[11] R. Schlitz, T. Helm, M. Lammel, K. Nielsch, A. Erbe, and S. T. Goennenwein, "Focused ion beam modification of non-local magnon-based transport in yttrium iron garnet/platinum heterostructures", *Applied Physics Letters*, vol. 114, no. 25, p. 252 401, 2019. DOI: 10.1063/1.5090209.

[12] O. V. Dobrovolskiy, R. Sachser, S. A. Bunyaev, D. Navas, V. M. Bevz, M. Zelent, W. Śmigaj, J. Rychły, M. Krawczyk, R. V. Vovk, *et al.*, "Spin-wave phase inverter upon a single nanodefect", *ACS applied materials & interfaces*, vol. 11, no. 19, pp. 17 654–17 662, 2019. DOI: 10.1021/acsami.9b02717.

[13] Y. Katoh, N. S. N. Sugimoto, and A. S. A. Shibukawa, "Formation of ridges on gd3ga5o12 by ion-beam etching and subsequent phosphoric acid treatment utilizing tri-layered etching mask", *Japanese journal of applied physics*, vol. 31, no. 12R, p. 3888, 1992. DOI: 10.1143/JJAP.31.3888.

[14] N. Zhu, H. Chang, A. Franson, T. Liu, X. Zhang, E. Johnston-Halperin, M. Wu, and H. X. Tang, "Patterned growth of crystalline y3fe5o12 nanostructures with engineered magnetic shape anisotropy", *Applied Physics Letters*, vol. 110, no. 25, p. 252 401, 2017. DOI: 10.1063/1.4986474.

[15] C. Chappert, H. Bernas, J. Ferré, V. Kottler, J.-P. Jamet, Y. Chen, E. Cambril, T. Devolder, F. Rousseaux, V. Mathet, *et al.*, "Planar patterned magnetic media obtained by ion irradiation", *Science*, vol. 280, no. 5371, pp. 1919–1922, 1998. DOI: 10.1126/science.280.5371.1919.

[16] W. Ruane, S. White, J. Brangham, K. Meng, D. Pelekhov, F. Yang, and P. Hammel, "Controlling and patterning the effective magnetization in y3fe5o12 thin films using ion irradiation", *AIP Advances*, vol. 8, no. 5, p. 056 007, 2018. DOI: 10.1063/1.5007058.

[17] G. Csaba, A. Imre, G. H. Bernstein, W. Porod, and V. Metlushko, "Nanocomputing by field-coupled nanomagnets", *IEEE Transactions on Nanotechnology*, vol. 1, no. 4, pp. 209–213, 2002. DOI: 10.1109/TNANO.2002.807380.

[18] S. Mendisch, V. Ahrens, M. Kiechle, Á. Papp, and M. Becherer, "Perpendicular nanomagnetic logic based on low anisotropy Co/Ni multilayer", *Journal of Magnetism and Magnetic Materials*, vol. 510, p. 166 626, 2020. DOI: 10.1016/j.jmmm.2020.166626.

[19] S. Mendisch, F. Riente, V. Ahrens, L. Gnoli, M. Haider, M. Opel, M. Kiechle, M. Ruo Roch, and M. Becherer, "Controlling domain-wall nucleation in Ta/Co-Fe-B/MgO nanomagnets via local Ga^+ ion irradiation", *Phys. Rev. Applied*, vol. 16, p. 014 039, 1 2021. DOI: 10.1103/PhysRevApplied.16.014039.

[20] V. Ahrens, S. Mendisch, W. Kaiser, M. Kiechle, S. B.-v. Gamm, and M. Becherer, "Focused ion beam irradiation for generation of skyrmionic bubble like structures", *Journal of Magnetism and Magnetic Materials*, vol. 523, p. 167 591, 2021. DOI: 10.1016/j.jmmm.2020.167591.

[21] V. Ahrens, L. Gnoli, D. Giuliano, S. Mendisch, M. Kiechle, F. Riente, and M. Becherer, "Skyrmion velocities in fib irradiated w/cofeb/mgo thin films", *AIP Advances*, vol. 12, no. 3, p. 035 325, 2022. DOI: 10.1063/9.0000287.

[22] V. Ahrens, C. Kiesselbach, L. Gnoli, D. Giuliano, S. Mendisch, M. Kiechle, F. Riente, and M. Becherer, "Skyrmions under control–fib irradiation as a versatile tool for skyrmion circuits", *Advanced Materials*, p. 2 207 321, 2022. DOI: 10.1038/s41598-021-93700-z.

[23] H. Puszkarski and M. Krawczyk, "Magnonic crystals—the magnetic counterpart of photonic crystals", in *Solid State Phenomena*, Trans Tech Publ, vol. 94, 2003, pp. 125–134. DOI: 10.4028/www.scientific.net/SSP.94.125.

[24] A. Chumak, A. Serga, and B. Hillebrands, "Magnonic crystals for data processing", *Journal of Physics D: Applied Physics*, vol. 50, no. 24, p. 244 001, 2017. DOI: 10.1088/1361-6463/aa6a65.

[25] E. Albisetti, D. Petti, M. Madami, S. Tacchi, P. Vavassori, E. Riedo, and R. Bertacco, "Nanopatterning spin-textures: A route to reconfigurable magnonics", *Aip Advances*, vol. 7, no. 5, p. 055 601, 2017. DOI: 10.1063/1.4973387.

[26] M. Haertinger, C. H. Back, J. Lotze, M. Weiler, S. Geprägs, H. Huebl, S. T. Gönnenwein, and G. Woltersdorf, "Spin pumping in yig/pt bilayers as a function of layer thickness", *Physical Review B*, vol. 92, no. 5, p. 054 437, 2015. DOI: 10.1103/PhysRevB.92.054437.

[27] L. Liu, Y. Li, Y. Liu, T. Feng, J. Xu, X. Wang, D. Wu, P. Gao, and J. Li, "Interfacial modulation of spin pumping in yig/pt", *Physical Review B*, vol. 102, no. 1, p. 014 411, 2020. DOI: 10.1103/PhysRevB.102.014411.

[28] A. Prabhakar and D. D. Stancil, *Spin waves: Theory and applications*. Springer, 2009, vol. 5. DOI: 10.1007/978-0-387-77865-5.

[29] C. Herring and C. Kittel, "On the theory of spin waves in ferromagnetic media", *Physical Review*, vol. 81, no. 5, p. 869, 1951. DOI: 10.1103/PhysRev.81.869.

[30] A. G. Gurevich and G. A. Melkov, *Magnetization oscillations and waves*. CRC press, 1996. DOI: 10.1201/9780138748487.

[31] RP Photonics Encyclopedia. "Articles on (chromatic) dispersion, (effective) refractive index, group (phase) velocity (dispersion)". (2008), [Online]. Available: https://www.rp-photonics.com/encyclopedia.html (visited on 02/13/2023).

[32] B. Kalinikos and A. Slavin, "Theory of dipole-exchange spin wave spectrum for ferromagnetic films with mixed exchange boundary conditions", *Journal of Physics C: Solid State Physics*, vol. 19, no. 35, p. 7013, 1986. DOI: 10.1088/0022-3719/19/35/014.

[33] A. Serga, A. Chumak, and B. Hillebrands, "Yig magnonics", *Journal of Physics D: Applied Physics*, vol. 43, no. 26, p. 264 002, 2010. DOI: 10.1088/0022-3727/43/26/264002.

[34] C. Tang, M. Aldosary, Z. Jiang, H. Chang, B. Madon, K. Chan, M. Wu, J. E. Garay, and J. Shi, "Exquisite growth control and magnetic properties of yttrium iron garnet thin films", *Applied Physics Letters*, vol. 108, no. 10, p. 102 403, 2016. DOI: 10.1063/1.4943210.

[35] V. E. Demidov, M. P. Kostylev, K. Rott, P. Krzysteczko, G. Reiss, and S. O. Demokritov, "Excitation of microwaveguide modes by a stripe antenna", *Applied Physics Letters*, vol. 95, no. 11, p. 112 509, 2009. DOI: 10.1063/1.3231875.

[36] A. V. Chumak, V. I. Vasyuchka, A. A. Serga, and B. Hillebrands, "Magnon spintronics", *Nature Physics*, vol. 11, no. 6, pp. 453–461, 2015. DOI: 10.1038/nphys3347.

[37] A. V. Chumak, "Fundamentals of magnon-based computing", *arXiv preprint arXiv:1901.08934*, 2019. DOI: 10.48550/arXiv.1901.08934.

[38] Y. Au, T. Davison, E. Ahmad, P. S. Keatley, R. Hicken, and V. Kruglyak, "Excitation of propagating spin waves with global uniform microwave fields", *Applied Physics Letters*, vol. 98, no. 12, p. 122 506, 2011. DOI: 10.1063/1.3571444.

[39] T. Schneider, A. A. Serga, B. Leven, B. Hillebrands, R. L. Stamps, and M. P. Kostylev, "Realization of spin-wave logic gates", *Applied Physics Letters*, vol. 92, no. 2, p. 022 505, 2008. DOI: 10.1063/1.2834714.

[40] T. Goto, T. Yoshimoto, B. Iwamoto, K. Shimada, C. A. Ross, K. Sekiguchi, A. B. Granovsky, Y. Nakamura, H. Uchida, and M. Inoue, "Three port logic gate using forward volume spin wave interference in a thin yttrium iron garnet film", *Scientific reports*, vol. 9, no. 1, p. 16 472, 2019. DOI: 10.1038/s41598-019-52889-w.

[41] S. Klingler, P. Pirro, T. Brächer, B. Leven, B. Hillebrands, and A. V. Chumak, "Spin-wave logic devices based on isotropic forward volume magnetostatic waves", *Applied Physics Letters*, vol. 106, no. 21, p. 212 406, 2015. DOI: 10.1063/1.4921850.

[42] A. Khitun and K. L. Wang, "Non-volatile magnonic logic circuits engineering", *Journal of Applied Physics*, vol. 110, no. 3, p. 034 306, 2011. DOI: 10.1063/1.3609062.

[43] F. Gertz, A. V. Kozhevnikov, Y. A. Filimonov, D. E. Nikonov, and A. Khitun, "Magnonic holographic memory: From proposal to device", *IEEE Journal on Exploratory Solid-State Computational Devices and Circuits*, vol. 1, pp. 67–75, 2015. DOI: 10.1109/JXCDC.2015.2461618.

[44] A. Khitun, M. Bao, and K. L. Wang, "Magnetic cellular nonlinear network with spin wave bus for image processing", *Superlattices and Microstructures*, vol. 47, no. 3, pp. 464–483, 2010. DOI: 10.1016/j.spmi.2009.11.004.

[45] P. Ambs, "Optical computing: A 60-year adventure.", *Advances in Optical Technologies*, 2010. DOI: 10.1155/2010/372652.

[46] N. L. Kazanskiy, M. A. Butt, and S. N. Khonina, "Optical computing: Status and perspectives", *Nanomaterials*, vol. 12, no. 13, p. 2171, 2022. DOI: 10.3390/nano12132171.

[47] G. Csaba, Á. Papp, and W. Porod, "Perspectives of using spin waves for computing and signal processing", *Physics Letters A*, vol. 381, no. 17, pp. 1471–1476, 2017. DOI: 10.1016/j.physleta.2017.02.042.

[48] D. A. Connelly, G. Csaba, H. R. O. Aquino, G. H. Bernstein, A. Orlov, W. Porod, and J. Chisum, "Efficient electromagnetic transducers for spin-wave devices", *Scientific Reports*, vol. 11, no. 1, p. 18 378, 2021. DOI: 10.1038/s41598-021-97627-3.

[49] J. Slonczewski, "Excitation of spin waves by an electric current", *Journal of Magnetism and Magnetic Materials*, vol. 195, no. 2, pp. L261–L268, 1999. DOI: 10.1016/S0304-8853(99)00043-8.

[50] V. E. Demidov, S. Urazhdin, and S. O. Demokritov, "Direct observation and mapping of spin waves emitted by spin-torque nano-oscillators", *Nature materials*, vol. 9, no. 12, pp. 984–988, 2010. DOI: 10.1038/nmat2882.

[51] M. Collet, O. Gladii, M. Evelt, V. Bessonov, L. Soumah, P. Bortolotti, S. Demokritov, Y. Henry, V. Cros, M. Bailleul, *et al.*, "Spin-wave propagation in ultra-thin yig based waveguides", *Applied Physics Letters*, vol. 110, no. 9, p. 092 408, 2017. DOI: 10.1063/1.4976708.

[52] Z. Ren, S. Liu, L. Jin, T. Wen, Y. Liao, X. Tang, H. Zhang, and Z. Zhong, "Reconfigurable nanoscale spin-wave directional coupler using spin-orbit torque", *Scientific Reports*, vol. 9, no. 1, p. 7093, 2019. DOI: 10.1038/s41598-019-43597-6.

[53] Z. Zhang, M. Vogel, J. Holanda, M. B. Jungfleisch, C. Liu, Y. Li, J. E. Pearson, R. Divan, W. Zhang, A. Hoffmann, *et al.*, "Spin-wave frequency division multiplexing in an yttrium iron garnet microstripe magnetized by inhomogeneous field", *Applied Physics Letters*, vol. 115, no. 23, p. 232 402, 2019. DOI: 10.1063/1.5127881.

[54] A. Khitun, D. E. Nikonov, and K. L. Wang, "Magnetoelectric spin wave amplifier for spin wave logic circuits", *Journal of Applied Physics*, vol. 106, no. 12, p. 123 909, 2009. DOI: 10.1063/1.3267152.

[55] V. E. Demidov, S. Urazhdin, and S. O. Demokritov, "Control of spin-wave phase and wavelength by electric current on the microscopic scale", *Applied Physics Letters*, vol. 95, no. 26, p. 262 509, 2009. DOI: 10.1063/1.3279152.

[56] F. Groß, M. Zelent, N. Träger, J. Förster, U. T. Sanli, R. Sauter, M. Decker, C. H. Back, M. Weigand, K. Keskinbora, *et al.*, "Building blocks for magnon optics: Emission and conversion of short spin waves", *ACS nano*, 2020. DOI: 10.1021/acsnano.0c07076.

[57] A. Papp, G. Csaba, and W. Porod, "Optically-inspired computing based on spin waves", in *2016 IEEE International Conference on Rebooting Computing (ICRC)*, IEEE, 2016, pp. 1–4. DOI: 10.1109/ICRC.2016.7738707.

[58] E. Almpanis, *Optomagnonic Structures: Novel Architectures for Simultaneous Control of Light and Spin Waves*. World Scientific, 2021.

[59] J. W. Goodman, *Introduction to Fourier optics*. Roberts and Company publishers, 1969. DOI: 10.1063/1.3035549.

[60] D. Woods and T. J. Naughton, "Photonic neural networks", *Nature Physics*, vol. 8, no. 4, pp. 257–259, 2012. DOI: 10.1038/nphys2283.

[61] Y. Zuo, B. Li, Y. Zhao, Y. Jiang, Y.-C. Chen, P. Chen, G.-B. Jo, J. Liu, and S. Du, "All-optical neural network with nonlinear activation functions", *Optica*, vol. 6, no. 9, pp. 1132–1137, 2019. DOI: 10.1364/OPTICA.6.001132.

[62] M. Vogel, P. Pirro, B. Hillebrands, and G. Von Freymann, "Optical elements for anisotropic spin-wave propagation", *Applied Physics Letters*, vol. 116, no. 26, p. 262 404, 2020. DOI: 10.1063/5.0018519.

[63] Á. Papp and G. Csaba, "Lens design for computing with anisotropic spin waves", *IEEE Magnetics Letters*, vol. 9, pp. 1–5, 2018. DOI: 10.1109/LMAG.2018.2872127.

[64] J.-N. Toedt, M. Mundkowski, D. Heitmann, S. Mendach, and W. Hansen, "Design and construction of a spin-wave lens", *Scientific reports*, vol. 6, p. 33 169, 2016. DOI: 10.1038/srep33169.

[65] Q. Wang, A. V. Chumak, and P. Pirro, "Inverse-design magnonic devices", *Nature communications*, vol. 12, no. 1, pp. 1–9, 2021. DOI: 10.1038/s41467-021-22897-4.

[66] Á. Papp, W. Porod, and G. Csaba, "Nanoscale neural network using non-linear spin-wave interference", *Nature communications*, vol. 12, no. 1, pp. 1–8, 2021. DOI: 10.1038/s41467-021-26711-z.

[67] Z. Yan, Y. Xing, and X. Han, "Inverse design of magnonic filter", *Journal of Magnetism and Magnetic Materials*, vol. 563, p. 169 976, 2022. DOI: 10.1016/j.jmmm.2022.169976.

[68] S. Molesky, Z. Lin, A. Y. Piggott, W. Jin, J. Vucković, and A. W. Rodriguez, "Inverse design in nanophotonics", *Nature Photonics*, vol. 12, no. 11, pp. 659–670, 2018. DOI: 10.1038/s41566-018-0246-9.

[69] N. Mohammadi Estakhri, B. Edwards, and N. Engheta, "Inverse-designed metastructures that solve equations", *Science*, vol. 363, no. 6433, pp. 1333–1338, 2019. DOI: 10.1126/science.aaw2498.

[70] G. Marcucci, D. Pierangeli, and C. Conti, "Theory of neuromorphic computing by waves", in *Nonlinear Optics*, Optica Publishing Group, 2021, NTh1A–7. DOI: 10.1364/NLO.2021.NTh1A.7.

[71] R. Nakane, G. Tanaka, and A. Hirose, "In a spin-wave reservoir for machine learning", in *2019 International Joint Conference on Neural Networks (IJCNN)*, IEEE, 2019, pp. 1–9. DOI: 10.1109/IJCNN.2019.8852280.

[72] J. Ding, T. Liu, H. Chang, and M. Wu, "Sputtering growth of low-damping yttrium-iron-garnet thin films", *IEEE Magnetics Letters*, vol. 11, pp. 1–5, 2020. DOI: 10.1109/LMAG.2020.2989687.

[74] C. Dubs, O. Surzhenko, R. Thomas, J. Osten, T. Schneider, K. Lenz, J. Grenzer, R. Hübner, and E. Wendler, "Low damping and microstructural perfection of sub-40nm-thin yttrium iron garnet films grown by liquid phase epitaxy", *Physical Review Materials*, vol. 4, no. 2, p. 024 416, 2020. DOI: 10.1103/PhysRevMaterials.4.024416.

[75] E. Schmoranzerová, T. Ostatnickỳ, J. Kimák, D. Kriegner, H. Reichlová, R. Schlitz, A. Baďura, Z. Šobáň, M. Münzenberg, G. Jakob, *et al.*, "Giant quadratic magneto-optical response of thin yig films for sensitive magnetometric experiments", *arXiv preprint arXiv:2110.13679*, 2021. DOI: 10.1103/PhysRevB.106.104434.

[76] R. Dreyer, G. Woltersdorf, G. Schmidt, and D. Grundler, *Magneto-optical Super-Nyquist Sampling of Linear and Non-linear Spin-wave Phenomena*. Martin-Luther-Universität Halle-Wittenberg, 2022. [Online]. Available: https://books.google.de/books?id=vlhfzwEACAAJ.

[77] C. Kittel, "On the theory of ferromagnetic resonance absorption", *Physical review*, vol. 73, no. 2, p. 155, 1948. DOI: 10.1103/PhysRev.73.155.

[78] S. Klingler, A. V. Chumak, T. Mewes, B. Khodadadi, C. Mewes, C. Dubs, O. Surzhenko, B. Hillebrands, and A. Conca, "Measurements of the exchange stiffness of yig films using broadband ferromagnetic resonance techniques", *Journal of Physics D: Applied Physics*, vol. 48, no. 1, p. 015 001, 2014. DOI: 10.1088/0022-3727/48/1/015001.

[79] J. Ziegler, "Srim & trim", *http://www. srim. org/*, 2013.

[80] H. Dai, A. Xiao, D. Wang, Y. Xue, M. Gao, X. Zhang, C. Liu, and Q. Lu, "The focusing properties of spin wave with fresnel lens phase profile", *Journal of Magnetism and Magnetic Materials*, p. 166 756, 2020. DOI: 10.1016/j.jmmm.2020.166756.

[81] H. Qin, R. B. Holländer, L. Flajšman, F. Hermann, R. Dreyer, G. Woltersdorf, and S. van Dijken, "Nanoscale magnonic fabry-pérot resonator for low-loss spin-wave manipulation", *Nature communications*, vol. 12, no. 1, pp. 1–10, 2021. DOI: 10.1038/s41467-021-22520-6.

[82] H. Yu, G. Duerr, R. Huber, M. Bahr, T. Schwarze, F. Brandl, and D. Grundler, *Omnidirectional spin-wave nanograting coupler nat*, 2013. DOI: 10.1038/ncomms3702.

[83] G. Csaba, A. Papp, and W. Porod, "Spin-wave based realization of optical computing primitives", *Journal of Applied Physics*, vol. 115, no. 17, p. 17C741, 2014. DOI: 10.1063/1.4868921.

[84] C. S. Davies and V. Kruglyak, "Graded-index magnonics", *Low Temperature Physics*, vol. 41, no. 10, pp. 760–766, 2015. DOI: 10.1063/1.4932349.

[85] Á. Papp, W. Porod, Á. I. Csurgay, and G. Csaba, "Nanoscale spectrum analyzer based on spin-wave interference", *Scientific reports*, vol. 7, no. 1, pp. 1–9, 2017. DOI: doi.org/10.1038/s41598-017-09485-7.

[86] P. Trempler, R. Dreyer, P. Geyer, C. Hauser, G. Woltersdorf, and G. Schmidt, "Integration and characterization of micron-sized yig structures with very low gilbert damping on arbitrary substrates", *Applied Physics Letters*, vol. 117, no. 23, p. 232 401, 2020. DOI: 10.1063/5.0026120.

[87] Y. Khivintsev, G. Dudko, V. Sakharov, Y. Nikulin, and Y. Filimonov, "Propagation of spin waves in microstructures based on yttrium–iron garnet films decorated by a ferromagnetic metal", *Physics of the Solid State*, vol. 61, no. 9, pp. 1614–1621, 2019. DOI: 10.1134/S1063783419090129.

[88] E. Albisetti, S. Tacchi, R. Silvani, G. Scaramuzzi, S. Finizio, S. Wintz, C. Rinaldi, M. Cantoni, J. Raabe, G. Carlotti, *et al.*, "Optically inspired nanomagnonics with nonreciprocal spin waves in synthetic antiferromagnets", *Advanced Materials*, vol. 32, no. 9, p. 1 906 439, 2020. DOI: 10.1002/adma.201906439.

[89] C. S. Davies, A. Francis, A. V. Sadovnikov, S. V. Chertopalov, M. T. Bryan, S. V. Grishin, D. A. Allwood, Y. P. Sharaevskii, S. Nikitov, and V. Kruglyak, "Towards graded-index magnonics: Steering spin waves in magnonic networks", *Physical Review B*, vol. 92, no. 2, p. 020 408, 2015. DOI: 10.1103/PhysRevB.92.020408.

[90] J. Chang, V. Sitzmann, X. Dun, W. Heidrich, and G. Wetzstein, "Hybrid optical-electronic convolutional neural networks with optimized diffractive optics for image classification", *Scientific Reports*, vol. 8, Aug. 2018. DOI: 10.1038/s41598-018-30619-y.

[91] H. G. Bauer, P. Majchrak, T. Kachel, C. H. Back, and G. Woltersdorf, "Nonlinear spin-wave excitations at low magnetic bias fields", *Nature communications*, vol. 6, no. 1, pp. 1–7, 2015. DOI: 10.1038/ncomms9274.

[92] N. Whitehead, S. Horsley, T. Philbin, and V. Kruglyak, "A luneburg lens for spin waves", *Applied Physics Letters*, vol. 113, no. 21, p. 212 404, 2018. DOI: 10.1063/1.5049470.

[93] N. Whitehead, S. Horsley, T. Philbin, and V. Kruglyak, "Graded index lenses for spin wave steering", *Physical Review B*, vol. 100, no. 9, p. 094 404, 2019. DOI: 10.1103/PhysRevB.100.094404.

[94] R. Paschotta, "Article on 'lenses' in the encyclopedia of laser physics and technology", *1. edition, Wiley-VCH, ISBN 978-3-527-40828-3*, 2008.

[95] R. A. Gallardo, P. Alvarado-Seguel, F. Brevis, A. Roldán-Molina, K. Lenz, J. Lindner, and P. Landeros, "Spin-wave channeling in magnetization-graded nanostrips", *Nanomaterials*, vol. 12, no. 16, p. 2785, 2022. DOI: 10.3390/nano12162785.

[96] W. J. Smith, *Modern Optical Engineering*. McGraw-Hill Professional, 4th Edition, 2008, ISBN: 9780819470966.

[97] M. Gołebiewski, P. Gruszecki, and M. Krawczyk, "Self-imaging based programmable spin-wave lookup tables", *Advanced Electronic Materials*, vol. 8, no. 10, p. 2 200 373, 2022. DOI: 10.1002/aelm.202200373.

[98] J. C. Gartside, K. D. Stenning, A. Vanstone, H. H. Holder, D. M. Arroo, T. Dion, F. Caravelli, H. Kurebayashi, and W. R. Branford, "Reconfigurable training and reservoir computing in an artificial spin-vortex ice via spin-wave fingerprinting", *Nature Nanotechnology*, vol. 17, no. 5, pp. 460–469, 2022. DOI: 10.1038/s41565-022-01091-7.

[99] J. Lynn and H. Mook, "Temperature dependence of the dynamic susceptibility of nickel", *Physical Review B*, vol. 23, no. 1, p. 198, 1981. DOI: 10.1103/PhysRevB.23.198.

[100] H. Chang, P. Li, W. Zhang, T. Liu, A. Hoffmann, L. Deng, and M. Wu, "Nanometer-thick yttrium iron garnet films with extremely low damping", *IEEE Magnetics Letters*, vol. 5, pp. 1–4, 2014. DOI: 10.1109/LMAG.2014.2350958.

[101] S. Maendl, I. Stasinopoulos, and D. Grundler, "Spin waves with large decay length and few 100 nm wavelengths in thin yttrium iron garnet grown at the wafer scale", *Applied Physics Letters*, vol. 111, no. 1, p. 012 403, 2017. DOI: 10.1063/1.4991520.

[102] J. Stigloher, M. Decker, H. S. Körner, K. Tanabe, T. Moriyama, T. Taniguchi, H. Hata, M. Madami, G. Gubbiotti, K. Kobayashi, *et al.*, "Snell's law for spin waves", *Physical review letters*, vol. 117, no. 3, p. 037 204, 2016. DOI: 10.1103/PhysRevLett.117.037204.

[103] B. Divinskiy, N. Thiery, L. Vila, O. Klein, N. Beaulieu, J. Ben Youssef, S. Demokritov, and V. Demidov, "Sub-micrometer near-field focusing of spin waves in ultrathin yig films", *Applied Physics Letters*, vol. 116, no. 6, p. 062 401, 2020. DOI: 10.1063/1.5131689.

[104] F. Heussner, G. Talmelli, M. Geilen, B. Heinz, T. Brächer, T. Meyer, F. Ciubotaru, C. Adelmann, K. Yamamoto, A. A. Serga, *et al.*, "Experimental realization of a passive gigahertz frequency-division demultiplexer for magnonic logic networks", *physica status solidi (RRL)–Rapid Research Letters*, vol. 14, no. 4, p. 1 900 695, 2020. DOI: 10.1002/pssr.201900695.

[105] A. Papp, G. Csaba, H. Dey, M. Madami, W. Porod, and G. Carlotti, "Waveguides as sources of short-wavelength spin waves for low-energy ict applications", *The European Physical Journal B*, vol. 91, no. 6, pp. 1–7, 2018. DOI: 10.1140/epjb/e2018-80623-x.

[106] S. Urazhdin, V. Demidov, H. Ulrichs, T. Kendziorczyk, T. Kuhn, J. Leuthold, G. Wilde, and S. Demokritov, "Nanomagnonic devices based on the spin-transfer torque", *Nature nanotechnology*, vol. 9, no. 7, pp. 509–513, 2014. DOI: 10.1038/nnano.2014.88.

[107] H. Fulara, M. Zahedinejad, R. Khymyn, A. Awad, S. Muralidhar, M. Dvornik, and J. Åkerman, "Spin-orbit torque–driven propagating spin waves", *Science advances*, vol. 5, no. 9, eaax8467, 2019. DOI: 10.1126/sciadv.aax8467.

[108] J. James, *Spectrograph design fundamentals*. Cambridge University Press, 2007. DOI: 10.1017/CBO9780511534799.

[109] C. Davies and V. Kruglyak, "Generation of propagating spin waves from edges of magnetic nanostructures pumped by uniform microwave magnetic field", *IEEE Transactions on Magnetics*, vol. 52, no. 7, pp. 1–4, 2016. DOI: 10.1109/TMAG.2016.2517000.

[110] M. Wu, "Nonlinear spin waves in magnetic film feedback rings", *Solid State Physics*, vol. 62, pp. 163–224, 2010. DOI: 10.1016/B978-0-12-374293-3.00003-1.

[111] A. Vansteenkiste, J. Leliaert, M. Dvornik, M. Helsen, F. Garcia-Sanchez, and B. Van Waeyenberge, "The design and verification of mumax3", *AIP advances*, vol. 4, no. 10, p. 107 133, 2014. DOI: 10.1063/1.4899186.

[112] M. Wu, B. A. Kalinikos, and C. E. Patton, "Generation of dark and bright spin wave envelope soliton trains through self-modulational instability in magnetic films", *Physical review letters*, vol. 93, no. 15, p. 157 207, 2004. DOI: 10.1103/PhysRevLett.93.157207.

[113] J. A. Arregi, P. Riego, and A. Berger, "What is the longitudinal magneto-optical kerr effect?", *Journal of Physics D: Applied Physics*, vol. 50, no. 3, 03LT01, 2016. DOI: 10.1088/1361-6463/aa4ea6.

[114] G. Genty, L. Salmela, J. M. Dudley, D. Brunner, A. Kokhanovskiy, S. Kobtsev, and S. K. Turitsyn, "Machine learning and applications in ultrafast photonics", *Nature Photonics*, vol. 15, no. 2, pp. 91–101, 2021. DOI: 10.1038/s41566-020-00716-4.

[115] A. Papp. "SpinTorch". (2022), [Online]. Available: https://github.com/a-papp/SpinTorch (visited on 06/26/2022).

[116] "PyTorch". (2022), [Online]. Available: https://pytorch.org/ (visited on 06/26/2022).

[117] Q. Wang, M. Kewenig, M. Schneider, R. Verba, F. Kohl, B. Heinz, M. Geilen, M. Mohseni, B. Lägel, F. Ciubotaru, *et al.*, "A magnonic directional coupler for integrated magnonic half-adders", *Nature Electronics*, vol. 3, no. 12, pp. 765–774, 2020. DOI: 10.1038/s41928-020-00485-6.

[118] K. Vogt, F. Y. Fradin, J. E. Pearson, T. Sebastian, S. D. Bader, B. Hillebrands, A. Hoffmann, and H. Schultheiss, "Realization of a spin-wave multiplexer", *Nature Communications*, vol. 5, no. 1, pp. 1–5, 2014. DOI: 10.1038/ncomms4727.

[119] A. Sadovnikov, E. Beginin, S. Odincov, S. Sheshukova, Y. P. Sharaevskii, A. Stognij, and S. Nikitov, "Frequency selective tunable spin wave channeling in the magnonic network", *Applied Physics Letters*, vol. 108, no. 17, p. 172 411, 2016. DOI: 10.1063/1.4948381.

[120] R. Dreyer, N. Liebing, E. R. Edwards, A. Müller, and G. Woltersdorf, "Spin-wave localization and guiding by magnon band structure engineering in yttrium iron garnet", *Physical Review Materials*, vol. 5, no. 6, p. 064 411, 2021. DOI: 10.1103/PhysRevMaterials.5.064411.

[121] J. Wu, T. Cheng, C. Lu, X. Zhou, X. Lu, and C. Bunce, "Spin-dynamic measurement techniques", in *Handbook of Spintronics*, Y. Xu, D. D. Awschalom, and J. Nitta, Eds. Dordrecht: Springer Netherlands, 2016, pp. 785–830, ISBN: 978-94-007-6892-5. DOI: 10.1007/978-94-007-6892-5_31.

[122] Q. Wang, E. T. Rogers, B. Gholipour, C.-M. Wang, G. Yuan, J. Teng, and N. I. Zheludev, "Optically reconfigurable metasurfaces and photonic devices based on phase change materials", *Nature Photonics*, vol. 10, no. 1, p. 60, 2016. DOI: 10.1038/nphoton.2015.247.

[123] F. Mushenok, R. Dost, C. Davies, D. Allwood, B. Inkson, G. Hrkac, and V. Kruglyak, "Broadband conversion of microwaves into propagating spin waves in patterned magnetic structures", *Applied Physics Letters*, vol. 111, no. 4, p. 042 404, 2017. DOI: 10.1063/1.4995991.

C Acknowledgments

This section is the hardest part for me as I already feel guilty about not being thankful enough. It goes without saying that this project would not have happened if all these people had not supported me along the way. Major shout-out to everyone who was there and helped when I had a hard time – it happened quite a lot.
Simon Mendisch, you played a central role in my work and I always valued your strong opinion. Sometimes inappropriate and discouraging, but so many more times incredibly helpful and thought-provoking. I don't know how I would have managed this project, thank you for always thinking a step ahead and having advice at hand.
Michael Haider, my office-mate I could ask any question, as stupid as it could be, and never received a response that was too short - your knowledge is mind-blowing and I learned so much from you. Needless to say, you added so much productive time by providing us with the most amazing IT infrastructure at TUM.
Waldemar Kaiser, you should've stayed with our group! I understand you didn't like the lab, but thank you for visiting our office so many times and for the inspiring conversations.
Valentin Ahrens, I admire how you could always keep cool. Whenever something went wrong, things did not turn out to be as dramatic after talking to you.
Matthias Golibrzuch, I regret we did not work together sooner. Thank you for enriching our project with your admirable fab processes and always being flat out.
Johannes Greil, you already helped so much in my project in the short time since you joined our group, and I wish you all the best for your Ph.D. research project. Levente Maucha, thank you for your great contributions to our work, and for always getting things done so quickly when we needed them, the university needs more students like you. Joseph Mock, it's sad that we did not have a lot of interaction due to our separate locations, but I enjoyed having you as a laid-back colleague whenever you were around.
I do want to thank the students involved in this project, especially Carolin Calcagno for her diligence and support, Daniele Tonni, Syukri Yahya, and Kien Tran.
Anika Kwiatkowski, I don't know what I would've done without your continuous support in these desperate moments in the cleanroom. Thank you for being there when I did not even ask. I also want to thank Max Stelzer, Moritz Jung, and Max Küffner for the great company in the cleanroom and the countless times you helped figure out some mess I created.
Luca Gnoli, it's been so much fun when you were around and brought the Italian flair to our group. Levent Sahin, it's been a pleasure to have you in our group and I hope you found something more interesting than SDRs at your new job.
Rosi Mittermeyer and Susanne Maier, thank you for helping me figure out all this University bureaucracy stuff and saving me so much time!
I am grateful that I was able to spend a few weeks in California on fun research exchanges in Ilya Krivorotovs' group at UC Irvine. Eric Montoya, Mishu Khan, and Mara Mishner thank you for involving me in all interesting tasks, teaching me useful stuff about fab and metrology, advising me on my research, and giving me fun company during this time.

Adam Papp, you've been my unofficial mentor throughout this time. I learned everything from you I could ask for, and you always made time when it was important. Although, it's been quite tough when someone's favorite word is 'trivial'. You turned this project into what it became, and aside from the crazy working hours it's been quite fun. Thank you!
Wolfgang Porod, in Notre Dame is where it all started, and I am so glad you gave me the opportunity

to dive into Magnonics. You offered me an incredible career path, and I've been sad for a long time that I had to turn this down. All the more I am happy we continued to collaborate, and I want to thank you for all your support and the great discussions.
Gary H. Bernstein, it's always been fun to hear about Magnonics (and most other things) from your viewpoint, especially when became philosophical. Thank you for all your support.
Gyorgy Csaba, your knowledge is inspiring and your tranquility when we approach deadlines is admirable. Thank you for your great ideas and all your contributions to making our projects work. ChatGPT gets nowhere close to writing such great introductions you always came up with in the middle of the night.
Markus Becherer, there is simply no better advisor anyone could ask for. You gave us room to thrive in our research, you believed in us, and were always there to solve problems. You are a good person, and I wish you all the best for your future!
Paolo Lugli, you are not at TUM anymore, but I want to thank you for advocating for Markus to temporarily take over the chair of Nanoelectronics and with this helping to awaken the nanomagnetism research again.

This doctoral program was intense, and I would surely not go through it again. The research part itself has been so much fun, but I unnecessarily wasted some important lifetime that I did not spend with my loved ones. All the more I want to thank my sister for calling in the middle of the day at least once a week and asking what I am doing (-'what do you think I am doing??'), and keeping me from working for some time. I am grateful for my family and my dear friends who had to bear me during this time and always believed in me. I want to thank my beloved partner for always listening and caring about my well-being, and the countless times you recharged my batteries after stressful moments.